THESIS FOR THE DEGREE OF DOCTOR OF PHILOSOPHY

Operando Single Particle Catalysis

Combining a Nanoreactor and Plasmonic Nanospectroscopy

DAVID ALBINSSON

CHALMERS

Department of Physics
CHALMERS UNIVERSITY OF TECHNOLOGY
Gothenburg, Sweden 2020

Operando Single Particle Catalysis

Combining a Nanoreactor and Plasmonic Nanospectroscopy

DAVID ALBINSSON

ISBN: 978-91-7905-380-2

Doktorsavhandlingar vid Chalmers tekniska högskola

Ny serie nr 4847

ISSN0346-718X

Department of Physics

Chalmers University of Technology

SE-412 96 Gothenburg

Sweden

Telephone + 46 (0)31-772 1000

Cover:

Artistic rendering of a nanoreactor containing plasmonic nanoparticles that are probed using light during a catalytic reaction.

Printed at Chalmers Reproservice

Gothenburg, Sweden 2020

Operando Single Particle Catalysis - Combining a Nanoreactor and Plasmonic Nanospectroscopy

David Albinsson
Department of Physics
Chalmers University of Technology

Abstract

Heterogeneous catalysis is an important cornerstone of modern society with strong ties to the development of sustainable sources of energy and products. Catalysts are typically realized as supported metal nanoparticles that offer active sites that can accelerate chemical reactions by providing energetically more favorable reaction paths. Despite their broad use, the scrutiny of catalysts under realistic application conditions, such as high pressure and temperature, is a major experimental challenge. This difficulty is further amplified by the complexity present in real catalysts, often consisting of large ensembles of nanoparticles that all are unique. Furthermore, reactors used in catalysis studies often give rise to ill-defined reaction conditions in terms of catalyst distribution, reactant concentration and temperature. To mitigate these challenges, techniques are being developed to enable studies of catalytic nanoparticles under relevant operation conditions, so-called operando techniques. In this context, down-sized chemical reactors can be utilized to achieve precise control of both the catalyst, and the operating conditions.

In this thesis, I have performed in situ studies of chemical reactions in/on nanoparticles by utilizing plasmonic nanospectroscopy based on the localized surface plasmon resonance (LSPR) phenomenon. The resonance condition for LSPR depends on both nanoparticle properties (size, shape, material) and the surrounding medium, which makes it possible to determine the physical and chemical state of individual nanoparticles optically. The LSPR response was used to study the oxidation of Cu nanoparticles, revealing the complex nature of nanoparticle oxidation kinetics, as well as particle specific oxidation mechanisms. Furthermore, a nanoreactor platform was developed and used in combination with plasmonic nanospectroscopy to perform operando characterization of individual Cu and Pt catalyst nanoparticles during CO oxidation. The obtained results illustrate how the oxidation of Cu results in catalyst deactivation and how reactant gradients formed inside the catalyst bed strongly affects the state of the catalyst, and thus its activity. Moreover, the nanoreactor enabled operando characterization of catalyst beds comprising 1000 well defined nanoparticles that could be individually addressed.

Keywords: localized surface plasmon resonance, plasmonic sensing, heterogeneous catalysis, single particle catalysis, Cu oxidation, CO oxidation, dark field scattering spectroscopy, nanofluidics, nanoreactor, microreactor

List of appended papers

This thesis is based on the work presented in the following papers:

I. **Single Particle Nanoplasmonic Sensing in Individual Nanofluidic Channels**

Joachim Fritzsche, **David Albinsson**, Michael Fritzsche, Tomasz J. Antosiewicz, Fredrik Westerlund, Christoph Langhammer
Nano Letters, **16,** 7857–7864 (2016)

II. **Heterodimers for in Situ Plasmonic Spectroscopy: Cu Nanoparticle Oxidation Kinetics, Kirkendall Effect, and Compensation in the Arrhenius Parameters**

David Albinsson, Sara Nilsson, Tomasz J. Antosiewicz, Vladimir P. Zhdanov, Christoph Langhammer
Journal of Physical Chemistry C, **123**, 6284–6293 (2019)

III. **Resolving single Cu nanoparticle oxidation and Kirkendall void formation with in situ plasmonic nanospectroscopy and electrodynamic simulations**

Sara Nilsson, **David Albinsson**, Tomasz J. Antosiewicz, Joachim Fritzsche, Christoph Langhammer
Nanoscale, **11**, 20725–20733 (2019)

IV. ***Operando* Detection of Single Nanoparticle Activity Dynamics inside a Model Pore Catalyst Material**

David Albinsson, Stephan Bartling, Sara Nilsson, Henrik Ström, Joachim Fritzsche and Christoph Langhammer
Science Advances, **6**(25), eaba7678 (2020)

V. **Copper under Operando Conditions - Bridging the Gap between Single Nanoparticle Probing and Catalyst-Bed-Averaging**
David Albinsson, Astrid Boje, Sara Nilsson, Christopher Tiburski, Anders Hellman, Henrik Ström and Christoph Langhammer
*Nature Commun*ications, **11**, 4832 (2020)

VI. **In Situ Plasmonic Nanospectroscopy of the CO Oxidation Reaction over Single Pt Nanoparticles**

Su Liu, Arturo Susarrey-Arce, Sara Nilsson, **David Albinsson**, Lars Hellberg, Svetlana Alekseeva and Christoph Langhammer
ACS Nano, **13**, 6090-6100 (2019)

VII. Unravelling CO Oxidation Surface Chemistry on Single Pt Catalyst Nanoparticles Inside a Nanofluidic Model Pore

David Albinsson, Stephan Bartling, Sara Nilsson, Henrik Ström, Joachim Fritzsche and Christoph Langhammer
Submitted

Related papers not included in thesis

Plasmonic Metasurface for Spatially Resolved Optical Sensing in Three Dimensions
Ferry Nugroho, David Albinsson, Tomasz Antosiewicz and Christoph Langhammer.
ACS Nano, **14**, 2345–2353 (2020)

My contribution to appended papers

Paper I: I performed the FDTD simulations and thiol binding experiments, and wrote a part of the manuscript.

Paper II: I fabricated the samples, performed all the experiments except the TEM measurements. I performed the FDTD simulations, analyzed the data and wrote the first draft of the manuscript.

Paper III: I fabricated the samples and was involved in developing the experimental method and the FDTD simulations.

Paper IV: I fabricated the samples, took part in constructing the experimental system, performed the experiments and the FDTD simulations, analyzed the data and wrote the first draft of the manuscript.

Paper V: I fabricated the samples, took part in constructing the experimental system, performed the experiments and the FDTD simulations, analyzed the data and wrote the first draft of the manuscript.

Paper VI: I was involved in developing the experimental method and performed FDTD simulation as well as data analysis.

Paper VII: I fabricated the samples, took part in constructing the experimental system, performed the experiments and the FDTD simulations, analyzed the data and wrote the first draft of the manuscript.

Table of Contents

1 Introduction

During the past decades, nanotechnology has played an increasingly important role in the development of our society. However, the use of nanostructures in human-made objects can be traced as far back as the Romans, who used metallic nanoparticles to stain glass.[1] On the other hand, the ability to understand nanomaterials and nanoparticles in a scientific way is rather recent and a consequence of the invention of techniques that enable imaging and characterization of structures on the nanometer scale. Today, state-of-the-art nanotechnology enables tailoring of nanostructures with exceptional precision in terms of size, shape and composition[2,3] and, thus, opens up the possibility to design task-specific materials at the atomic level. This development is driven both by the strive for miniaturization and by the fact that materials that are scaled down in size to the nanometer regime (10^{-9} m) can have significantly different properties than at the macroscopic scale. Understanding why, and learning how, to control these new properties has proven to have a large impact on many fields of modern technology, including electronics,[4] catalysis[5] and medicine.[6]

One field that has benefitted greatly from the progress in nanotechnology is heterogeneous catalysis, where nanostructures and nanoparticles are used to enable and control chemical reactions.[5] The word "catalyst" is something that the layman probably has heard about in the context of cars, where it refers to the part of the exhaust system that removes dangerous pollutants from the gas stream. However, the applications of catalysis stretch far beyond its use in cars, and it has been estimated that catalysts are involved in 90% of the products made by the chemical industry,[7] they play an essential role in assisting biological reactions (often in the form of enzymes) and they are the key to numerous sustainable energy technologies, such as batteries, sustainable fuel production and fuel cells.

The broad appeal of catalysts stems from their ability to make otherwise slow chemical reactions proceed much faster. This is done by providing alternative reaction paths with lower energy barriers in the elemental reaction steps. In this way, a catalyst can enable chemical reactions that would otherwise be infinitely slow. Lowering energy barriers also results in a reduced use of energy and the use of a suitable catalyst is therefore beneficial from both an environmental and economical point of view. Catalysts used in man-made systems typically consist of solid nanostructures that are used to catalyze reactions of liquid or gas phase reactants. This is known as heterogeneous catalysis because the reactants and catalyst are in different states of matter. A heterogeneous catalyst often contains a noble metal, such as Palladium (Pd), Platinum (Pt) or Rhodium (Rh), which are all quite scarce and thus expensive. Therefore, to maximize the active surface area per gram of used catalyst, the materials are scaled down to nanoparticles (1-100 nm), which are dispersed onto a highly porous support material, such as Alumina (Al_2O_3), Silica (SiO_2) or Titania

(TiO_2) and mixtures thereof. During a catalytic cycle, reactants are introduced to the catalyst where they typically adsorb. This adsorption is often followed by dissociation, surface diffusion and reaction, before finally the reaction product(s) desorb from the surface, leaving the surface free for another reaction cycle. In this way, the catalyst remains unchanged and can (in principle) be used for an infinite number of reactions. Measuring how and where on the catalyst these steps proceed is important to fully understand catalysis.

Developing efficient catalysts is a multi-disciplinary task that requires cooperation from science and engineering, much due to the many length scales that are spanned by a catalyst.[8] Starting from the Ångström level (10^{-10} m), at which the bonds in molecules are broken and formed, and spanning from the active nanoparticles (10^{-9} – 10^{-7} m) to the support materials (10^{-6} m) and all the way up to industrially sized catalyst beds (>1 m). Therefore, measurements on a real catalyst involve many different experimental methods capable of addressing different length scales and properties. These measurements are far from trivial and there are still many open questions related to what exactly is controlling a catalytic process at operating conditions. More specifically, to get the true picture of a catalytic process, one must be able to characterize both the active catalyst materials *and* the chemical transformations on them with very high spatial (below 1 nanometer), as well as temporal (down to femtoseconds) resolution. Preferably, this characterization should work at operating conditions in terms of temperature and pressure. At the same time, the transport of reactants to and from the catalyst particle surface has to be studied since mass transport is strongly affected by the dimensions of the surrounding environment (e.g. a nano- or mesopore[9]), as well as by other catalytic particles in the vicinity.[7] In this context, a large body of research has been dedicated to developing the capabilities of experimental methods for catalyst research. These methods should ideally follow the so-called *operando* methodology, meaning that they are capable of simultaneously characterizing the state of the catalyst and its performance in terms of catalytic activity, under relevant conditions.[10] This might sound trivial, however, the ability to characterize nano-scale materials with (close to) atomic resolution is an experimental challenge, and doing it at high temperatures and pressures is considered state of the art.

Chemical reactions on a heterogeneous catalyst occur at the interface between the fluid and the solid and it is therefore important to directly characterize the state of the catalyst surface. Such precise surface characterization was made possible by the birth of surface-science during the second half of the 20th century.[11] Experimental surface-science was largely enabled by three developments: (i) affordable ways to achieve ultra-high vacuum (UHV, i.e. pressures below 10^{-7} Pa), (ii) the ability to fabricate single crystal surfaces and (iii) the invention of several techniques capable of probing surfaces through the interactions with mainly photons and electrons. Prominent techniques relying on electrons include low energy electron diffraction (LEED) and X-ray photoelectron spectroscopy (XPS) which are used to probe surface structure and surface composition. Photons can be used to probe a wide range of

properties ranging from the vibrational bands of adsorbate molecules by IR spectroscopy to catalyst crystallinity by X-ray diffraction.

Studies performed on model catalysts comprised of single crystalline surfaces have generated invaluable insights into the fundamental steps involved in a catalytic process, with a famous example being the ability to track surface coverage of different species changing in time and space on a catalyst surface.[8] However, to achieve the highest possible spatial and temporal resolution, most surface science techniques are limited to operation under ideal conditions (low pressure). At the same time, it is today well-known that many reactions do not proceed in the same way at ambient pressure conditions. In addition, the model catalyst materials used for research are often an oversimplification of commercial catalysts. This creates a mismatch between the conditions, as well as the materials, used in catalysis research and technical catalysts used in industry commonly referred to as the *pressure* and *materials gap*, respectively. Hence, to bridge the pressure gap, it is necessary to develop new experimental means that allow the study of catalytic reactions and the active catalyst nanomaterials under realistic application conditions, also known as *in situ* techniques.[12] To bridge the materials gap, the model catalysts have to be replaced by "real" catalyst materials, such as nanoparticles. The latter step, however, brings along yet another experimental challenge, namely the difficulty to create an ensemble of perfectly identical nanoparticles.[13] In other words, to see beyond the averaged response of many slightly different nanoparticles, it is necessary to study individual nanoparticles, which is a grand experimental challenge that requires instruments capable of detecting small signals and tailored experimental designs.[14]

The harsh conditions in which many catalysts operate can also induce dramatic changes to the catalyst over time, including changes in the oxidation state,[15–17] sintering[18] and phase segregation.[19] Therefore, to get a correct understanding of the catalyst, it is essential to continuously monitor the catalyst during the reaction. The great importance of catalyst characterization and my approach to it is discussed further in **Chapter 2**.

In this context, the use of nanoplasmonic probes has been proposed as an attractive candidate since they are capable of characterizing individual nanoparticles, while being compatible with high pressures and temperatures.[20,21] Plasmonic nanospectroscopy is based on the localized surface plasmon resonance (LSPR) phenomenon, that results in vivid coloration of metallic particles when they are scaled down to a size smaller than the wavelength of visible light (<400 nm). This stems from a collective oscillation of the free electrons in the metal, which can be resonantly excited by light. The LSPR is very sensitive to changes occurring in, on, or in the close vicinity of, the nanoparticles that support it, and changing any of these parameters affects their optical response. Therefore, plasmonic nanoparticles can be used as optical probes to detect the state of catalyst nanoparticles and catalytic reactions that occur at the nanoscale.[20–27] Plasmonic nanospectroscopy and how it was used in my work are discussed in more detail in **Chapter 3**.

1.1 Scope of this thesis

In this thesis I present the development of a new experimental concept that enables operando characterization of catalyst nanoparticles. This is achieved by utilizing individual plasmonic nanoparticles as nanoscale probes of the catalyst bed. By combining plasmonic nanospectroscopy with the development of a miniaturized chemical reactor, a *nanoreactor,* direct correlations between the state of individual catalyst nanoparticles and their activity can be realized.

The use of plasmonic nanospectroscopy to investigate reactions in nanoparticles is explored in two studies of Cu oxidation. By combining experiments with electrodynamics simulations, correlations between the optical signature and the extent of oxidation of Cu nanoparticles is established. This knowledge is later used to investigate Cu nanoparticles during catalytic reactions.

The nanoreactor is based on the fabrication of nanofluidic channels decorated with catalyst particles. Nanofluidics is, as the name suggests, the field related to studying and controlling fluids on length scales smaller than 100 nm.[28,29] By confining molecules using nanofluidic channels, they can be guided very precisely to specific – and very small – regions, e.g. directly to selected nanoparticles where they induce specific interactions. To actualize the nanoreactor, a part of this thesis is dedicated to the development of the principle and necessary nanofabrication to combine single particle plasmonic nanoprobes with nanofluidic structures. As the first step in this quest, a liquid phase nanofluidic system is integrated with plasmonic nanoparticles that were individually optically addressable by means of dark-field scattering spectroscopy. For a first proof-of-principle, the developed nanofluidic device is used to measure minute changes in the fluids flushed through the nanofluidic system via the integrated plasmonic readout, as well as to detect molecular binding events taking place on individual plasmonic Au nanoparticles.

This is followed by the development and construction of an entirely new experimental setup that enables the operation of a nanofluidic system with a fluid in the gas phase. By connecting the nanofluidic channels directly to a mass spectrometer, characterization of the gas composition is enabled. In this way, it possible to utilize the nanofluidic systems, decorated with optically addressable catalyst nanoparticles, as nanoscale chemical flow reactors or, as we choose to call them – nanoreactors. Operando characterization of individual catalyst particles placed in the reactors is achieved by optical dark field microscopy and spectroscopy. Most notably, the nanoreactor enables non-invasive characterization of multiple (up to thousands) individual nanoparticles simultaneously. At the same time, the small reactor volumes (femtolitre to picolitre range) enables the use of extremely small catalyst loadings to the extent that every single nanoparticle in the catalyst bed can be monitored in parallel. Measurements with these nanoreactors can thus be used to study both statistically relevant particle averages, as well as interesting single particle outlier characteristics, in the same experiment.

As a further aspect, by studying specifically tailored reactor geometries, the impact of mass transport inside catalyst beds is studied. We observe large impact of mass transport at the microscale that significantly affects catalyst state and, thus, activity. In the most extreme case, conversion over a single nanoparticle in a model catalyst pore is found to impact particles placed downstream. These findings thus highlight the fact that the conditions inside a chemical reactor can vary significantly in both space and time. The nanoreactor is described in detail in **Chapter 5**. In a broader context, the downscaling of experimental techniques achieved by the nanoreactor takes us one step closer to unifying experimental measurements with theoretical modelling of technologically relevant catalytic systems.

2 Catalysis and Catalyst Characterization

After several observations that certain chemical reactions were influenced by the vicinity of metals, the term Catalysis was defined in 1835 by the Swedish chemist Jacob Berzelius. He described the phenomena where a substance influenced a chemical reaction without itself being affected.[30] Since then, this definition has been refined, and a more recent one was proposed by W. Ostwald as: "*A catalyst is a substance, which affects the rate of a chemical reaction without being part of its end product*".[31] This neatly summarized the essence of what a catalyst is. As for further definitions, if the catalyst and the reacting species are in the same state of matter or in a different state of matter, the process is categorized as homogenous or heterogeneous catalysis, respectively. Homogenous catalysis is primarily important in biological systems, where large macromolecules, such as enzymes, perform a plethora of different homogeneous catalytic reactions to keep an organism alive. When it comes to man-made catalytic processes involving both gas and liquid phase reactants, heterogeneous catalysis using a catalyst in the solid-state is the key technology.

The use of heterogeneous catalysis has had an enormous impact on the evolution of human society and today we have catalysis to thank for fuels, polymers, clean air and medicines.[7] One of the most notable discoveries, solely based on a heterogeneous catalytic process, was made in 1909 when Fritz Haber found a way to bind atmospheric nitrogen into fertilizers (ammonia). This effectively prevented mass starvation and made it possible for the world population to grow in an unprecedented way.[8,32–34] Although industrially useful, the full description of how a catalyst actually works remained a mystery for several decades, and to some extent is still an open question.

This chapter is intended to give a brief background to what heterogeneous catalysis is, why it is important and how research in the field of catalysis is typically carried out. For a comprehensive summary of the field, I recommend the recent review article by Robert Schlögl, with the suitable title "Heterogeneous Catalysis".[35]

2.1 Catalysis

The working principle of a catalyst can be summarized as a system that offers energetically more favorable reaction pathways for a chemical process, without itself being consumed.[7] A typical chemical reaction involves breaking and forming of bonds between molecular species to transform chemical compounds into new configurations. To this end, if two species, A and B, can react through a chemical

reaction to form an energetically favorable species C, it may seem intuitive to assume that that reaction would happen spontaneously. However, in many cases, although thermodynamically allowed, the reaction of A + B → C is inhibited by energetically unfavorable molecular configurations, causing the reaction to proceed extremely slowly. This is illustrated in **Figure 2.1**, where the solid lines represent the potential energy of the reactants A and B, and of the product C, as well as of the energy barrier in-between them. This barrier has to be overcome for the reaction to proceed and is a consequence of intermediate elementary reaction steps, where the reactants have to reorganize in energetically costly ways. The energy required to overcome the barrier is described by the so-called activation energy (E_a), which must be supplied externally, usually via heat, as $E = k_B T$, where k_B is the Boltzmann constant and T is temperature. The probability for the reaction to proceed can be described by the Boltzmann distribution as $P \propto e^{-\frac{E_a}{k_B T}}$. From this relation one can see that, if E_a is significantly higher than $k_B T$, the probability for the reaction to proceed is very small.

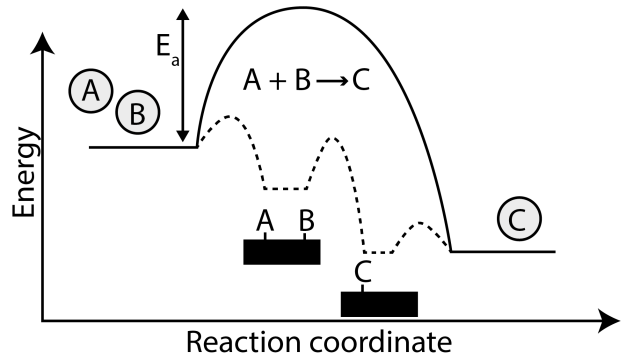

Figure 2.1 Catalyst principle. Energy diagram for a chemical reaction in the presence (dotted line) and absence (solid line) of a catalyst for the reaction between species A and B forming the product C. E_a is the activation energy needed for an uncatalyzed reaction. The intermediate steps along the dotted line correspond to typical intermediate reaction steps, namely adsorption of gas species (A & B) onto the surface, surface reaction to form C and finally desorption of C to the gas phase.

If a catalyst is introduced, it presents a new alternative reaction pathway with lower energy barriers, as illustrated by the dotted lines in **Figure 2.1.** In this way the catalyst can effectively change the energy landscape, such that the effective E_a is lowered and an increased reaction rate can be achieved. Typically, the intermediate steps are (i) adsorption of reactants on the catalyst, (ii) surface reaction and (iii) desorption of the reaction product(s), which opens the surface for the next catalytic cycle. In this way, the catalyst also collects the reactants and increases the chance of reactant interaction compared to the gas phase. For these steps to proceed efficiently the reactants should neither bind too weakly nor to strongly, which was first realized by Sabatier who gave his name to this principle.[7] He realized that if the adsorption is too weak the catalyst will not affect the adsorbate enough to e.g. break bonds and a too strong adsorption results in permanent blockage (poisoning) of the catalyst surface.

An important thing to note is that a catalyst does not change the start and end products of a reaction. Thus, the thermodynamics are unaffected because the catalyst only changes the kinetics of the reaction. However, if there are several competing chemical reactions available, a catalyst can, in principle, be tailored to target only one of the reactions and thus be used to control the ratio of end products. This can be used to increase selectivity for otherwise unfavorable reactions.

2.1.1 Heterogeneous Catalysis

In heterogeneous catalysis, the typical catalyst is a solid material where chemical reactions will take place on the surface of the catalyst. When a solid material is terminated by a surface, the outermost atoms have fewer neighboring atoms to form bonds with than the ones in the bulk, that is, they have a lower coordination number. These under-coordinated surface atoms can therefore rather easily form bonds with a molecule approaching the surface through what is known as adsorption. When such bonds are formed between a surface and a molecule, the original electronic structure (chemical bonds) of the adsorbing molecule (as well as of the surface) will be modified, potentially causing intra-molecular bonds to weaken or break, thereby forming new surface-bound species that can participate in a catalytic reaction.

Commonly, heterogeneous catalysts consist of metallic or metal-oxide structures that have nanoscale dimensions (~1-10 nm). This small size serves two main purposes. First, it maximizes the particles' surface to volume ratio and therefore minimizes material cost per active reaction site. Secondly, down-scaling of materials to the nanoscale can significantly change their original physical and chemical properties. This effect is of great importance for catalysis where nanoparticles provide modified physical as well as electronic structure, and therefore changed reactivity compared to their bulk counterparts.[8] Although the electronic structure of a nanoparticle is similar to that of bulk material, as long as the particles are larger than ~1 nm, it can be modified at the interface where the particle meets the support. Changing from single crystalline (bulk-like) to supported nanoparticles results in a catalyst that exposes a wider range of facets, corners and edges, as well as a variety of defects such as grain boundaries in the bulk and on the surface.[36] Almost a century ago, this fact was given attention by Taylor, who put forward a "Theory of the catalytic surface", where different surface sites where considered to interact differently with the reacting species.[37,38] As a consequence, so-called active sites were proposed to exist, where, for example, a specific type of defect will contribute in an disproportionate way to the overall reactivity.[35] Since the goal of catalyst research is to identify where and how catalytic reactions proceed, it is essential to identify and characterize these active sites to get an unambiguous description of the catalyst. However, characterization with this level of precision is an experimentally challenging endeavour that is actively researched to this date.[35]

In parallel with the evolution of experimental techniques, the ability to use theoretical modelling of materials from first principles using mainly density functional theory (DFT)[39] has brought about the ability to predict material properties

and chemical reactions. This has resulted in a massive surge in the field of computational chemistry[40] and by using DFT paired with other computational techniques one can today simulate nanoparticles with realistic sizes (<5 nm) in an ab-initio manner.[41,42] This, in combination with the improved experimental capabilities, means that we are closer than ever to directly linking experimental observations to theoretical models.

2.2 Techniques to Study Heterogeneous Catalysts

In its infancy, catalyst research involved mixing compounds and observing how reactions were affected. With the invention of analysis tools, such as the mass spectrometer,[43] reaction products could be quantified and a more detailed understanding of catalysts could begin to evolve. Furthermore, the invention of experimental surface science techniques made it possible to identify surface and adsorbate structures that were present under catalytic action.[44] In surface science experiments, the complex catalysts were typically replaced by simplified model systems. Historically, one of the most common model catalysts consisted of macroscopic single crystalline surfaces and they were investigated using surface sensitive techniques. In this context, low energy electron diffraction (LEED), which utilizes the short mean free path of elastically scattered electrons with low energy, can be used to probe both surface and adsorbate structure. X-ray photoelectron spectroscopy (XPS) and Auger electron spectroscopy (AES) probes the core electron states and can thus be applied to determine surface composition. In the 1990's, spatially resolved techniques such as photoelectron emission microscopy (PEEM),[45] scanning tunneling microscopy (STM)[46,47] and atomic force microscopy (AFM)[48] were developed which made it possible to image surfaces. These tools were famously used to reveal the spatiotemporal complexity involved in one of the most studied catalytic reactions, namely CO oxidation over Pt.[45] Other spectroscopic, microscopic and diffraction techniques for characterizing catalysts include X-ray diffraction (XRD) used to determine crystallinity of samples, electron microcopy to investigate structure and morphology, infrared spectroscopy and Raman spectroscopy that are widely used to determine surface species, UV-vis spectroscopy, nuclear magnetic resonance (NMR) and methods based on X-ray absorption (XAS) such as Extended X-ray absorption fine structure (EXAFS) and (XANES) that often rely on synchrotron light to maximize their resolution.[7]

Many of the surface science techniques rely on electrons travelling to/from the sample to a detector, which limits their use to UHV conditions due to scattering of electrons by gas molecules. Real catalysts, on the other hand, are typically operated at atmospheric pressure and above. This gives rise to the *pressure gap* mentioned in the introduction. Similarly, the "materials gap" separates the model catalysts and the complex real catalyst materials, which typically consist of small (< 10 nm) active catalyst nanoparticles dispersed on chemically complex matrices of (oxidic) support material to create a large specific surface area for reactions to take place. Although model catalysts have been essential in understanding the fundamentals of catalytic reactions, they are not always representative of real catalysts and may therefore be of

limited use when designing a catalyst for use in the real world. Despite this pressure gap, knowledge gained from studying ideal surfaces under UHV conditions has resulted in invaluable insight into how catalysts function and have, in some cases, correctly predicted reaction rates in an industrial process (and thus bridged the pressure gap).[49] However, going from UHV conditions to pressures used in practical catalyst applications (above 1 bar) is often accompanied by changes in mechanisms.[7,10,12] Although a catalyst is, by definition, not consumed during reaction, it can change over time. Examples of possible changes include oxidation, deposition of carbon and morphological changes, for example sintering and re-faceting. To identify the state of the catalyst during reaction conditions it is important to be able to observe the catalyst while it is at work.

Fortunately, several methods that rely on photons, e.g. IR spectroscopy, UV-vis spectroscopy, XRD and synchrotron based X-ray techniques (XAS, EXAFS, XANES), function at elevated pressures and they can thus bridge the pressure gap by enabling *in situ* characterization of real catalysts.[12,50] The sensitivity to the presence of a gas depends on the wavelength used in each technique. For example, IR spectroscopy will detect both adsorbates and gas phase molecules. To selectively detect adsorbates, sum frequency generation (SFG) can be used,[51] which relies on a nonlinear excitation process by two light sources. Furthermore, as part of intense efforts to bridge the pressure gap, techniques like high pressure STM[10,52,53] and AFM,[54] ambient pressure XPS (APXPS)[55] and environmental TEM (ETEM)[56,57] have been developed.

When it comes to the material gap, part of the difficulty lies in the fact that real catalysts consist of nanoparticles dispersed in a geometrically complex support material. The support can also actively participate in catalysis via charge or mass transfer to and from the nanoparticle. Transport of atoms or molecules between a nanoparticle and the support is known as spillover and has been extensively studied.[58] Most of the interest has been related to hydrogen spillover,[59–61] but also oxygen, carbon monoxide (CO)[61] and nitrogen oxide (NO_x)[62] have received attention. Furthermore, each individual nanoparticle has its own unique size, shape, microstructure and local environment, giving rise to ensemble averaging effects as soon as larger samples are measured. Because of averaging, important information about how specific particle properties affect activity might be lost since it is possible that only a small fraction of particles contributes in a disproportionate way to the overall activity. Additionally, the reaction conditions inside a catalyst bed can vary significantly due to, for example, temperature and concentration gradients which can in turn result in spatial variations of the catalyst state. To avoid ensemble averaging, scientists have turned to developing single particle sensitive techniques to measure both structure and activity related information,[14] with some examples being tip enhanced Raman spectroscopy to measure activity,[63] X-ray microscopy to measure catalyst morphology and composition[64] and TEM to look at microstructure and facetting.[56]

In summary, to be able to understand real catalysts there is a need to investigate catalysts under operational conditions, preferably with single particle resolution.

2.2.1 Operando Characterization

The term operando first appeared in the catalysis literature in 2002 to describe techniques that were capable of simultaneously probing the state of a catalyst and the reaction products formed.[65,66] Today, the operando methodology is widely adopted, with over 100 publications on the topic in 2019*. It's principle is illustrated in **Figure 2.2** and involves the combination of an in situ technique that probes the (surface) state of the catalyst, with a measurement of catalyst activity. Typically, the latter is performed by monitoring reaction products using mass spectroscopy (MS), gas chromatography (GC) or Fourier transform infrared spectroscopy (FTIR). In this way, changes in the state of the catalyst can be directly correlated with a change in activity, as illustrated in **Figure 2.2**. The operando methodology has therefore been imperative in correctly identifying true active phases of catalysts.

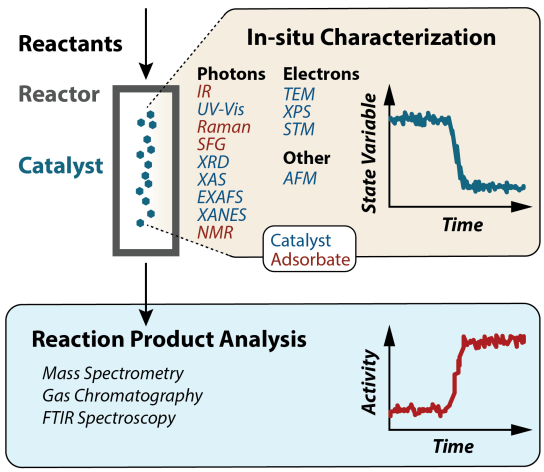

Figure 2.2 Principle of the operando methodology. An operando measurement is conducted by simultaneously measuring the state of the catalyst, using an in situ technique, and the performance of the catalyst by analyzing the reaction products. In situ techniques that mainly characterize the catalyst or adsorbates are colored blue and red, respectively.

Three of the most used techniques in operando catalysis research are UV-vis, IR, and Raman spectroscopy, due to their ability to operate under harsh conditions without requiring significant modifications to the instruments or reaction cell. Additionally, during the past two decades, several techniques that are traditionally limited to operation at UHV conditions have been upgraded, and are now applicable at operando conditions.[10,12,65,67–69] Some techniques that are today capable of operando operation are outlined in **Figure 2.2** and include high pressure STM[52,53] and AFM,[54]

* Based on a search for "*catalysis + operando*" on Web of Science

SFG,[70] environmental TEM (ETEM)[56,57,71,72] and ambient pressure XPS (APXPS).[55,69] Similarly, techniques based on X-ray diffraction (XRD) and absorption (XAS, EXAFS, XANES) which rely on high brilliance synchrotron light have been used to study catalysts under operando conditions.[10,73–75]

Another aspect that deserves consideration is the fact that research reactors almost always deviate from the real application conditions. Typically, when adapting a chemical reactor for a specific measurement technique, it involves physically altering the original reactor. Therefore, care must be taken to ensure that the reactor design itself does not dramatically change the reaction conditions by introducing ill-defined flow patterns, limited mass transport or temperature gradients inside the catalyst bed.[68] This is of particular importance when the catalyst is represented by a flat surface (wafer catalyst), as is often the case when spectroscopic techniques operating in transmission mode are used. One way to address this issue is to accurately control the flow patterns in the reactor. This has, for example, been pointed out by Thomas et al., who utilized fluid dynamics simulations to optimize the flow pattern in their operando IR reactor cell, which led to a more accurate kinetic model.[76]

Since operando characterisation typically involves exposing the catalyst bed to some kind of radiation, care must be taken to ensure that beam effects are minimized. Catalyst probes that involve high intensity light or electrons can themselves cause local hotspots or beam damage during measurements.[77] Localized heating can directly influence reaction rates and lead to significant changes to the catalyst itself.[78,79] Such beam effects have even been shown to occur >100 μm away from the probing beam[79] and even the oxidation of Au has been observed when XPS was used under ambient pressure conditions.[80] To mitigate these issues, it is important to both ensure that the techniques used are as non-invasive as possible and preferably that the whole catalyst can be characterized to minimize the risk of investigating a non-representative part of the catalyst.[81]

The emergence of operando techniques has taken us one step closer to creating realistic structure function relationships. However, most traditionally, catalyst characterization is performed by treating the whole catalyst bed as a single entity (a "black box") and characterization is performed by (i) probing the whole catalyst bed or (ii) using a spot measurement of a fraction of the bed. In the former case, measurements will correspond to an ensemble average. In the latter case, a point measurement is used to represent the catalyst as a whole and consequentially most of the catalyst is ignored. Both these approaches can be problematic because a catalyst bed can have large spatial variations in chemical composition, temperature and catalyst loading. Additionally, if the catalyst is operated under integral conditions (high conversion), there will be significant gradients in reactant concentration between the in- and outlet of the reactor. As a consequence, the information extracted using an operando measurement can be strongly influenced by where it is collected. In the end, an ideal operando experiment should be able to directly predict the bulk activity of a catalyst based on several (sub-) nano-scale measurements of the catalyst. In other words, by knowing the ingoing reactants and the exact state of the

whole catalyst (chemistry, temperature, structure etc.), the outgoing reaction products should be correctly predicted. In a real catalyst, with heterogeneities on many length scales, this inevitably involves conducting several types of measurements addressing different length scales and properties.[82]

Adding Spatial Resolution

As a natural evolution to operando technologies, methods to spatially resolve the catalyst have attracted the attention of many researchers.[68,81–86] One early example of this concept combined in situ XAS with mass spectrometry to study the oxidation state of a Rh/Al_2O_3 catalyst during partial methane oxidation. The authors demonstrated a spatial resolution of approximately 10 μm and revealed that the oxidation state of Rh changed dramatically along the reactor.[75] Additional examples of successful applications of spatially resolved operando measurements include the use of XAS to study the oxidation state of Pt during CO oxidation,[73] revealing how Pt nanoparticles changed between a reduced state and a partially oxidized state. Similarly, a study by Gänzler et al.[17] utilized a combination of IR thermography and XANES/EXAFS to study Pt, and identified reduced Pt with a slight O-coverage during CO oxidation.

Heterogeneities in temperature are common inside chemical reactors since they can occur both due to uneven external heating and based on local activity variations inside the catalyst bed. There are several techniques to spatially resolve temperature, including IR thermography,[17,87] and NMR thermometry[88] that can be used to externally probe the temperature differences in a catalyst bed. Another interesting approach that was recently demonstrated is luminescence thermometry based on lanthanide doped microparticles that are deposited in the catalyst bed and used to measure local temperature with a resolution of 10 μm.[89]

Other research has focused on local measurements of the fluid phase, i.e. how the gas/liquid composition changes in time and space inside a catalyst bed. For gas phase reactants, techniques that rely on physical probes include *spaci-MS* and *spaci-IR* that utilize a thin translatable capillary to probe the gas composition at specific positions of the catalyst.[81] Another method capable of spatially mapping the gas composition above a catalyst is Planar Laser Induced Fluorescence (PLIF),[10,90] in which a planarized laser sheet is used to excite molecules in the gas phase and quantify them by monitoring fluorescence using a camera. Similarly, for liquid phase reactions, fluorescence microscopy has been used to measure the activity of single nanoparticles.[91]

For a more comprehensive summary of the current state of (spatially resolved) operando methods, I recommend two recent reviews on the topic. Morgan et al.[81] focuses on the invasive nature of operando probes and Portela et al.[68] emphasizes the importance of combining highly local information with the global response of the catalyst bed.

2.2.2 Single Particle Techniques

Nanoparticles are typically the smallest building block of a catalyst bed and provide the active surfaces for chemical reactions. It is therefore important to know as much as possible about the nanoparticles in terms of material, size, shape and surroundings. In most cases, catalyst nanoparticles are measured by techniques that collect data from large ensembles. However, since each nanoparticle will have a unique size, shape, crystallinity and contact with its surroundings,[13] methods capable of measuring single particles are needed to avoid ensemble averaging effects. In addition, having the ability to address individual particles makes it possible to investigate inter-particle communication, which is important to understand e.g. spillover between metallic particles and an oxide support.[59] Due to their small size, nanoparticles interact weakly with any type of radiation that is used to probe them and, consequentially, a technique used for single particle studies has to provide a very high sensitivity to enable efficient data acquisition. During the past decades, a range of experimental approaches capable of addressing individual catalyst nanoparticles have been presented, with a selection of relevant techniques presented in **Table 2.1** together with their respective operational principles and limitations. In terms of categorization, the methods can be divided into two subgroups. A first group that addresses the state of the catalyst particles themselves and a second group that is used to probe the state of the species on the catalyst surface. In the first group, we find ETEM that can be used to investigate the morphology and crystalline structure of the particle,[56,71] X-ray microscopy[92] that probes the (oxidation) state of individual particles, and plasmonic nanospectroscopy[21] that can detect changes in the particles size, shape or chemistry. In the second group, we find nanoscale IR techniques that include surface/tip enhanced Raman spectroscopy (S/TERS),[93,94] surface enhanced IR absorption spectroscopy (SEIRAS)[95] and synchrotron-radiation-based and infrared nanospectroscopy (SINS)[96] that can be used to probe the surface species adsorbed to the surface of a nanoparticle. The reaction rate can be measured on single particles using e.g. scanning probe electrochemical microscopy[97] and single molecule fluorescence microscopy can be used to detect reaction rates via the formation (or consumption) of a fluorescent molecule. Lastly, plasmonic nanospectroscopy can be used to identify surface adsorbed species[20,21,98,99] and spillover from a catalyst to the surrounding support material and can therefore be used to measure reaction rates on single particles.[60]

As outlined in Table 2.1, no single techniques "has it all", and as a general trend, techniques with the highest spatial resolution (ETEM and scanning probe based methods), are limited by their field of view, while techniques with a large field of view lack spatial resolution. The technique that I have focused on in my work, is plasmonic nanospectroscopy, which will be discussed in detail in **Chapter 3**.

Table 2.1. Methods used for single particle catalysis studies

Technique	Principle	Measured property	Limitations
Single Molecule Fluorescence Microscopy	Detect catalytic event(s) by registering the formation or consumption of a fluorescent molecule occurring on a catalyst nanoparticle	Reaction Rate	Products or reactants need to be fluorescent to be detectable, dramatically limiting the reactions that can be studied.
Scanning Probe Electrochemical Microscopy[97]	Measure electrical current generated by electrochemical reactions occurring on a nanoparticle	Reaction rate	New electrode probe needed for each experiment. Tip-crash can damage sample. Liquid phase only.
X-Ray Microscopy[92]	Changes in the oxidation state or coordination environment of the atoms in the catalyst are detected by X-rays.	State of nanoparticle	High X-ray flux may damage the sample. Requires synchrotron infrastructure. No activity info.
Tip-enhanced Raman Spectroscopy (TERS)[94]	An AFM tip is used to localize visible light. Molecules are detected via vibrational features in the IR range, giving rise to a Raman shift in a probe light beam.	Molecules on catalyst surface	Tips with known enhancement are critical. Differences between tips hamper reproducibility. Needs plasmonic enhancement.
Surface Enhanced IR Spectroscopy (SEIRAS) [95]	Molecular vibrations of species on the nanoparticle surface are detected in the IR range.	Molecules on catalyst surface	Low molecular IR cross-sections give very weak signals. Limited to plasmonic metals that provide surface enhancement. Not explored for catalysis (yet).
Synchrotron-radiation-based Infrared Nanospectroscopy (SINS)[96]	Similar to TERS where an AFM tip is used for localization. IR light from synchrotron is used and scattering is collected.	Molecules on catalyst surface	Low scattering cross-section. Synchrotron light needed.
Plasmonic Nanospectroscopy[21]	Chemical or physical property changes of a catalyst particle or its local environment are detected as spectral shift of the plasmon resonance.	Nanoparticle size, shape, oxidation state and surrounding environment	Requires plasmonic material. Readout is non-specific and signal can be due to several different effects, including temperature changes. No activity info.
Environmental Transmission Electron Microscopy (ETEM)	ETEM is enabled by confining the high-pressure region close to the sample.	Nanoparticle structure	High-energy electrons may damage sample. Complex infrastructure. Limited field of view. No activity info.

2.2.3 Microreactors

One approach of the ongoing efforts to bridge material and pressure gaps that has been especially relevant to this work is the development of so called “microreactors”. Since the nanoreactor concept developed in this thesis essentially is the downscaling of a microreactor to the nanometer scale, in this section, I will give a brief overview of what microreactors are and why they are useful. For a more comprehensive description I refer the reader to one of the rather recent review articles or textbooks that exist on the subject.[100–103]

The term microreactor in catalysis research refers to a reactor with at least one dimension in the submillimeter range. Such a reactor can look like a conventional tubular reactor with very small dimensions,[16] but more often considers reactor designs that utilize microfabrication techniques to make the reactor.[100,101,104,105] Benefits of using reduced dimensions, compared to conventional reactor design, include improved heat transfer, faster diffusion times, precise control of mass transport to the active catalyst, increased safety due to lower volume of potentially hazardous compounds and the ability to do more precise in-line analysis of the reaction products.[100–102,106,107] In addition, reducing the reactor dimensions reduces the amount of catalyst material needed to result in a measurable amount of reaction products, making it possible to use precise top-down nanofabrication methods, such as electron beam lithography (EBL), to make model catalyst nanostructures.[108] The materials used to make microreactors are typically based on their compatibility with microfabrication techniques, such as EBL, photolithography and reactive ion etching, as well as with the need for chemical inertness. Hence, the materials of choice are therefore typically Si and SiO_2. Using combinations of Si and SiO_2 makes it possible both to make reactors of varying size, as well as to integrate sensors and heaters to make "reactor-on-a-chip" devices that can withstand temperatures up to 500°C.

Based on their small size and high degree of control during manufacturing, microreactors allow access for different in situ characterization methods, which makes them excellent candidates for operando experiments.[103] For example, the microreactor platform developed by Henriksen et al[108] enables activity measurements using mass spectroscopy of active catalyst areas down to 15 μm^2 and simultaneous catalyst characterization via UV-vis measurements[109] or small-angle X-ray scattering (GISAX).[110] Similar Si-based microreactors have been demonstrated to be compatible with in situ IR-thermography,[111] Raman spectroscopy,[112,113] X-ray diffraction, absorption and microscopy,[64,111] UV-vis spectroscopy[114] and FTIR[115] characterization of the active catalyst.

Microreactors also play an instrumental role in the recent attempts to increase the spatial resolution of in situ catalyst nanoparticle characterization down to the atomic level. Specifically, reactors with windows made of thin (< 100 nm) Silicon Nitride enable TEM access, which has made it possible to monitor individual catalyst nanoparticles with atomic resolution in real time and at reaction conditions.[56,113,116] This has generated new fascinating direct visualizations of Pt nanoparticle reshaping in an oscillatory manner during CO oxidation reaction,[13] as well as dramatic oxidation of Co nanoparticles.[117] The same platform has recently been modified with more well defined reactor volumes and the ability to perform hard X-ray ptychography with a spatial resolution of 23 nm.[118]

Despite these unique possibilities offered by in situ TEM in microreactors with respect to monitoring the catalyst itself during reaction with atomic resolution, even this approach still has a number of limitations. For example, simultaneous analysis of reaction products stemming from individual nanoparticles is still far out of reach. As demonstrated recently, when in situ single nanoparticle TEM characterization is

combined with analysis of reaction products, the latter is obtained from a large ensemble of nanoparticles that is considered to homogenously cover the whole length of the 320 μm wide reactor, hence, only reflecting heavily ensemble-averaged properties.[56] In other words, it is still very difficult to establish direct structure-function correlations at the single nanoparticle level. A second key limitation of the TEM approach is that only one nanoparticle can be monitored and characterized at the time since the electron beam must be focused on that particle. As a consequence, it becomes impossible to monitor several individual nanoparticles simultaneously, meaning that one cannot directly compare the behavior of individual catalyst in the same experiment, but only in sequence. Since nanostructures are dynamic during reaction and thus change with time due to, for example, sintering, this can be a significant limitation.

2.2.4 Nanoreactor for Single Particle Catalysis

As a contribution to the ongoing evolution of methods for operando catalyst research, the focus of my work has been the development of a miniaturized catalytic reactor platform. The reactor, coined a *nanoreactor*, is based on microreactor technology and relies on nanofabrication to make a reactor chip from Si and SiO_2. Illustrated in **Figure 2.3** is a schematic of the main components of the nanoreactor platform and its connections to the macroscopic world. It comprises an inlet microfluidic system connected to an array of mass flow controllers (MFCs) and a pressure controller that are used to set the gas composition and pressure inside the microfluidic channel. At the center of the microfluidic channel, a smaller nanofluidic channel is connected and leads to the catalytic reactor comprising the catalyst bed. The other end of the catalyst bed is connected to a second microfluidic channel that is directly coupled to a quadrupole mass spectrometer (QMS) capable of quantifying the gas composition exiting the reactor. In this way, a pressure driven flow can be established through the reactor by setting a high pressure (1-5 bar) on the inlet side, while pumping the outlet to high vacuum conditions (< 10^{-8} mbar). In situ catalyst characterization is performed by optical microscopy that is capable of single nanoparticle resolution by means of plasmonic nanospectroscopy.

One of the main benefits of the platform lies in its modularity, where the reactor geometry, nanoparticle loading, and positioning can be controlled at the nm scale. In the work presented in this thesis, differently designed reactors with volumes in the femtoliters to picolitres range have been investigated, which has allowed for quantitative mass spectroscopy of exposed catalyst areas below 1 μm^2 under flow conditions. To put this size in perspective, the term *nanoreactor* has been used in the literature to describe reactors with volumes in both the nanoliter[56] and microliter[118] regime, i.e. 1000,000 – 1000,000,000 times larger (in volume) than the nanoreactors I have developed.

Because the development, fabrication and utilization of this platform has been the main focus of my work, a more detailed description of the nanoreactor is given in **Chapter 5**. Leading up to that I will first introduce the principles behind plasmonic

nanospectroscopy (**Chapter 3**) and the fabrication tools needed to make the devices (**Chapter 4**).

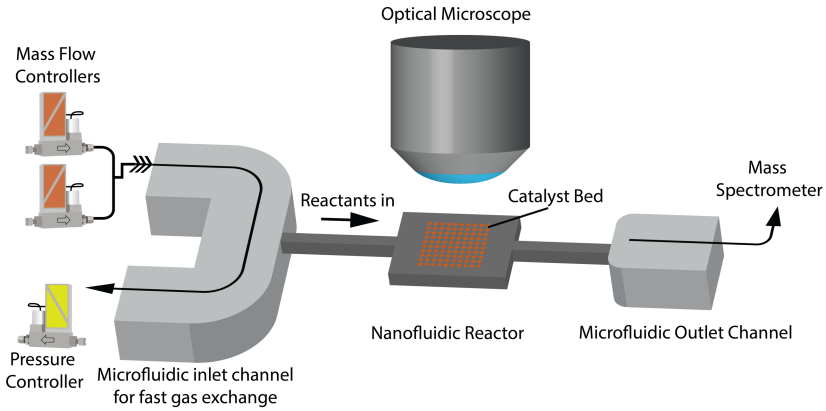

Figure 2.3 Schematic illustration of the nanoreactor platform. The nanoreactor consists of separate microfluidic and nanofluidic systems. On the inlet, a microchannel is connected on one end to an array of MFC's and on the other end to a pressure controller. This allows for control of the gas phase composition and total pressure of reactants at the inlet of the nanofluidic reactor. At the outlet, a second microfluidic channel is connected to an on-line mass spectrometer. The nanofluidic reactor connects the two microfluidic channels and comprises the catalyst bed. Operando measurements are enabled by an optical microscope that measures light stemming from nanoparticles in the catalyst bed. Note that the illustration is not to scale.

2.3 Carbon Monoxide Oxidation with O_2

One specific catalytic reaction that has been of great relevance for my thesis is the oxidation of carbon monoxide (CO) with oxygen (O_2). This reaction is probably one of the most studied model reactions in catalysis and has been extensively investigated since the 1970's[67,74] due to its importance in the automotive industry, where removal of CO from the exhaust gas stream is vital.

The reaction is:

$$CO + \frac{1}{2}\, O_2 \longrightarrow CO_2 \qquad (2.1)$$

which in the gas phase can proceed if the temperature is high enough to dissociate the O_2 molecule. This has an energy barrier of roughly 500 kJ/mol and the reaction does not occur below 700°C.[7] In contrast, in the presence of a catalyst, such as Pt, Pd, Rh or Cu, the dissociation occurs without energy barrier which allows the reaction to procced more efficiently.[7]

2.3.1 CO Oxidation over Platinum

One of the most extensively studied and utilized CO oxidation catalysts is Pt. Based on surface science UHV studies, the reaction mechanism can be described to be of the Langmuir-Hinshelwood (LH) type, according to the following four elementary steps (**Figure 2.4**): [7,119]

Reversible adsorption of CO (**Figure 2.4A**) and dissociative adsorption of O_2 (**Figure 2.4B**) on the Pt surface

$$CO + * \rightleftharpoons_{k_1^-}^{k_1^+} CO^* \tag{2.2}$$

$$O_2 + 2* \rightleftharpoons_{k_2^-}^{k_2^+} 2O^* \tag{2.3}$$

surface reaction (**Figure 2.4D**)

$$CO^* + O^* \rightleftharpoons_{k_3^-}^{k_3^+} CO_2^* + * \tag{2.4}$$

and lastly, desorption of CO_2 (**Figure 2.4D**)

$$CO_2^* \rightarrow CO_2 + * \tag{2.5}$$

In the equations, the forward and reverse reaction constants are indicated by $k_i^{+/-}$, and * indicates an empty site on the surface. Frequently, the desorption of CO_2 is considered fast and irreversible and can be ignored when kinetics is evaluated. It has also been suggested that adsorbed O_2 can react directly with adsorbed CO to form CO_2 and an O species.[120] However, for simplicity, only eqs. 2.2-2.5 are considered here.

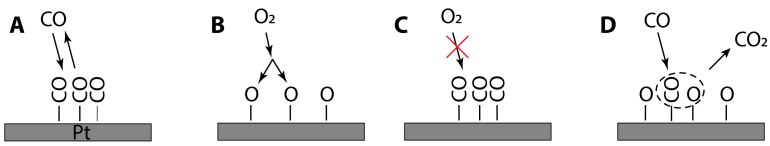

Figure 2.4 Catalytic CO oxidation on Pt. A) Adsorption and desorption of CO. B) Dissociative adsorption of O_2. C) Pre-adsorbed CO inhibits O_2 adsorption. D) CO adsorption next to previously adsorbed O species and resulting surface reaction to form CO_2.

Based on the elementary reaction steps outlined above, the time dependent surface coverages of the reactants can be expressed as

$$\frac{d\Theta_{CO}}{dt} = k_1^+\Theta_* - k_1^-\Theta_{CO} - k_3^+\Theta_{CO}\Theta_O \tag{2.6}$$

$$\frac{d\Theta_O}{dt} = 2k_2^+\Theta_*^2 - 2k_2^-\Theta_O^2 - k_3^+\Theta_{CO}\Theta_O \tag{2.7}$$

where Θ_i is the surface coverage of species *i,* and k_j is the rate constant for reaction step *j* and Θ_* is the number of free sites, defined as $\Theta_* = 1 - \Theta_O - \Theta_{CO}$. Here the partial pressure of CO and O_2 is included in k_1^+ and k_2^+, respectively. Solving these

equations can be done numerically or analytically under steady state conditions by imposing relevant assumptions. Here, I will only discuss these solutions briefly, while an in depth discussion of how this can be approached can be found in work by Zhdanov & Kasemo.[121]

In equations 2.6 & 2.7 the CO_2 production rate is

$$r = k_3^+ \Theta_O \Theta_{CO} \quad (2.8)$$

which is maximized when Θ_O and Θ_{CO} are as high as possible. Consequently, it is important to discuss the dependence of Θ_O and Θ_{CO} on gas phase composition, temperature, pressure and state of the catalyst surface.

At low temperature, CO species adsorbed to a Pt surface tend to form a densely packed surface layer, while O species form a more open structure since they adsorb in threefold coordinated sites.[8,119,122] Because O_2 dissociates upon adsorption, it requires two free neighboring sites and consequently this process is inhibited if the CO coverage exceeds a critical value (**Figure 2.4C**). The main consequence of this is that a surface exposed to a stochiometric mix of gas phase CO and O_2, at moderate temperatures, will quickly be covered by adsorbed CO that inhibits O_2 adsorption and hence suppresses the reaction since $\Theta_O \approx 0$. This is known as CO poisoning.[123] To overcome this problem, temperature can be increased, resulting in a higher desorption rate of CO, while O_2 desorption is much less affected. The increased CO desorption will allow gas phase O_2 to compete for the freed adsorption sites and Θ_O is increased. A practical consequence of the above is the so-called "cold start problem" of the automotive three-way catalytic converter, i.e. that it is not functioning efficiently before it has been heated up.

The CO poisoning effect results in two distinct reaction regimes, i.e. the poisoned regime (high Θ_{CO} and $\Theta_O \approx 0$), where the rate depends negatively on CO concentration, and the low CO coverage regime, where the rate increases with increased CO concentration (**Figure 2.5**). The transition between these two regimes can occur in a narrow CO:O_2 mixing range and gives rise to a dramatic change in reaction kinetics known as *kinetic phase transition*.[121] Close to the kinetic phase transition point, the two kinetic regimes are almost equally stable for the same mixing ratio of O_2 and CO, which gives rise to a bistability that induces hysteresis, as illustrated in **Figure 2.5**. In other words, the reaction rate is determined by the direction in which the mixing ratio is changed, i.e. whether the CO concentration is increased or decreased.

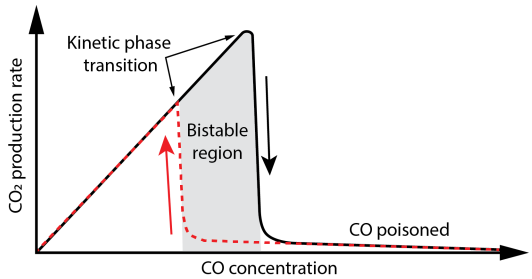

Figure 2.5 Kinetic phase transition. CO_2 production rate as a function of the introduced CO concentration (c_{CO}) at constant total pressure, O_2 concentration and temperature. At low c_{CO} the reaction rate depends positively on c_{CO}, while high c_{CO} results in a CO poisoned surface with low reaction rate. The transition between the two regimes is called the kinetic phase transition. If both states are stable in a c_{CO} range (bistable region), the catalyst can exhibit hysteresis where the activity depends on how the current state was approached.

The change in surface coverage with respect to CO and O has been shown to cause a structural reorganization of the topmost atomic layer(s) of some Pt surfaces.[7] In turn, this structural reorganization changes the adsorption and reaction dynamics, which eventually again results in a change in surface coverage, etc. Hence, spatial and temporal oscillations of the reaction rate, as well as of the surface structure, can occur, as famously demonstrated by Ertl and co-workers on single crystal surfaces at low pressures.[8,124] These observations, based on studies of isolated Pt surfaces, can unfortunately not be directly translated to nanoparticles that comprise a combination of different facets, edges and corners. In a nanoparticle, each facet will interact differently with the reactants, resulting in a facet dependent activity.[125,126] Additionally, recent studies based on DFT and kinetic Monte Carlo (kMC) have shown that it is not sufficient to study separate site-types, since the site assembly strongly affects each particles activity.[41,127] Therefore, to attain information of the catalytic performance of a nanoparticle, an actual nanoparticle has to be studied.

More recent operando studies made at ambient pressures have revealed even more dramatic changes including surface oxidation,[10,17,67,73] roughening,[52,128] nanoparticles dynamically changing shape[56] and migration of support material.[129] These studies have also shown indications that the previously suggested Langmuir-Hinshelwood mechanism might be accompanied by a so called Mars-van Krevelen (MvK) mechanism, in which a CO molecule reacts with a pre-formed surface oxide instead of just chemisorbed O-species.[67] For a comprehensive summary of the state of operando studies of CO oxidation over Pt, I refer to the review by Newton.[74]

2.3.2 CO Oxidation over Copper

Due to the scarcity of the most used CO oxidation catalyst materials (Pt, Pd, Rh), Cu has been suggested as a possible candidate to replace these noble metals. It is generally accepted that CO oxidation over metallic Cu follows the same LH mechanism as described for Pt. However, compared to Pt, Cu is less sensitive to CO

poisoning due to the lower binding energy of CO on Cu.[130] Instead Cu is sensitive to oxygen, where experiments with AP-XPS have demonstrated that CO adsorbed on a Cu surface is readily replaced by oxygen when exposed to a mix of O_2 and an excess of CO.[131] Even though it has received a fair amount of research attention, Cu is not used as a CO oxidation catalyst industrially, which can be explained by the difficulty to keep Cu in a single oxidation state under typical CO oxidation conditions.[16,130–133] This issue manifests itself as a swift deactivation when oxygen is introduced to the catalyst, which is related to the oxidation of Cu into Cu_2O and/or CuO.[16,130,131] The fact that the catalyst changes quite dramatically during reaction conditions makes the use of operando techniques essential, in order to identify which state of Cu that is present during high activity.

Although it has been recognized that the full oxidation of Cu to CuO is related to deactivation, there is an ongoing debate in the literature over which oxidation state is the most active.[16,130–134] In an early work, Jernigan et al. identified a decrease in activity as the extent of Cu oxidation increased.[134] Their conclusion was that metallic copper was the most active phase, which has more recently been confirmed by ambient pressure studies.[16,133] In contrast, a study utilizing ambient pressure XPS identified Cu_2O as the most active oxidation state,[131] which has also been proposed previously.[130,132] In this context, it has been suggested that the reaction on the oxide could follow a MvK mechanism, where a lattice oxygen is used to oxidize CO, followed by re-oxidation of the surface by O_2 from the gas phase.[132,133,135] Similarly, a recent study utilizing ETEM concluded that an amorphous Cu_xO with a continuously changing morphology is the most active phase.[136] These processes thus involve a catalyst with a continuously changing phase that can cycle through Cu, Cu_2O and CuO, which can complicate the identification of a single active phase.[133]

Parts of the disagreement found in the literature is likely due to the different catalyst types that were investigated, as well as the choice of in situ probe. For example, Eren et al.[131] identified Cu_2O as the most active phase when they investigated a single crystalline Cu(111) surface with AP-XPS which selectively probes the top 3 – 4 nm of the catalyst, and thus characterizes the surface. In contrast, Bu et al.[16] identified a decreased activity upon oxidation of Cu when they investigated nanoparticles using UV-vis spectroscopy based on the plasmonic properties of Cu nanoparticles, which mainly probes the bulk state of the catalyst. Therefore, the apparent disagreement might simply be a consequence of the probing techniques utilized in the separate studies.

Experiments conducted at ambient pressure (including my own) have shown that a high CO oxidation activity can be sustained if Cu nanoparticles are retained in a metallic state by limiting the amount of O_2 that is introduced to the catalyst.[16] This can be rationalized by considering that two reactions that consume oxygen will occur simultaneously on the Cu surface, i.e. the oxidation of CO and the oxidation of Cu. By assuming that CO oxidation on the metallic Cu surface follows a combination of LH and MvK mechanisms, the elementary steps on the Cu surface can be described by modified versions of eqs. 2.2 – 2.4, with the addition of the formation and removal

of a surface oxide. Since it is not experimentally obvious what type of oxide is formed during early stages of oxidation, a simplified model is used to describe oxide formation as a process where an adsorbed O species forms an surface (or sub-surface) oxide site[137]

$$O^* \rightarrow O_{ox} \tag{2.9}$$

The removal of the oxide is described as a reaction between an oxide site and an adsorbed CO molecule, resulting in a CO_2 and the regeneration of free Cu sites following

$$O_{ox} + CO^* \rightarrow 2* + CO_2 \tag{2.10}$$

Compared to the Pt case described above, the differential equations that describe the coverages on Cu also include an oxide coverage (θ_{ox}) and the modified equations are

$$\frac{d\Theta_{\mathrm{CO}}}{dt} = k_1^+\Theta_* - k_1^-\Theta_{CO} - k_3^+\Theta_{CO}\Theta_O - k_{\mathrm{red}}\Theta_{\mathrm{CO}}\Theta_{\mathrm{ox}} \tag{2.11}$$

$$\frac{d\Theta_{\mathrm{O}}}{dt} = 2k_2^+\Theta_*^2 - 2k_2^-\Theta_O^2 - k_3^+\Theta_{CO}\Theta_O - k_{\mathrm{ox}}\Theta_{\mathrm{O}} \tag{2.12}$$

$$\frac{d\Theta_{\mathrm{ox}}}{dt} = k_{\mathrm{ox}}\Theta_{\mathrm{O}} - k_{red}\Theta_{ox}\Theta_{CO} \tag{2.13}$$

$$\Theta_* = 1 - \Theta_{CO} - \Theta_O - \Theta_{ox} \tag{2.14}$$

where k_{ox} is the rate constant for oxide formation and k_{red} is the rate constant that describes the reaction between a lattice oxygen and an adsorbed CO to form CO_2. These equations can then be solved numerically with relevant rate constants based on the literature and/or experimental observations. Although this model is not assumed to be complete, it correctly captured many of the relevant factors observed experimentally, such as a decrease in activity when the oxide coverage is increased ($\Theta_{ox} \rightarrow 1$). In addition to the reaction steps outlined above, adsorption of CO and O_2 directly on the oxide could be included. This would allow for an additional LH route to occur on the oxide surface, which has been suggested as a plausible route in the literature.[138]

My own contribution in this context is presented in **Paper IV** and **V**, where we identify that oxidation of Cu nanoparticles (to Cu_2O and CuO) is accompanied by a decrease in CO oxidation activity. During high activity we also observed signs of a surface oxide that was repeatedly formed and decomposed, indicating a MvK mechanism involving lattice oxygen. Our ability to study individual catalyst particles also showed clear particle differences that we attribute to structural differences. Currently we are not able to directly correlate a specific particles structural properties to catalyst activity. Nevertheless, the ability to identify differences is an indication that single particle studies are important to correctly characterize a real catalyst bed.

3 Plasmonic Nanoparticles

When metals are reduced to a size smaller than the wavelength of light their optical properties change dramatically, giving rise to vivid coloration of otherwise often gray shiny materials. These colors stem from a phenomenon caused by resonant collective oscillations of the conduction electrons in the material and are known as Localized Surface Plasmon Resonances (LSPR). Interestingly, these resonances are strongly dependent on a wide set of properties of the nanoparticles, such as the material, size, shape and permittivity of the medium surrounding them. This chapter will focus on explaining the physics governing the optical properties of metallic nanoparticles, as well as explain why they are interesting.

3.1 Optical Properties of Bulk Metals

Optical properties of all materials are governed by how the materials interact with visible light, that is, the part of the electromagnetic spectrum with a wavelength from 400 to 750 nm. Bulk metals and their shiny appearance are something well known to most of us, and the fact that some metals appear gray, whereas others appear colored, is also common knowledge. In this section, I will briefly describe what gives rise to colors in some metals.

In atoms or molecules, the energy levels that electrons can occupy are discrete and to excite an electron from one energy level to another costs a finite amount of energy. The molecule can absorb a photon with energy that matches one of the gaps between energy levels via an electronic transition. In a semiconductor, a similar absorption process can take place by exciting an electron from the valence band to the conduction band above the band gap. If this absorption occurs in the range of visible light, the material will appear to have color due to the "removal" of photons in a certain wavelength span. In contrast, metals have no minimum energy needed to excite an electron to a non-bound state (i.e. no band gap). Instead, when exposed to an electric field such as light, the free electrons in a metal will immediately rearrange to screen the field. If they have enough time to fully rearrange and screen the incoming field, the metal will reflect the incident field and thus reflect the light. However, above a certain frequency the electrons will not be able to respond fast enough to the external field. This essentially makes the screening impossible and the electromagnetic wave will not be reflected. This frequency is known as the plasma frequency. Additionally, if the band structure of a certain metal allows for electrons to be excited from a region with high density of states (typically a d-band) to the Fermi level, certain wavelengths of the electromagnetic spectrum can be absorbed by

the metal in a fashion similar to the case of semiconductors in what is known as an interband transition. This process is what gives rise to the coloration of, for example, bulk Au which has an interband transition threshold at 2.5 eV (496 nm) that results in blue light being absorbed, making the metal appear yellow. If the onset for interband transitions has a lower energy than visible light (< 1.65 eV or > 750 nm) photons of all colors can be (partially) absorbed into the metal, making it appear duller and less shiny, which can be seen for, for example, palladium. Physically, the interaction of a metal (as well as semiconductors and insulators) with incident electromagnetic fields can be described by their complex dielectric function.

3.2 Optical Properties of Metallic Nanoparticles

The fact that metals change their optical properties when scaled down in size is something that has been used for centuries, long before any attempts to understand the physics of why these optical changes occurred had been reported. A classic example is the Lycurgus Cup, shown in **Figure 3.1**, dating back to the 4th century A.D. It has the fascinating property that it is perceived to have different colors depending on if it is viewed against a dark or a bright background.

Figure 3.1 The Lycurgus cup. A Roman-era cup made such that it appears red when light is transmitted through it (left) and green when light is reflected by it (right). The reason for this optical phenomenon is the colloidal noble metal nanoparticles in the glass that both scatter and absorb light in the visible range. Images from the website of the British Museum. [139]

The reason is that the glass in the cup contains colloidal metallic nanoparticles (Au, Ag and Cu) that both absorb and scatter light mostly in the green part of the optical spectrum.[1] As a result, the cup appears green when the scattered light is seen and red when transmitted light is seen. The phenomenon giving rise to these colors is the LSPR.

Figure 3.2A illustrates a nanoparticle that is smaller than the wavelength of an incident time-dependent electric field. As a consequence of the field, the electrons in the particle are displaced with respect to the atomic cores, resulting in charge separation. In turn, this will give rise to a restoring force that tries to pull the electrons back in place, making the system behave as a damped harmonic oscillator with spring

constant and damping depending on the shape, size and material of the particle. Thus, incoming electromagnetic radiation that matches the resonance frequency of the nanoparticle will result in strong absorption and scattering, which in turn gives rise to color if the resonance is in the visible range of the spectrum.

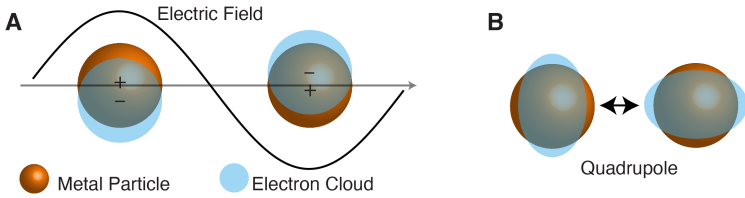

Figure 3.2 The localized surface plasmon resonance (LSPR). A) Schematic illustration of free electrons in a nanoparticle being displaced by an incident time-dependent electric field causing an oscillation of the free electrons. B) Higher order quadrupole resonance.

Due to the displacement of the electrons during a LSPR excitation, a dipolar field is induced close to the particle. For very small particles, this dipolar mode shown in **Figure 3.2A** dominates, but higher order modes, such as quadrupoles illustrated in **Figure 3.2B** are also possible, especially as the nanoparticle size is increased.[140] The enhanced field region created by such resonances can act as a probe of the dielectric environment surrounding the particle, making it useful as an optical nanoscale sensor in many applications including biosensing, chemical sensing, and gas sensing.[22,24,98,99,141,142] For the same reason, it is also the main method that I have used to study minute changes on (single) catalyst nanoparticles in this thesis.

To qualitatively describe the LSPR phenomenon, it is initially sufficient to consider a simplified system consisting of a metallic sphere with a radius much smaller than the wavelength of light. This makes it possible to employ analytical solutions developed by Gustav Mie to calculate the electromagnetic response of the system.[143] For a small spherical particle one can assume that the electrostatic approximation holds, meaning that at a given time, there is no spatial variation of the electric field along the whole sphere. Hence, upon exposure to an electric field, $\boldsymbol{E_0}$, a dipole moment will be induced as:

$$\boldsymbol{P} = \varepsilon_d \alpha \boldsymbol{E_0}$$

Where ε_d is the dielectric function of the embedding medium and α is the polarizability of the sphere that can be expressed as:[144]

$$\alpha(\omega) = 4\pi r^3 \frac{\varepsilon_m - \varepsilon_d}{\varepsilon_m + 2\varepsilon_d} \qquad (3.1)$$

where r is the radius of the sphere and ε_m is the frequency dependent dielectric function of the metal. The strength of the particle-light interaction can be expressed as cross-section, and for a perfect sphere an interaction cross-section can be calculated for scattering, absorption and extinction, respectively[144]:

$$C_{absorption} = k\mathrm{Im}(\alpha) = 4\pi k r^3 \mathrm{Im}\left(\frac{\varepsilon_m - \varepsilon_d}{\varepsilon_m + 2\varepsilon_d}\right) \quad (3.2)$$

$$C_{scattering} = \frac{k^4}{6\pi}\mathrm{abs}(\alpha)^2 = \frac{8\pi}{3}k^4 r^6 \left|\frac{\varepsilon_m - \varepsilon_d}{\varepsilon_m + 2\varepsilon_d}\right|^2 \quad (3.3)$$

$$C_{extinction} = C_{absorption} + C_{scattering} \quad (3.4)$$

where $k = \frac{2\pi}{\lambda}$ is the wavenumber of incident light. From these equations we can note that both scattering and absorption are maximized by maximizing the polarizability. Furthermore, we see that scattering scales as r^6, while absorption scales as r^3. This means that larger particles will predominantly scatter light, while smaller ones mainly absorb. For both processes the cross-section will diverge when the denominator goes to zero, i.e. when

$$\varepsilon_m(\omega) = -2\varepsilon_d \quad (3.5)$$

which is the resonance condition for LSPR.

As briefly mentioned previously, the optical properties of different metals can be quite different, meaning that ε_m varies from metal to metal. However, in a simple picture a metal can be described by the Drude model, which assumes that all conduction electrons are delocalized and free to move, thus ignoring any potential interband transitions. This approximation allows us to describe the complex dielectric function of the metal as:[144]

$$\varepsilon_m(\omega) = 1 - \frac{\omega_p^2}{\omega^2 + i\Gamma\omega} \quad (3.6)$$

where ω_p is the plasma frequency and Γ is a damping parameter that originates from processes taking place in the material to dissipate energy. The plasma frequency is defined as

$$\omega_p = \sqrt{\frac{Ne^2}{\varepsilon_0 m_e}} \quad (3.7)$$

where *N, e and* m_e is the free electron number density, charge and mass, respectively, and ε_0 is the permittivity of free space.

By further assuming that damping is negligible, putting eq. 3.6 into eq. 3.5 and solving for ω, the LSPR frequency reads as:

$$\omega_{LSPR} = \frac{\omega_p}{\sqrt{1 + 2\varepsilon_d}} \quad (3.8)$$

or expressed in terms of wavelength:

$$\lambda_{LSPR} = \lambda_p\sqrt{2\varepsilon_d + 1} \quad (3.9)$$

where $\lambda_p$is the plasma wavelength defined as $\lambda_p = \frac{c}{\omega_p}$, where c is the speed of light. Although very simplified, this model captures the key aspects of the LSPR, such as its

dependence on the surrounding medium, which gives rise to a spectral redshift when its refractive index ($n = \varepsilon_d^2$) is increased.

Above we assumed the damping was negligible, however, in real nanoparticles, damping will always take place and it will strongly affect the optical properties of the nanoparticle. The main sources of damping are either radiative processes (scattering), or non-radiative processes, mainly dominated by electron-hole excitations in the metal through intra- and interband transitions. Increasing the damping factor will lower the lifetime of the LSPR and as a result the resonance peak will widen in the frequency domain.

Although the description presented above is very useful for conceptual understanding, real nanostructures neither are ideal spheres nor are their dielectric functions as simple as the form suggested by Drude. To address real materials with realistic shapes in different constellations, other approaches have to be used and will be addressed in the following section.

3.2.1 Effects of Material, Shape and Size

The two most widely used materials in the field of plasmonics are Au and Ag thanks to their superior optical properties that give rise to narrow LSPR bands in the visible range, as well as due to their chemical inertness (especially in the case of Au). However, the field of plasmonics is not limited to these materials and has been expanded to include Cu, Pt, Pd, Ni, Al,[145–148] alloys of noble metals,[149,150] as well as non-metallic materials such as nitrides.[151] Naturally, each of these materials has its own electronic structure that gives rise to different dielectric functions and thus different plasmonic properties.

Size can strongly affect the optical properties of nanoparticles. When the particle size is increased, the incoming field will no longer be the same across the whole particle, which leads to retardation effects. This will result in a phase shift between the incident and induced dipolar field in the particle, which in turn will red shift the resonance. As shown in eq. 3.3, scattering increases rapidly with volume, giving rise to strong radiative damping. Therefore, larger particles are also expected to exhibit more radiative damping, a shorter lifetime and thus a wider resonance peak.[152] The non-radiative damping channel is dominated by absorption and results in a broadening of the resonance peak in materials that have strong absorption in the same range as the LSPR. This is typically seen in materials with allowed interband transitions in the visible range, such as the noble metals like Pt or Pd that have a very broad resonance peak.

To address more complex shapes, analytical solutions that extend Mie's theory for spheres exist for arbitrary spheroids.[140] However, real nanostructures always have more complex shapes and are often placed on substrates that themselves can have complicated surface structure. To simulate the optical properties of such structures one has to rely on numerical solutions to Maxwell's equations.[153] Some examples of methods to do so are finite difference time domain (FDTD),[154] discrete dipole

approximation (DDA),[140] finite element method (FEM), boundary element method (BEM)[155] and the modified long wavelength approximation (MLWA).[140,153] These methods make it possible to predict how individual, or groups of, nanoparticle(s) will respond to an electromagnetic field. Today, one of the most popular methods is FDTD that also has been the tool I used in this thesis to simulate the optical response of various nanostructures I have used. FDTD is discussed further in section 3.4.

LSPR Hybridization

When two (or more) plasmonic nanostructures are placed in close vicinity, the individual resonators couple and modify the resonance condition of the system.[156–158] The interaction between the resonators can be explained by describing the newly formed system as a coupled harmonic oscillator with its own hybrid resonances that closely resemble the hybridization taking place when molecular bonds are formed.[158,159] Similar to the case of molecular bonds, were two orbitals are hybridized to form two new molecular orbitals, one with lower (binding) and one with higher (anti-bonding) energies, the hybridization between two LSPRs results in the formation of two new resonance frequencies with lower and higher energies. In the case of a simple homo-dimer system consisting of two identical spherical particles excited by an electromagnetic field polarized along the dimer axis, the hybridization scheme is summarized in **Figure 3.3**. It shows the original energy levels for the dipolar resonances of the two resonators and the two hybridized states with their corresponding dipoles. From **Figure 3.3** one can see that the case where the two dipoles are oriented in the same direction corresponds to the low energy mode, and the one where they are pointing in the opposite direction is the high energy resonance. Since this higher order resonance has no net dipole moment, it cannot interact with the incoming field of light and is thus not excited, resulting in a so-called "dark" mode. If the incident field is instead polarized perpendicular to the dimer axis, the hybridization will be different and therefore dimer structures have a strongly polarization dependent optical response.

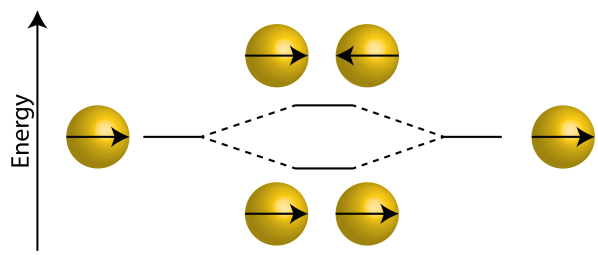

Figure 3.3 Plasmon hybridization. As two plasmonic resonators are placed in close vicinity, their modes can couple to form hybridized modes.

More complex structures consisting of differently sized particles of different materials can also be understood by the same hybridization scheme with some added complexity.[157,160] In the case of differently sized structures consisting of the same

material, the dark mode is no longer totally dark since the two differently sized particle dipoles will not cancel out completely. Additionally, material dependent effects can give rise to new coupling possibilities between free electron resonances and e.g. interband transitions.[157]

In **Paper II**, heterodimer structures consisting of a Au disk placed next to a smaller Cu nanoparticle formed a hybrid resonance. Presented **in Figure 3.4** is an example of the polarization dependent extinction spectra of these nanostructures. Light polarized along the dimer axis is clearly redshifted compared to the orange line, which represents the spectrum for light polarized perpendicular to the dimer axis.

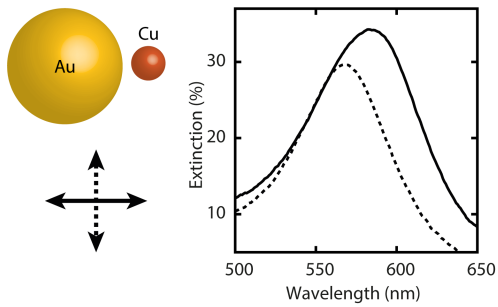

Figure 3.4 Polarization dependent extinction spectra of a heterodimer. An Au-Cu heterodimer structure (left) shows a polarization dependent extinction spectrum due to plasmon hybridization, which results in a lower energy (longer wavelength) resonance for light polarized along the dimer axis compared to light polarized perpendicular to it.

3.3 Plasmonic Sensing

As already mentioned, the plasmonic properties of a metal nanoparticle depend on the dielectric properties of the LSPR active material,[161] the size[162] and the particle's surroundings.[163] A change in one of those properties may induce a change in the optical spectrum. Consequently, by measuring absorption and/or scattering spectra from LSPR active structures, small changes in or around the particle can be detected. This is the basis of what is known as plasmonic sensing that was first demonstrated two decades ago[164] when plasmonic Au particles were used as transducers for detecting antigens binding to ligands attached to the particles. A typical optical change of a plasmonic nanoparticle, measured for instance by extinction spectroscopy, is illustrated in **Figure 3.5**, where a change in the particles surrounding modifies the resonance condition of the LSPR. To quantify the readout, the peak is characterized by some well-chosen parameters, such as the resonance wavelength (λ_{peak}), the intensity (Ext) and the full-width-at-half-maximum (FWHM) of the peak. By tracking how these parameters change over time, one can get information about both transient and steady state properties of the system.[165,166]

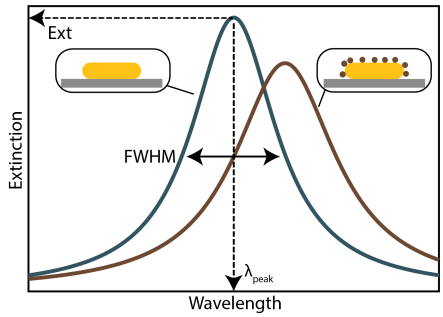

Figure 3.5 Readout of a plasmonic sensor. Changes in the plasmonic particle environment or of the particle itself result in a change of the LSPR condition, which is reflected as a change of the far-field extinction (or scattering) spectrum. Typically, the peak descriptors peak position (λ_{peak}), width of the peak (FWHM) and peak extinction (Ext) are used as readout to track changes.

The use of plasmonic structures as sensors spans a wide set of fields. It is dominated by biological sensors[24,167,168] but has also been used for chemical and gas sensing,[27,169,170] as well as sensing related to catalytic reactions.[22,98,99] Plasmonic sensing has shown to be especially attractive for sensing of solid-state chemical reactions due to the possibility to use it under ambient pressure and at elevated temperatures. Additionally, the measurements can be done in a non-invasive way because only low power visible light is used. Some examples of uses of plasmonic sensing that are of relevance to my work include measurements of the phase transition when Pd and Mg is transformed from a metal to hydride[25,27,142,170–175] and the oxidation of Cu nanoparticles. [176,177]

Another advantage of using LSPR for sensing is that it is only sensitive to changes in a very small volume surrounding the nanoparticle, due to the rapid decay of the induced field away from the surface. Specifically, this sensing decay length is on the order of a few tens of nm at visible frequencies.[168] Furthermore, the field enhancement region around a nanoparticle is determined by how the resonance of the particle is aligned with the polarization of the incoming electric field, as well as by the particle shape (**Figure 3.6**). Optimizing the latter enables tailoring of the sensitivity such that even single molecules can be detected.[23,178]

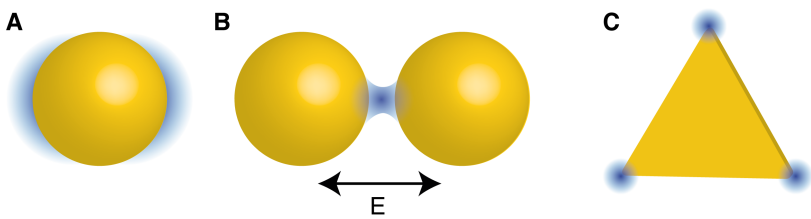

Figure 3.6. Plasmonic field enhancement. Schematic depiction of enhanced electric fields around differently shaped plasmonic nanoparticles. A) Around a spherical structure the field enhancement aligns with the incident polarization of the field. B) Dimer structures form hybrid

resonances, which result in so-called hot spots with highly enhanced field intensities forming between the structures. C) Sharp corners can also result in greatly enhanced field intensities.

3.3.1 Indirect Plasmonic Sensing

To expand the applicability of plasmonic sensing to a wider range of materials the concept of indirect nanoplasmonic sensing (INPS) can be utilized.[179] The main differentiator that distinguishes INPS from "direct" plasmonic sensing is that the optically active component, the plasmonic nanoantenna, is separated from the material to be "sensed" by a thin spacer layer (**Figure 3.7**). This makes it possible to study otherwise non-plasmonic or "bad" plasmonic materials by placing them in close vicinity to a good sensing unit. To date, this approach has been used to study properties of Pd nanoparticles undergoing hydride formation both for ensembles[170] and at a single nanoparticle level,[25–27] sintering of catalytic particles[180] and catalytic reactions[20] to name a few. In this thesis, I have used INPS in **Paper II** to study oxidation of small Cu nanoparticles by using a combined Au and Cu heterodimer, in **Paper IV** to study the hydrogenation of Pd in a Au-SiO_2-Pd structure and in **Papers VI & VII** to study changes in individual Pt nanoparticles during the CO oxidation reaction, by using the Au-SiO_2-Pt arrangement depicted in **Figure 3.7**.

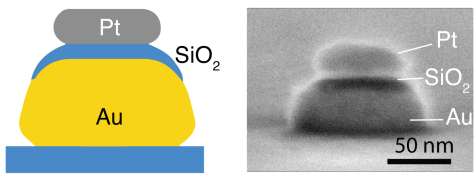

Figure 3.7 Indirect plasmonic sensor. Schematic (left) and SEM micrograph (right) of an indirect nanoplasmonic sensing structure used in this thesis. It is comprised of a Au disk (yellow) used as the sensor to detect changes taking place in the smaller Pt nanoparticle (gray) placed on top. The two particles are separated by a 7 nm SiO_2 spacer layer.

3.3.2 Single Nanoparticle Plasmonics

Today there are several different methods to study LSPRs in individual nanoparticles, each with their own benefits and drawbacks. Here I will try to briefly summarize the main methods and how they work. For a more complete overview, I refer to the literature.[181]

Single particle methods can be separated into two subgroups: near-field and far-field. Near-field methods study the electromagnetic near-field of a particle, meaning that the probing is done on the order of a few to a few hundred nm away from the particle itself. Far-field methods instead measure the fields that propagate far from the particle. The methods to study near-field properties of plasmonic nanoparticles include: (i) scanning near-field optical microscopy, where a mechanical near-field probe (typically an AFM-tip) is inserted in close vicinity to a nanoparticle and excites a plasmon through near-field interaction;[182–184] (ii) photoelectron emission

spectroscopy (PEEM) that studies electrons that are emitted due to absorption of incident photons;[185,186] (iii) cathodoluminescence where photons are emitted due to an excitation from incident electrons;[187] and (iv) electron energy loss spectroscopy (EELS), where the energy lost from an electron due to an LSPR excitation is measured.[188]

The far-field methods instead rely on probing the signal in the far-field, which means that they are inherently diffraction limited. The techniques to study properties of single nanoparticles in the far-field include: (i) dark-field scattering spectroscopy (DFSS), where light scattered from a single nanoparticle is measured; and (ii) photothermal imaging used to study absorption of light.[189] Because of the strong light-matter interaction resulting from LSPR active nanoparticles, scattering measurements of individual plasmonic nanoparticles can be done using relatively simple equipment, consisting of a traditional optical microscope with a dark-field condenser. Additionally, as long as individual nanoparticles are separated by a larger distance than the diffraction limit (i.e. a few 100 nm), they can be seen as individual bright spots in a microscope, which allows for several individual particles to be measured simultaneously.[25,26,190,191] This was utilized in **Paper V** where Cu nanoparticles where placed in a square grid with an inter particle distance of 900 nm. In this configuration, the particles where individually addressable by an optical microscope with a numerical aperture (NA) of 0.55.

One significant limitation of single particle spectroscopy based on scattered light is the fact that scattering from a particle scales as r^6, as shown in eq. 3.3. This means that as the particle size is decreased, the scattering signal will diminish quickly, resulting in difficulties to investigate single nanoparticles with a size smaller than around 50 nm. To overcome this, the previously discussed INPS scheme can be utilized by, for example, placing the small and thus weakly scattering nanoparticle close to a larger, better scatterer to act as a signal trancducer.[25,27]

In this thesis, I have used scattering microscopy and spectroscopy to study the response of individual nanoparticles both in the direct and INPS variants. In the case of spectroscopy, DFSS was used which will be described in more detail in **Chapter 4**.

3.4 Simulating Plasmonic Particles with FDTD

When simulating the electromagnetic response of nanoparticles with plasmonic properties, one of the commonly used numerical methods is the finite difference time domain (FDTD) method. It is also known as Yee's method after it's inventor, and has since 1966 expanded from classical electromagnetics problems to include more novel areas including plasmonics, and nano-optics which is of interest to me.[192] It is, however, beyond the scope of this thesis to explain the details of the FDTD algorithm and therefore I refer to the literature for details.[154] In short, to solve Maxwell's equations in an FDTD simulation, both space and time is discretized and central difference approximations are used to solve the derivatives of the curl equations. The novel solution that Yee proposed was to use a staggered grid, separating the electric and magnetic parts both spatially and temporally.[154]

The reason for the growing use of FDTD lies in its inherent flexibility allowing for arbitrary shapes and material combinations to be simulated. In my work, FDTD has been essential when connecting theoretical physiochemical models with experimental measurements. In addition to far-field spectral information, FDTD can also be used to get near-field information of how the EM-field behaves in the close vicinity of a nanoparticle. All simulations were carried out using the commercial software FDTD Solutions (Lumerical[193]). Some example usages from the attached publications are the optical response of a Cu nanoparticle as it changed from metal to oxide in **Paper II & III**, the optical response of a nanoparticle placed in a nanofluidic channel as the contents of the channel were exchanged in **Paper I** and changes in a Pt/SiO_2 catalyst induced by catalytic reactions in **Paper VII**. In the latter, both the effect of changing the Pt particle itself due to surface oxidation as well and changes affecting the SiO_2 support was investigated. In this context we propose that adsorbed O-atoms could spill over from the Pt catalyst to the SiO_2 resulting in a change in its optical properties. In my case the spillover is solely used as a means of measuring the state of the catalyst

3.5 Application Example: Copper oxidation

To illustrate how plasmonic nanospectroscopy can be used to measure a chemical transformation in a nanoparticle I will here give an example of how it was used to study the oxidation of Cu.

Most metals oxidize when exposed to oxygen. Some metals, like Iron (Fe), oxidize readily in air and Fe turns into brown, crumbly hematite (Fe_2O_3), commonly known as rust. In contrast, when Copper (Cu) is exposed to air it does not crumble. Instead, a thin oxide film forms on the surface of the metal and protects the bulk from further oxidation. If this film consists of Cu_2O, Cu attains its characteristic brown-orange color. The green color, seen in e.g. The Statue of Liberty, stems from different Sulfur containing Cu species.[194] Oxidation has been studied for a long time, and historically, most experimental and theoretical studies have focused on the oxidation of macroscopic samples.[195] With the evolution of nanotechnology, the ability and interest in oxidation of nanostructures have also received significant attention. Regardless of the size of the material studied, the mechanisms governing the oxidation process are inherently nanoscale and to study oxidation, methods capable of resolving chemical changes on the nanoscale are therefore needed. When studying oxidation of nanoparticles, it is of interest to both understand at what conditions oxidation occurs and what the kinetics and underlying mechanisms that control the process are. Here I will thus briefly introduce some concepts relevant to my study of Cu nanoparticle oxidation both under idealized and at catalytic reaction conditions. For a more comprehensive discussion of oxidation of metals in general I refer to the literature. [195]

Oxidation of a metallic nanoparticle is a multi-step process where oxygen first adsorbs on the particle surface, dissociates, interacts with a metal atom and forms the oxide. For a whole particle to oxidize, diffusion has to be involved, where either

oxygen (O^{2-}) diffuses inwards into the particle or metal species (M^{+}) diffuse outwards towards the oxygen adsorbed on the surface. The former mechanism is known as a Valenci-Carter (VC) mechanism and results in an oxidation front that grows from the surface of the particle inwards until the whole particle is oxidized.[196] The latter mechanism involves a net transport of metal atoms outwards, resulting in a void forming inside the particle. This is known as nanoscale Kirkendall effect (NKE).[197] Which of the two mechanisms that dominates in a specific system is determined by the diffusivity of oxygen (O^{2-}) and metal (M^{+}) ions in the oxide film, respectively.

In my work, Cu has played a central role, primarily due to its catalytic properties and the fact that they change dramatically when Cu oxidizes. In this context I have utilized plasmonic nanospectroscopy to probe the oxidation process itself and as operando probe to monitor the oxidation state of Cu catalyst nanoparticles during catalytic reactions. This was particularly important in the study of Cu oxidation presented in **Paper II** where plasmonic nanospectroscopy performed on Au-Cu heterodimer structures (**Figure 3.8A-B**) was used to measure the oxidation of Cu (**Figure 3.8C-E**). The optical measurements were combined with an FDTD model that described the oxidation of a hemispherical Cu nanoparticle (**Figure 3.8F-G**). Specifically, the FDTD model was constructed to represent a Au-Cu heterodimer structure in which changes due to oxidation were simulated as a growing Cu_2O layer and the growth of a central void, as illustrated in **Figure 3.8G**. By comparing the simulated spectra (**Figure 3.8H**) with the experimental spectra (**Figure 3.8E**) the extent of oxidation at any state of the experiment could be determined.

As a natural evolution of this study, experiments performed on single Cu particles were carried out in **Paper III.** In this study, TEM was used in conjunction with plasmonic nanospectroscopy to identify features in the optical scattering spectra that could be directly linked to the formation of a central Kirkendall void.

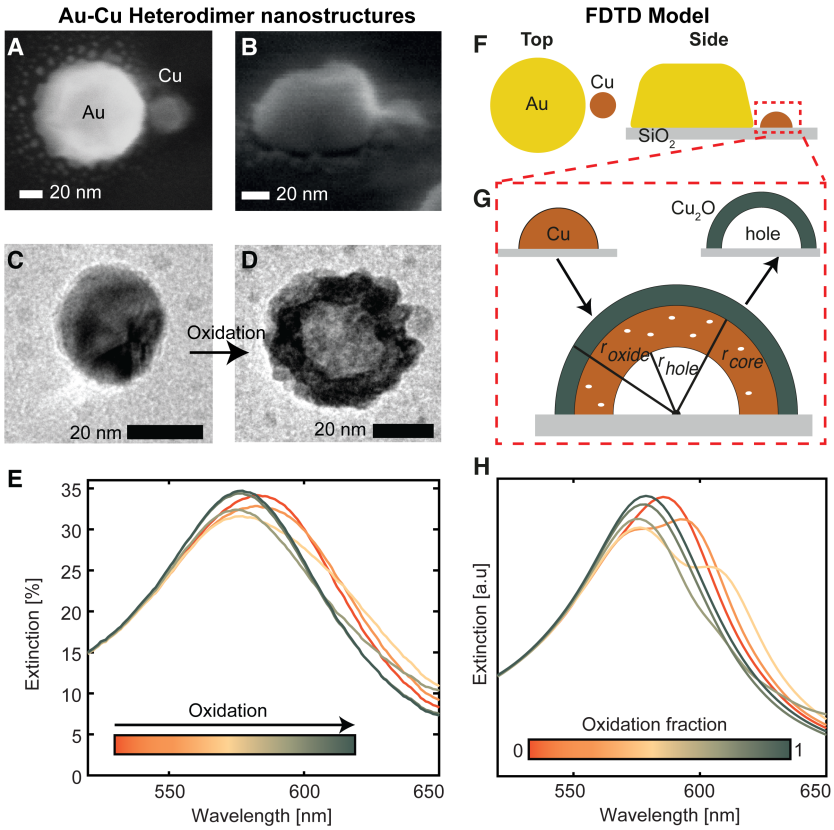

Figure 3.8 Au-Cu Heterodimer for Cu oxidation study. Top- (A) and side-view (B) SEM images of a nanostructure comprised of a larger Au particle placed next to a smaller Cu particle. TEM images of a Cu nanoparticle before (C) and after (D) oxidation in O_2 where a clear void is formed at the center of the particle, indicating a NKE mechanism. E) Extinction spectra measured from a sample containing Au-Cu heterodimer nanostructures at different stages of oxidation. F) Schematic of the structure used in FDTD simulations. G) Schematic of the oxidation process used in the FDTD simulations illustrating the growth of an oxide shell and a central void as a result of the NKE. H) Simulated extinction spectra as a function of oxidation extent.

4 Nanofabrication and Characterization

In his now legendary talk entitled "There's plenty of room at the bottom", Richard Feynman in 1959 envisioned the benefits of being able to manipulate physical objects on the atomic level. Back then, the electron microscope had already been invented and provided the possibility to image objects with nanometer resolution. However, the art of making and manipulating the world at the nanoscale had not yet been explored. Now, almost 60 years later, we have undoubtedly come a long way, where every one of us has one of the miniaturized computers envisioned by Feynman in our pockets.

The progress in nanofabrication and nanocharacterization has given rise to the field of nanotechnology that bridges chemistry, physics, biology and engineering. It has not only resulted in a deeper understanding of the world but also made it possible to make new materials. Furthermore, many of the techniques that I have used to make and characterize samples in this thesis are direct results from the developments in nanotechnology during the past decades. In this chapter, I will go through the main principles of the techniques I have utilized to fabricate and characterize nanoparticles and nanofluidic structures.

4.1 Nanofabrication

Fabrication of structures on the sub-micrometer scale has been a substantial part of this thesis. In this section, the working principle of the applied nanofabrication methods will be discussed.

4.1.1 Lithography

To be able to define different structures on top of or in a substrate, a masking layer can be used to prepare the underlying layer for processing. In nanofabrication, these masks are often made from polymer materials that can be lithographically patterned using different techniques. Often, patterns are generated by exposure to radiation that induces a chemical change, followed by a chemical processing step that selectively removes part of the polymer mask. When exposing the mask to radiation, the maximum resolution (minimum size) of the pattern that can be made is set by the wavelength of the exposing radiation. Therefore, different techniques are used, depending on the desired structures. In general, a lithography process can be divided into the three main steps summarized in **Figure 4.1**. They are:

1. **Coating** the sample with a mask material, typically a polymer applied by spin coating (**Figure 4.1B**).

2. **Exposing** certain areas of the mask to radiation, typically photons (optical lithography) or electrons (electron beam lithography), illustrated in **Figure 4.1C**.
3. **Developing** the exposed mask, resulting in removal of either exposed or unexposed regions. The resulting patterned mask can then be used for further processing (**Figure 4.1D**).

Steps 1 and 2 will be explained in this section, followed by examples of what can be done to further process the sample, once the lithographic mask is in place.

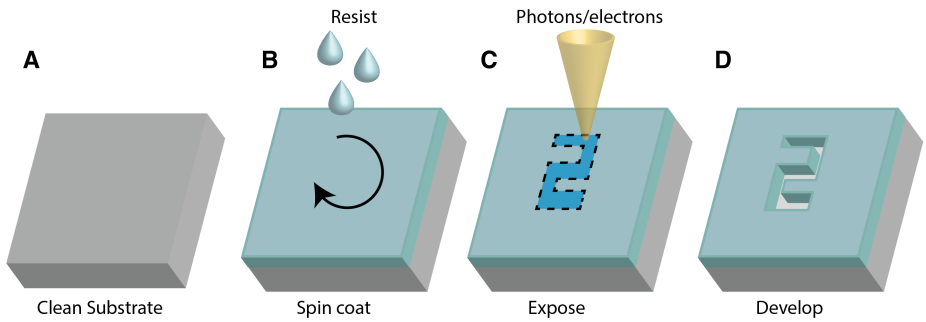

Figure 4.1 Main Lithography steps. Preparing a mask for processing includes (i) a clean substrate (A) is covered by a resist, typically by spin coating a polymer material (B); (ii) exposing the resist using light or electrons to chemically alter the resist layer (C); (iii) developing the resist, effectively removing the exposed areas to make the underlying substrate accessible for further processing (D).

Spin Coating

The first step of a lithographic process is to apply the temporary masking layer to the substrate that is being processed. Typically, this mask is a so-called (photo-)resist consisting of a specific polymer that is spin-coated onto the substrate. Spin coating is a process where a spinning substrate is used to apply a thin uniform polymer layer with a well-known thickness. The process is rather simple as a droplet of the resist material dissolved in a solvent is applied to a horizontally placed sample, followed by acceleration up to a spin-rate of a few thousand rpm, depending on the resist, as well as the desired thickness. Spinning continues for about a minute and is followed by a baking step, were the sample is heated up to evaporate any remaining solvent and solidify the polymer film. The desired film thickness is controlled by modifying the viscosity of the resist solution or varying the spin rate.

Optical Lithography

Optical lithography is based on selectively exposing parts of a light sensitive polymer to UV- or visible light. The exposure results in a chemical change that is followed by dissolving either the exposed or the non-exposed area in a solvent, in what is known as positive and negative lithography, respectively. The light exposure is commonly done either through a pre-patterned photomask or by focusing a laser beam onto the

resist to "write" the desired pattern. Practically, the main difference between using a pre-patterned photomask or a laser writer is that the photomask can be used several times and the exposure process is quick (less than 30s), while the laser exposure scales linearly with the size of the exposed area resulting in around 1h exposure time for a 10 x 10 cm pattern with a modern machine. However, if the pattern is expected to be different for each exposure the laser writer is much more convenient since the pattern can be changed by only modifying a design file instead of having to make a new photomask.

Electron Beam Lithography

EBL is used when the resolution needed surpasses the capabilities of optical lithography due to the diffraction limit of light, and it is the process with the highest possible resolution available today. The reason is that, due to their small wavelength, electrons can be focused to a much smaller spot than photons. Hence, they can be used to make patterns with a resolution on the order of a few nanometers.[198] The working principle of an EBL system is that an electron beam is focused onto a substrate by a series of magnetic lenses that both shape the beam, as well as control its position. A modern EBL system typically relies on a thermal field emitter using Zr/O/W to supply a stable electron beam at variable currents.[199]

The resolution limit in EBL comes not from the actual wavelength of the electrons that is in the picometer range when using a 100 kV acceleration voltage. Instead it is dictated by how the electrons travel through the resist, as it is exposed. Since the electrons will scatter both from the resist material itself and from the underlying substrate, it results in an area larger than the beam size being exposed. In addition, secondary electrons with energies up to 400 eV are generated as the primary electrons are slowed down when traveling through the resist material. These electrons have a traveling distance of 5-10 nm and will expose the resist surrounding the primary electron beam, which is one of the major causes for the limited resolution. These effects also must be taken into account when structures are written close to each other since exposing one of the structures can lead to partially exposing the neighboring structures as well. This is called the proximity effect.[200]

The basic steps of an EBL process follow the scheme illustrated in **Figure 4.1** and are as follows: 1) Spin-coat a substrate with a polymer resist that is sensitive to electron exposure. 2) Align the sample using predefined alignment marks to calibrate the machine to the positions of the sample. 3) Irradiate the sample with an electron beam at the positions defined by the user. The irradiation chemically alters the resist. 4) Develop the exposed mask in an appropriate developer liquid causing the exposed (or un-exposed) areas to dissolve, leaving a patterned resist for further processing.

Although EBL is the process of choice in nano- and micro-fabrication when the highest resolution is needed, it does not come without drawbacks. The major one is the long writing time that makes large area patterning for industrial purposes extremely costly or even impossible.

4.1.2 Etching

Removal of material can be used as a means of patterning a surface. In micro- and nanofabrication, different types of etching are used to remove specific materials. Etching methods can be roughly grouped in two main categories: wet etching and dry etching. The former relies on liquid (wet) chemicals to remove materials, and the latter on gaseous molecules (often in the form of ionized plasma) to physically remove material and/or chemically react with the substrate. Another important classification of etching processes can be made between isotropic etching methods that etch with a similar rate in all directions and anisotropic etching that etches differently, depending on etching direction (**Figure 4.2**).

Wet Etching

Thanks to years of development within chemistry there exists a lot of knowledge about how different materials react with other chemical species. This knowledge is today readily accessible in various databases and allows one to rapidly identify which combination of materials that could be used to effectively protect and etch different parts of a sample.[201] Depending on the system, wet etching can be isotropic or anisotropic, e.g. depending on the crystalline orientation of a substrate.

Dry Etching

Reactive ion etching (RIE) is the most common dry-etching method and makes use of reactive ions to etch away different materials. Depending on the choice of ionic species, different materials can be etched selectively. When designing an etching process, it is important to consider the relative etch rates between the material used as a mask and the material that is to be etched. These rates can be found in the literature.[201] RIE can also make use of physical etching by accelerating ions towards the substrate to remove material due to the physical impact of the ions.

To initiate the etching process, a sample is typically placed inside a vacuum chamber with a controlled gas environment. A plasma of the chosen gas is ignited, creating a mix of atoms, ions and free electrons in the chamber. Due to their higher mobility, the free electrons will quickly accelerate towards the anode of the chamber and the positive ions left behind will therefore start accelerating towards the cathode, where the sample to be etched is placed. Upon impact, these accelerated ions will physically knock out atoms from the substrate, thereby causing an etching effect. At the same time, the highly reactive ions will react with the substrate material creating volatile gaseous species that are pumped out of the chamber. In this process, one can also tune the degree of chemical (reactive) and physical etching to achieve more or less anisotropic results, as illustrated **in Figure 4.2**.

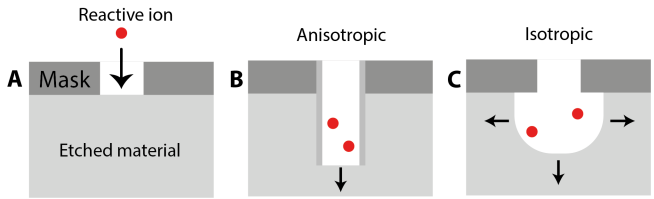

Figure 4.2 Reactive ion etching. A) A reactive molecule is ionized and accelerated towards the substrate by an electric field. Depending on the process parameters an anisotropic B) or isotropic C) etching profile can be achieved. To achieve deep anisotropic etching one can utilize a polymer to protect the sidewalls, as schematically depicted by the grey regions that cover the walls of the trench in B).

One of the more specialized processes used to achieve deep anisotropic etching into Si is known as the Bosch process or as deep reactive ion etching (DRIE).[202] The process works by cycling between an etching step and a passivating step that protects the surface from the reactive gases. The first step in the process is to passivate all surfaces with a polymer that is resistant to the reactive gas mixture used in the etching step. The second step involves etching by both sputtering and reactive ions. The role of sputtering is to remove the protective polymer film. Because this sputtering effect is controlled by an applied forward voltage it is directional and thus only etches surfaces that are perpendicular to the direction of the accelerated ions. The protective polymer will thus remain only on the sidewalls of previously etched trenches (**Figure 4.2B**). In regions where the protective polymer has been removed, the reactive ions will etch the substrate. As the result, a trench that is being etched will be etched only in the direction normal to the sample surface, resulting in strongly anisotropic etch profiles. These two steps are cycled until the desired etching depth is achieved.

Reactive ion etching was used to make the micro- and nanochannel systems in **Papers I, IV, V** & **VII**. For the nanochannels etched into SiO_2, a fluorine based RIE process was used. For the deeper microchannels, as well as for the inlet holes that were etched into Si, DRIE was used. RIE with O_2 was also used to selectively remove polymer resist materials in the hole-mask colloidal lithography process (discussed in detail in section 4.1.4) to make nanostructures for **Paper II**.

4.1.3 Thin Film Growth

Another way of patterning surfaces is to add material instead of removing. Here, different ways of adding materials will be discussed in terms of growing thin films.

Thermal oxidation

One way of growing a thin film onto, for instance, Si is by thermally oxidizing it in a controlled way to form a thin film of SiO_2. This thermal oxidation can be achieved in two ways called wet or dry oxidation, depending on if the oxidation is done in the

presence or absence of water, respectively. The corresponding reaction schemes look as follows:

$$Si\ (s) + O_2(g) \rightarrow SiO_2(s) \text{or}$$

$$Si(s) + 2H_2O(g) \rightarrow SiO_2(s) + 2H_2(g),$$

where *g* and *s* correspond to solid and gas phase, respectively.

The oxidation of a clean Si wafer takes place in a furnace with a temperature of typically 800 – 1200 °C, were the wafer is exposed to an oxidizing atmosphere containing O_2 or H_2O. The relationship between oxide thickness and time is a function that is strongly dependent on temperature, pressure and what crystal orientation is to be oxidized. The equations governing this process are well known and online tools for process planning are readily available.[203,204]

Thin film deposition

There exist several ways to grow materials onto a substrate with thickness control at the nanometer scale.[205] Here, I will briefly discuss the thin film deposition methods relevant to this work.

Chemical vapor deposition (CVD) relies on inducing a chemical reaction on the surface of a sample. This is done by introducing reactants in the gas phase in a vacuum chamber, where they adsorb to the sample surface and react to form the deposited material. CVD is typically used to deposit oxides or nitrides. In my work, plasma enhanced CVD (PECVD) was used to deposit silicon nitride (SiN_x) by a reaction between silane (SiH_4) and N_2 assisted by a plasma. These nitride films were used as electron transparent windows for TEM imaging of nanostructures.

Physical vapor deposition (PVD) relies on the condensation of vaporized atoms and clusters on a substrate. Materials that are deposited using PVD are often metals, metal oxides or nitrides that are vaporized either through thermal evaporation, electron beam evaporation or by sputtering atoms from a source/target that is placed in vacuum together with the substrate that is to be coated.

In *sputtering* the atoms or clusters are created by bombarding a target of the desired material with ions (typically Ar) that knock out target species. The ions are generated using plasma and are accelerated towards the target using an electric field. Some of the ejected atoms will then travel through the chamber and hit the substrate where they are deposited.

In contrast, *evaporation* relies on heating the source material until the vapor pressure is high enough that atoms exit the source and travel (in vacuum) through the deposition chamber to eventually condensate when landing on the sample surface. Heating of the target is done either resistively or by an electron beam. Because an electron beam can be tuned to very high energies and focused into a small spot size, it can create extremely high target temperatures and is thus used to evaporate materials with high melting temperatures such as tungsten, carbon or alumina. In contrast to CVD, deposition done by evaporation is very directional. This results in

highly anisotropic deposition profiles where only areas in direct line of sight of the target will be covered.

In this thesis, evaporation based PVD was used for the growth of the nanostructures in all appended papers, as well as for the fabrication of the resistive heaters on the nanoreactor chips.

4.1.4 Hole Mask Colloidal Lithography

One challenge with conventional lithography (and EBL in particular) is to pattern large areas (~cm^2), while still maintaining nanometer precision. Using conventional optical lithography, the resolution is limited by the diffraction limit, and structures below a few 100 nm are hard to obtain. At the same time, the higher resolution of EBL is limited by the fact that exposure time scales with an increase in exposed area. A solution to these limitations is to use self-assembly based methods that rely on nanostructured objects arranging themselves on a surface, meaning that the process is naturally parallel rather than serial. One such process that uses colloidal suspensions of nanostructures for patterning is colloidal lithography (CL).[206] In this chapter I will specifically discuss a variant of CL that has been developed at Chalmers and is known as Hole-mask colloidal lithography (HCL).[207]

HCL utilizes charged polystyrene (PS) beads that are self-assembled on an oppositely charged substrate, resulting in a quasi-randomly spaced scarce monolayer of PS on the underlying substrate.[207] The fabrication steps are presented in **Figure 4.3** and are as follows: 1) The substrate is cleaned with acetone, isopropyl alcohol (IPA) and methanol, each solvent followed by immersing the beaker in an ultrasonic cleaning machine for 3 minutes. 2) Poly(methylmethacrylate) (PMMA) is spin coated on the substrate followed by baking on a hotplate at 170°C for 10 minutes to evaporate any remaining solvent. 3) A short etch by oxygen plasma is performed on the PMMA to reduce the hydrophobicity of the substrate. 4) Poly(diallyl dimethylammonium) (PDDA) in water solution is drop coated on to the surface for 40 seconds, followed by rinsing in deionized water. This creates a thin positively charged layer on top of the PMMA. 5) A dispersion of polystyrene (PS) particles in water is drop coated on to the surface for 3 minutes, followed by 20 seconds rinsing in deionized water. The concentration of the PS solution can be varied to be able to control the surface coverage of the final structures.[208] The PS particles have a negative surface charge and therefore attach to the positively charged PDDA surface, while at the same time repelling each other. This results in PS particle coverage with a defined nearest neighbor distance but without long range order. 6) A thin film (around 20 nm) of a material of choice (typically Cr or Au) is deposited by evaporation onto the surface covered with PS. 7) Tape is placed on top of the covered surface. When removed, the tape will strip the PS particles, leaving a mask with holes defined by the PS particle diameter where the underlying PMMA is exposed. 8) Oxygen plasma etching through the holes in the metal mask transfers the hole pattern into the underlying PMMA. In this step, longer etching time results in a larger undercut, meaning that the PMMA is etched parallel to the substrate surface to create a hole that has a larger diameter than

the hole in the mask. 9) By evaporating materials through the holes, structures are formed on the substrate surface with a shape determined by the hole. 10) After completing the evaporation, the mask is removed by dissolving the PMMA using acetone in a lift-off step. This results in removal of all material that is attached to the PMMA layer, leaving only the material that is deposited directly on the substrate.

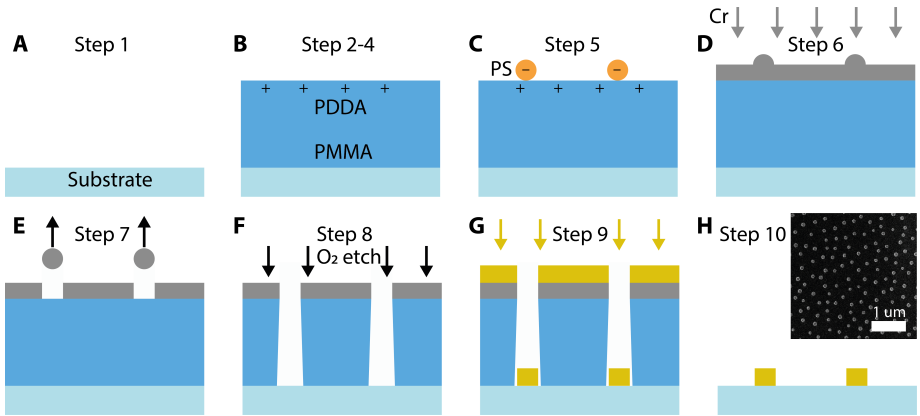

Figure 4.3 Hole-mask colloidal lithography fabrication steps. A) Substrate is cleaned. B) PMMA is spin coated on the substrate and the surface is made positively charged by adsorption of a polyelectrolyte (PDDA) layer. C) Polystyrene beads with opposite charge to the PDDA are self-assembled on the surface from aqueous solution. D) The mask layer of Cr or Au is deposited by PVD. E) Tape is used to strip away the PS beads, leaving holes in the metal mask. F) Holes are etched through the PMMA layer using reactive ion etching. G) The desired structure material is deposited by PVD. H) The PMMA is dissolved resulting in the top layer being lifted off, leaving the substrate patterned with nanoparticles. The inset shows an SEM image of an array of 100 nm Au disks fabricated using HCL.

4.1.5 Shrinking Hole Colloidal Lithography

A variation of the HCL process known as Shrinking Hole Colloidal Lithography (SHCL) has been developed to be able to create complex nanostructures, such as multimers of different size and material.[209] SHCL utilizes the fact that the PMMA layer can be under-etched in step 8 (**Figure 4.3F**), and that by depositing material at an angle, several particles can be placed consecutively through the same mask in a self-aligned way. Because each deposition will cause a slight shrinking of the hole in the mask, consecutive depositions will furthermore result in slightly smaller structures. An example of the SHCL process is presented in **Figure 4.4**, were the first material (Au) is deposited at an angle placing the disk slightly off center. Following this deposition, a layer of Cr is deposited at a high angle (45°) while rotating the sample, resulting in the Cr only getting deposited on the PMMA walls, as well as on top of the Au mask-layer. The purpose of this layer is to only shrink the size of the hole without leaving any material on the substrate. The third deposition is subsequently done at a small angle opposite to the angle used for Au, resulting in a

smaller Cu particle placed next to the Au. This technique was used to create the Au-Cu heterodimer arrays for plasmonic nanospectroscopy of Cu oxidation in **Paper II**.

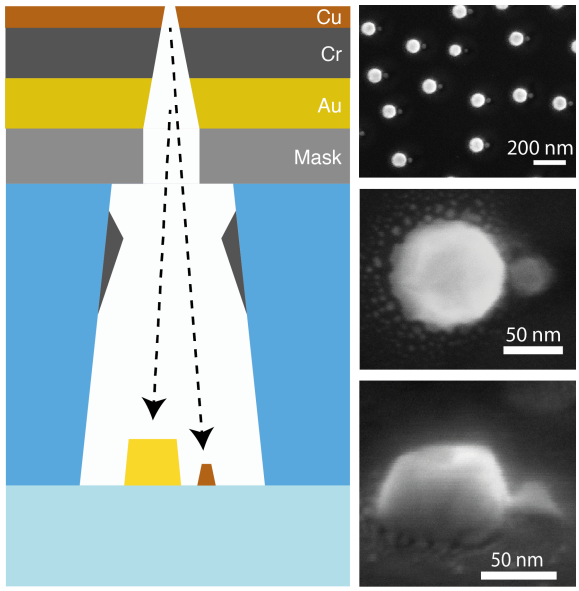

Figure 4.4 Shrinking hole colloidal lithography. By depositing material at an angle and utilizing the fact that the hole in the mask shrinks during deposition, multimer structures can be fabricated from a HCL mask. First, Au (yellow) is deposited, followed by Cr (dark grey) that is deposited at an angle while rotating the sample so that the material ends up on the PMMA walls. Lastly Cu (orange-brown) is deposited at a small angle through the smaller hole. To the right, three SEM images of Au-Cu heterodimer(s) are presented, showing the obtained structures viewed from the top (top two) and from the side (bottom).

4.1.6 Nanofabrication of the Nanoreactor Chip

The general nanofabrication scheme for the nanoreactor chips I have developed is summarized in **Figure 4.5** with the main steps as follows: 1) Oxidizing a 4 inch, p-type, Si wafer by thermal oxidation to a desired oxide thickness (typically 100-300 nm). 2) Defining nanochannels into the oxide using electron beam lithography (EBL) and reactive ion etching with NF_3 to etch SiO_2 to the desired depth. 3) Defining larger microchannels using optical lithography, etching through the SiO_2 using RIE or a HF-based wet-etch, followed by DRIE with C_4F_8 used for passivation and CF_6 to etch into the Si. 4) Making holes through the Si wafer to enable connecting an external gas or liquid supply from the face of the chip. The holes are made in the same way as the microchannels but etching using DRIE for a longer time. 5) Fabricating a heater by patterning a mask on the back of the chip with optical lithography and depositing a 10 nm Cr layer, followed by 100 nm Pt, using electron beam evaporation. 6) Fabricating nanoparticles in the nanochannels by defining a mask using EBL and depositing the desired material using electron beam evaporation. 7) Sealing the chip

by fusion bonding[210] a glass wafer to the top of the Si/SiO_2 chip at 550°C. This process relies on the fact that when two perfectly clean and flat SiO_2 surfaces come in contact at this temperature, covalent bonds are formed between the two surfaces. 8) The chip is cut into the desired shape using a dicing saw.

Each 4" Si wafer is used to make 16 chips that can be individually patterned with different nanoreactor designs and filled with different catalysts. In this way several experiments can be prepared in parallel to avoid differences related to different batches.

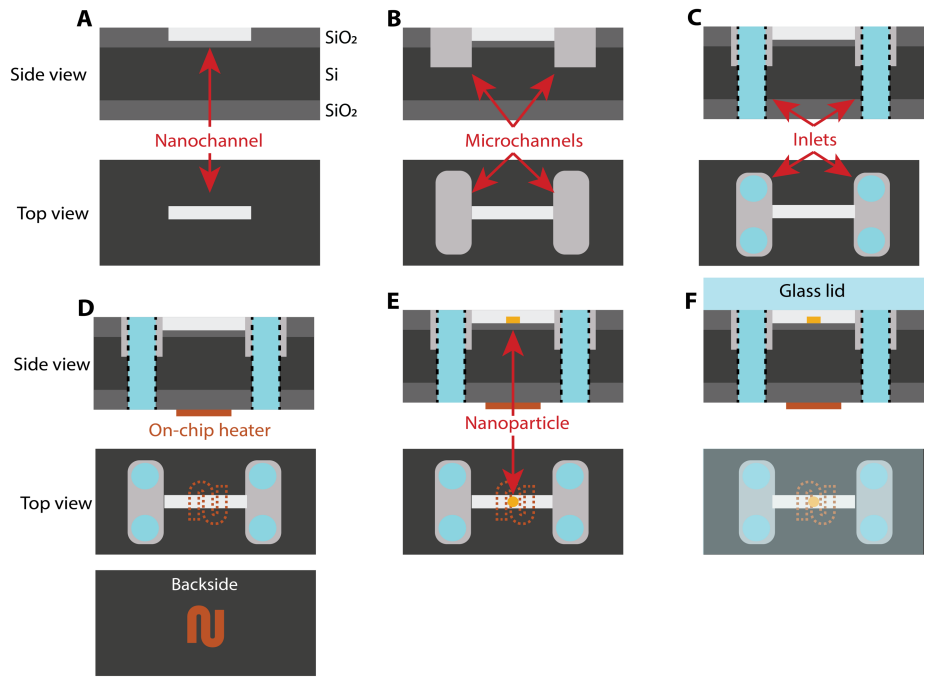

Figure 4.5 Main nanofabrication steps for making a nanofluidic chip for single particle catalysis. A) Nanochannels are fabricated into 200 nm thermal oxide on a Si wafer by EBL followed by RIE. B) Larger microchannels are then made by optical lithography followed by RIE/DRIE through both the SiO_2 and into the Si. They connect to the nanochannels. C) Inlet holes to the microchannels are defined by optical lithography and etched using DRIE through the Si wafer. D) (If needed) a resistive heater is placed on the back of the chip by Pt evaporation through a mask defined by optical lithography. E) Nanoparticles are fabricated inside the nanochannels by evaporation through a mask that has been patterned by EBL. F) A glass lid is fusion bonded on top to seal the channels.

4.2 Characterization Techniques

I have used many different characterization techniques to get information about my samples. This section summarizes my most used techniques and discuss their mode of operation. The techniques include electron microscopy, used for imaging of nanoscale objects, X-ray photoelectron spectroscopy (XPS) for identifying the composition of nanoparticles, optical spectroscopy used for in situ characterization of nanoparticles and mass spectroscopy used for identification of gas phase composition during catalytic reactions.

4.2.1 Electron Microscopy

One of the most widely used techniques to image matter on the nanoscale is electron microscopy. As the name implies, it relies on electrons to probe a sample which results in a higher resolution than optical microscopy due to the short wavelength that electrons can have. However, electrons also suffer from a much shorter mean free path in matter compared to photons. Therefore, electron microscopes typically require the sample to be placed inside a vacuum chamber to minimize the number of gas molecules between the electron emitter and the sample. Inside solids, electrons scatter even more and imaging structures enclosed in e.g. a catalyst is therefore not possible.

When an electron beam hits a sample, several processes occur, and the resulting signals are summarized in **Figure 4.6**. The elastically scattered electrons, known as backscattered electrons (BSE), have lost little to no energy during their interaction with the sample and thus have the same energy as the incident beam. The yield of BSE is strongly dependent on the molecular weight of the material and thus gives good chemical contrast of the sample. Examples of this contrast can be seen in most SEM images presented in this thesis, e.g. **Figure 4.4**, where the heavier metals (Cu & Au) appear brighter than the underlying Si. Secondary electrons (SE), on the other hand, are electrons that have been ejected from an atom in the sample due to an inelastic interaction with the primary beam. The kinetic energy of these electrons is typically less than 50 eV, which limits their travel distance through a solid material to a few nm. Therefore, SE can only originate from atomic layers close to the sample surface and they are used to get topographic information.

When an electron is emitted by an atom due to interaction with the primary electron beam, the empty energy level will quickly be filled by an electronic transition of an electron in a higher energy state. The energy lost in this transition can result in emission of a photon in the X-ray range or an Auger electron. Since the possible electronic transitions of each element are unique, compositional information of the sample can be collected through what is known as energy dispersive X-ray spectroscopy (EDS or EDX). Additionally, the energy lost by electrons of the primary beam can be studied by electron energy loss spectroscopy (EELS). The EELS spectrum is specific to each element and can therefore be used for compositional mapping of the sample.

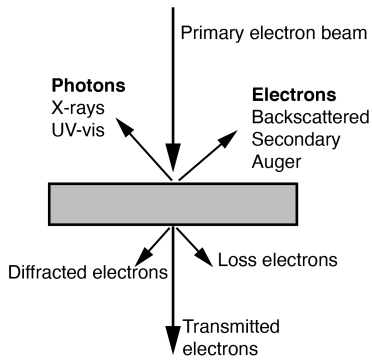

Figure 4.6 Electron microscopy. As the primary electron beam hits the sample, several signals are generated and can be detected.

The two main sub-techniques of electron microscopy are scanning electron microscopy (SEM)[211] and transmission electron microscopy (TEM).[212] SEM utilizes a focused, raster-scanned beam and electrons traveling backwards from the sample (BSE, SE) are monitored. The sample investigated by SEM should generally be conductive to avoid the accumulation of charge on the surface. Such charge accumulation will otherwise deflect incident electrons and distort the image. To enable imaging of non-conductive samples, a thin film of a conductive material can be applied on top of the sample.

In TEM, electrons transmitted through the sample are used for imaging. As a consequence, the sample has to be thin enough to let electrons travel through. The incident beam can be either wide, illuminating the whole sample at once to generate the image, or it can be swept over the sample as in the SEM in what is known as scanning transmission electron microscopy (STEM). Between TEM and SEM, the former achieves the highest spatial resolution and can even be used to image individual atoms, while SEM has a typical resolution down to 1 nm.

A TEM operates similar to a normal optical microscope, where a wide beam of electrons is used to probe the sample. A “bright-field” image is created by studying the transmitted electrons where image contrast stems from the density and thickness of the sample. Regions with more material, or containing material of higher atomic number, appear darker than regions with less material. A dark-field image is created by studying electrons that have been diffracted in specified directions and can therefore give information about the crystal lattice.

TEM is heavily used in catalysis, mainly for pre- and post-reaction analysis of catalysts where it is typically used to investigate the size and distribution of nanoparticles. As mentioned in Chapter 2, a TEM cannot operate at ambient pressures due to scattering

of electrons from gas molecules. However, in situ TEM has been realized by e.g. utilizing miniaturized reactor cells with thin electron transparent windows. This has resulted in fascinating direct visualizations of catalyst nanoparticles changing shape under reaction conditions at ambient pressure.[56] A limitation of TEM stems from the fact that higher resolution imaging comes at the cost of a reduced field of view. Typically, only a handful, of nanoparticles can be studied simultaneously if atomic resolution is needed. Moreover, because TEM utilizes high energy electrons, the energy deposited in the sample can interfere with chemical reactions. For example, the reduction of oxidized Cu has been observed as a result of TEM imaging.[213] Therefore, when performing operando characterization, care must be taken to assure that the observed particle properties are not an artifact of the measurement.

In this work, SEM has been heavily used to image samples during and after fabrication, as well as to characterize the samples after being exposed to e.g. chemical reactions. TEM has been used ex-situ to study the oxidation state of Cu in **Paper II**, **III**, **IV** & **V** and the morphology of Pt nanoparticles in Paper **VI** & **VII.** All TEM analysis was performed by my colleague Sara Nilsson.

4.2.2 X-ray Photoelectron Spectroscopy

X-ray photoelectron spectroscopy (XPS) relies on the photoelectric effect, where an atom absorbs a photon resulting in the emission of an electron that can be detected (**Figure 4.7**). If the absorbed photon energy is higher than the binding energy of an electron, the electron will get emitted with a kinetic energy

$$E_k = h\nu - E_b - \emptyset_S \tag{4.1}$$

that can be detected. Here $h\nu$ is the photon energy, E_b is the binding energy of the electron and $\emptyset_S$ is the work function of the detector. Therefore, an ejected electron will have a kinetic energy that is determined by its binding energy. In addition to the photoelectrons, Auger electrons can be emitted. Auger electrons are generated when an electron from an outer shell fills the hole in a previously excited inner shell. The energy released when this electron relaxes is taken up by another electron that in turn is emitted from sample with a kinetic energy that is characteristic of the element.

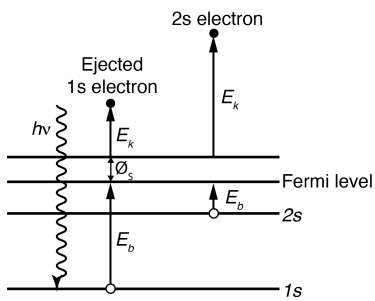

Figure 4.7 X-ray photoelectron generation. If an incident photon has enough energy ($h\nu$) to overcome the binding energy of an electron (E_b), the electron is ejected with a kinetic energy (E_k) corresponding to eq. 4.1.

In an XPS measurement X-rays with a fixed energy are used. The X-rays in laboratory instruments are typically generated from a Mg K_α (1253.6 eV) or Al K_α (1486.3 eV) source,[7] and the intensity of emitted electrons as a function of kinetic energy in the interval 0 ~ 1 eV is collected. The kinetic energy is typically converted to binding energy via eq. 4.1. Because the binding energy of electrons is material specific, XPS is useful for identifying the elemental composition of samples. The binding energy is also modified by the chemical state of the atom which makes XPS useful for determining the oxidation state of a sample. Furthermore, the mean free path of electrons in a solid, in the considered energy range, is typically less than 2 nm.[7] Therefore, the detected photoelectrons stem from the outer most atomic layers, making XPS a highly surface sensitive technique.

The spatial resolution of an XPS measurement is determined by the spot size of the X-ray beam and the acquisition time is largely determined by the photon flux. In a lab scale XPS system the spot size is typically > 10 um and measurements typically take a few to several minutes. By utilizing high flux sources, e.g. synchrotron light, both the temporal and spatial resolution can be improved significantly and a spatial resolution of approximately 10 nm has been demonstrated.[214] Just as in electron microscopy, XPS is traditionally limited to operation under UHV to avoid electron scattering from gas molecules. Efforts to enable in situ/operando XPS include the use of microreactors and the use of differential pumping[69] which was discussed in Chapter 2.

In my work, XPS has been used ex-situ to identify the oxidation state of Cu in **Paper II, III, IV** & **V** and to study Pt in **Paper VI**.

4.2.3 Optical Characterization

The optical analysis of nanoplasmonic structures is one of the main themes of my work and different types of optical characterization methods have been utilized to study both ensembles and individual nanostructures.

Spectrophotometry

Spectrophotometry is used to characterize how a material interacts with light in the UV-visible-NIR range of the electromagnetic spectrum. When shining light onto a sample, the light-matter interaction will result in three possible events: transmission, scattering or absorption. To measure the extent of these processes a spectrophotometer can be used. The working principle of a spectrophotometer is that an incident beam with a well-known intensity is irradiated onto a sample. By measuring the intensity ($I(\lambda)$) as a function of wavelength for light that has interacted with the sample and comparing it to the incident light intensity ($I_0(\lambda)$), the transmission spectrum can be attained as $T = \frac{I}{I_0}$. The extinction spectrum, defined as the sum of absorption and scattering, is related to the transmittance as $E = 1 - T$ and thus corresponds to how much light has been absorbed or deflected (scattered) from traveling in forward direction. As discussed in Chapter 2, plasmonic nanoparticles in the commonly used size regime (~100 nm) exhibit both scattering and absorption.

Therefore, to be able to distinguish between light that has been scattered or absorbed, additional measurement methods must be employed, e.g. measuring absorption alone using an integrating sphere.

Dark Field Scattering Microscopy and Spectroscopy

Dark field microscopy is a technique that is used to quantify light scattered from the sample surface, rather than relying on light absorption, as in more common bright field microscopy. To achieve dark field illumination the specimen of interest is illuminated in such a way that the direct incident light is not transmitted or reflected into the objective of the imaging light path. This is typically achieved by illuminating the sample from a sufficiently high angle, such that incident or reflected light is not collected by the objective. Hence, the so-called dark field image that is obtained, is created only by light scattered (or emitted e.g. by fluorescence) by the sample, as illustrated in **Figure 4.8**.

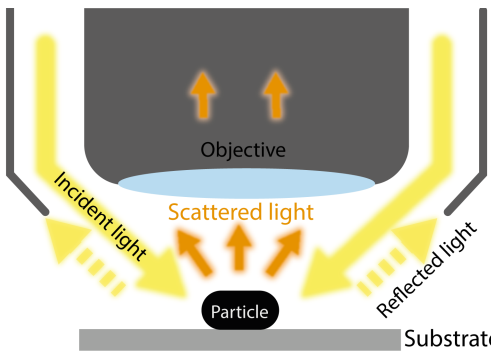

Figure 4.8 Dark field microscopy. By illuminating the sample at a high angle, the reflected incident beam does not end up in the imaging path (objective) and only scattered light is collected by the microscope.

Plasmonic nanoparticles, although much smaller that the wavelength of visible light, scatter light strongly at their plasmonic resonance. Their scattering spectrum is highly dependent on the material, shape, size and electronic surroundings of the nanoparticle, as discussed in chapter 3. Accordingly, single metallic nanoparticles down to a size of a few tens of nanometers can be resolved as distinct individual scattering point-sources in a dark-field optical microscope, **Figure 4.9A**. By focusing them onto a spectrometer with a grating that separates the light into its wavelength constituents it is thus possible to spectroscopically analyze the scattered light of individual plasmonic nanoparticles (**Figure 4.9B**) in what is known as dark field scattering spectroscopy (DFSS).

To correct for scattering from the substrate, as well as for the wavelength dependence of the lamp and the detector, a corrected scattering spectrum (**Figure 4.9C**) is obtained as

$$I_{scattering} = \frac{I_{particle} - I_{background}}{I_{lamp}} \tag{4.1}$$

where the subscripts particle, background and lamp stand for the raw scattering counts measured over an area containing a particle, without a particle and the corresponding lamp spectrum, respectively.

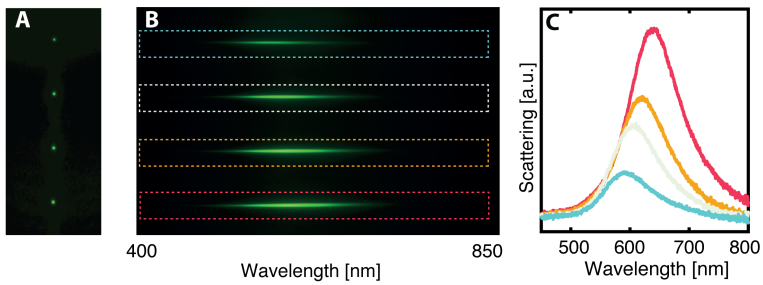

Figure 4.9 Dark field scattering spectroscopy. A) Dark field scattering image of 4 nanoparticles seen through a 50× objective of an optical microscope. B) The same four particles resolved as a function of wavelength by inserting a grating in the light path between the microscope and the camera. C) The corrected scattering spectra from the 4 particles outlined in (B).

When utilizing a grating to resolve the single particle spectra, particles must be placed in a relatively well defined (vertical) line, and the field of view is thus limited to one dimension. Although clever calibration approaches have be used to account for horizontally displaced particles,[215] the measurements are typically limited to fewer than 100 particles. To expand the capabilities of scattering spectroscopy to 2D, methods that combine 2D imaging with 1D spectroscopic information to create 3D (x,y,λ) images can be utilized. These techniques are known as hyperspectral imaging techniques[216] in which a combination of light sources and/or filters are used to take a series of 2D images of the object at a desired number of wavelength points. In this way, the acquisition of spectral information is spread out in time instead of space, as for the grating-based spectrometers. Consequentially, acquiring > 1000 wavelength points (a typical number for grating based DFSS), would take 1000 times longer time for hyperspectral imaging if the same exposure time is used for each image. Therefore, the choice between hyperspectral imaging and grating based DFSS depends on the specific requirements of the experiment. If high spectral resolution is required, grating based spectroscopy is preferred, while 2D hyperspectral imaging offers a significantly larger field of view and thus the ability to readily study > 100 particles.[217] By reducing the number of wavelength points, the acquisition speed of a 2D imaging technique can be maximized. In its simplest form, imaging utilizes only a single image corresponding either to measurements from a well-defined wavelength or integrated scattering from a wide wavelength range, e.g. the whole visible range.

For my work both imaging and spectroscopic studies of both ensembles and single particles were used. Often the experiments took place over long times (several hours) and the optical response was recorded continuously by gathering optical information at pre-defined time steps. Spectroscopy of up to 21 nanoparticles was performed in **Papers I,III,IV,VI** & **VII**. Imaging was used in **Paper I**, based on particle scattering light from a HeNe-laser, and in **Paper V** integrated white light scattering of individual Cu nanoparticles was used to study 1000 particles in parallel during a catalytic reaction.

4.2.4 Mass Spectrometry

Mass spectrometry (MS) is an analytical method used to measure the molecular or atomic composition of a sample. For this thesis, I used it to analyze gas phase composition in what is known as residual gas analysis (RGA). A mass spectrometer works by ionizing molecules and separating them, depending on their specific mass to charge ratio (m/z). Ionization of the molecules can be achieved in different ways, e.g. by exposing them to high-energy particles (electrons or ions), thermally, by electric fields or by laser irradiation. After ionization, the ions are separated based on their m/z by the mass analyzer.

The separation can be done using different methods that all rely on the fact that the trajectory and velocity of an ion accelerated in an electric field depends on its mass and charge. After the mass separation the species with the selected mass hit a detector that is used to count the number of ions, typically using a Faraday cup or an electron multiplier. In this chapter, I will briefly discuss the basic principle of a mass analyzer used in mass spectrometry. For a more detailed description I refer to the literature.[218]

Mass analyzer

The kinetic energy (E_k) gained by an ion with charge q when moved through a field with a voltage U is:

$$E_k = Uq = Uze \tag{4.2.1}$$

where e is the electron charge and z is an integer corresponding to a number of electrons. This can be translated to the velocity gained by the ion with mass m_i

$$v_i = \sqrt{\frac{2ezU}{m_i}} \tag{4.2.2}$$

which shows that the velocity gained by a heavier ion is lower than by a lighter one if they both have the same charge. Hence, the simplest type of mass separation technique is based on the time it takes for an accelerated ion to travel a certain distance and is known as a time of flight (TOF) mass spectroscopy.

A different approach to separating masses is the quadrupole mass spectrometer *(QMS).* In a QMS the mass separation takes place by injecting an accelerated ion into a mass filter that consists of four parallel rods under a combined DC and AC potential,

with the same potential applied to an opposing pair of rods (**Figure 4.10**). An ion traveling through the mass filter will thus have a trajectory dictated by the applied potential and can be described by solving the Mathieu equations.[218] If the parameters are tuned in a way that results in the ion not hitting any of the rods, it will pass through the filter and is detected by the detector. The conditions for achieving this are very precisely defined, which allows a QMS to separate ions by their m/z ratio.

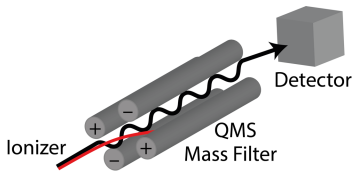

Figure 4.10 Quadrupole mass filter. A combined DC and AC potential is applied to four parallel rods and determines the trajectory for ions travelling between them. Depending on the m/z ratio, an ion will either hit one of the rods (red line) or pass through (black line) the filter and reach the detector.

In both TOF and QMS mass filters, the ratio m/z is what identifies the specific ion. This means that singly ionized molecules with the same original mass will behave identically in the mass filter. Hence, two different molecules with the same mass, e.g. N_2 and CO, have the same m/z-ratio, 28, and cannot be distinguished. To get around this problem one can analyze additional masses corresponding to fragments of the original molecule, also known as cracking patterns. In the above example, CO could separate into C an O during ionization, resulting in m/z ratios 12 and 16 also being present in the mass spectrum, which is not the case for N_2. Additionally, multiple ionization events can occur, generating ions with higher charge that in turn will be detected as lower mass species. Another approach is to study an alternative isotype of a species with an alternative mass. To summarize, the user of a mass spectrometer must take care to ensure that the correct species is measured.

5 Nanoreactor Chip for Single Particle Catalysis

Designing, fabricating and characterizing a novel type of nanofluidic chip has been a major part of this thesis. The main goal of this device was to (i) enable mass transport to and from individual nanoparticles, (ii) provide optical access to the inside of the channels to enable single particle dark field scattering spectroscopy and imaging, (iii) provide temperature control up to 400 °C and (iv) be connected to a QMS for residual gas analysis of reaction products created inside the nanofluidic system. In this chapter, I will first introduce nanofluidics followed by a detailed explanation of the working principle of the nanoreactor and the surrounding hardware.

5.1 Nanofluidics

Nanofluidics can be described as the field related to fluidic behavior on scales below 100 nm. Typically, this involves creating structures that confine a fluid (liquid, gas, or a mix of the two) where at least one dimension is < 100 nm. However, sometimes the definition stretches into the μm-regime in what is called "extended nanofludics",[219,220] which allows for a wider range of nanometric objects to be studied, e.g. single cells or macromolecules, such as DNA. Although different fields have studied nanoscale flow for a long time, the name nanofluidics is rather recent, as it emerged in the early 2000's in the footsteps of microfluidics.[29] The transition from micro- to nanofluidics can be partially attributed to the improvements in the field of nanotechnology that allow for more precise characterization, as well as better control of smaller structures.

Because nanoscale phenomena related to flow are inherent to many fields, nanofluidics is naturally interdisciplinary. To illustrate this, **Figure 5.1** presents disciplines that incorporate knowledge about nanofluidics in some way, together with some relevant applications.[29] Although nanofluidics can be considered as an evolution of microfluidics, it is important to note that the distinction between the two stretches far beyond the difference in size. When scaled down to < 100 nm, new phenomena start to emerge, which opens up possibilities not only to study smaller samples, but also to investigate new scientific territories. Due to the extreme confinement, the physical behavior of fluids in nanofluidic structures can differ significantly compared to the bulk case. This can be explained by the characteristic length scales of the fluid, such as the hydrodynamic radius, the Debye length and the electronic double layer being on the same scale as the confining structures. To this end, a selection of phenomena that have been observed and investigated with the help of nanofluidics are nonlinear transport resulting in concentration polarization,[221,222] ion-current rectification[223,224] and changes in the properties of

liquids.[225–227] A multitude of additional studies of the properties of liquids confined at the nanoscale exist, and I refer the interested reader to one of many review articles on the topic.[219,220,228–230] Of more direct relevance for the work presented in this thesis is another aspect of nanofluidics, namely the possibility to enable precise mass transport down to the level of individual (macro) molecules that can be delivered to specific sites to be investigated or detected. This precise control has been applied in nanoparticle/molecular sieves[231,232] as well as to reshape molecules as demonstrated by e.g. stretching of DNA to measure the length of a DNA molecule[233] or for DNA mapping.[234]

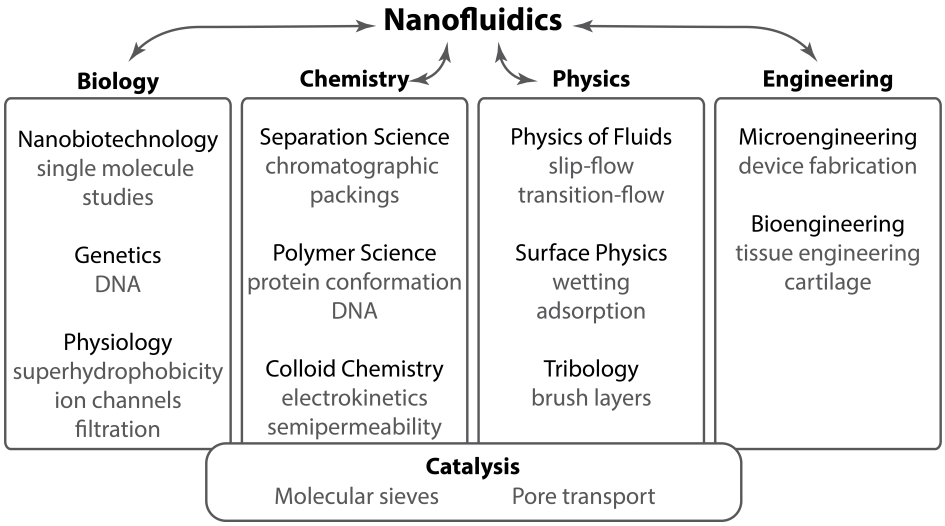

Figure 5.1 Research disciplines related to nanofluidics within a number of relevant subjects. (Adapted from [29]).

One important technological aspect of nanofluidics that is essential to the applications presented in this work is the ability to decorate the *inside* of the nanofluidic system with functional nanostructures, as exemplified in **Figure 5.2**. The emerging capabilities to do so have been proposed as the key to bring nanofluidics from the more fundamental physics oriented stage to a more application oriented regime.[219] Nevertheless, due to the small dimensions, selective functionalization of nanofluidic systems is a major challenge. For example, since one of the main approaches to fabricating nanofluidic systems is to use lithography-based nanofabrication techniques[235] where the nanofluidic structures are etched into a substrate and sealed by a lid that is chemically bonded to the substrate, any functionalization inside the channels that requires nanoscale precision has to be done *prior to* the bonding. Furthermore, the positioning of a nanoscale object inside another nanoscale structure is by itself non-trivial and requires very careful alignment. Hence, to the best of my knowledge, prior to my own contribution to this field presented in this thesis, there existed only one successful example, for the functionalization of the inside of a nanofluidic system with nanoparticles.[236] The

authors demonstrated a method to place nanoparticles, as well as seal the chip, using a room temperature bonding process. Furthermore, they used the patterned structures for molecular functionalization within nanochannels. In contrast, I am mainly interested in the optical readout capabilities of functionalizing nanofluidic systems with nanostructures to shed light on nanoparticle changes taking place on individual particles during catalysis, and I am using a nanofluidic system to confine a gas rather than a liquid.

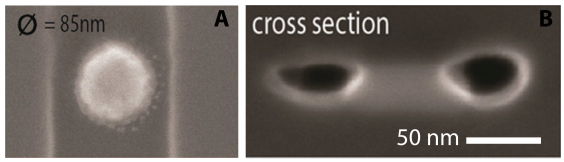

Figure 5.2 Functionalized nanochannel. SEM micrographs of two different Au nanoparticles placed inside nanochannels. A) Top view of a particle in a channel. Particle diameter is indicated. B) Cross sectional view of a 30 nm deep and ~150 nm wide nanochannel with a particle in the center. The particle has the same height as the channel, resulting in two separate channels on each side of the particle.

In a catalysis context, nanofluidic systems occur in the porous structure of catalyst support materials. These pores are categorized into three subgroups,[237] (i) micropores with pore diameters of < 2 nm, (ii) mesopores with diameters between 2 – 50 nm and (iii) macropores (> 50 nm) which are all present in many types of catalysts. In a porous material, the gas flow can be modified if molecules are more likely to interact with the walls of the fluidic structure than with other molecules. This can be quantified by comparing the pore width (d) and the mean free path (l) of a molecule that can be described by kinetic theory of gases as

$$l = \frac{\mu}{P}\sqrt{\frac{\pi k_B T}{2m}} \tag{5.1}$$

where μ is the viscosity, k_B is Boltzmann constant, P is pressure and m is the molecular mass. From the mean free path and the pore width, the so-called Knudsen number can be calculated as

$$\mathrm{Kn} = \frac{l}{d} \tag{5.2}$$

The Knudsen number can then be used to estimate to what degree molecular interactions and molecule-wall interactions will govern the flow. Specifically, for large, open systems (Kn < 0.01) molecule-molecule interactions dominate and the flow can be described by continuum models, whereas highly spatially confined systems (Kn > 10) are described by free molecular flow models.[238] In between these two extremes the flow is further classified as slip flow (0.01 < Kn < 0.1) or transition flow (0.1 < Kn < 10). As an example, the mean free path of Nitrogen (μ = 18.5 μPs) at P = 1 bar and T = 25 °C is ca. 60 nm. This can be compared with the typical channel

dimension in my work of ca. 100 nm, leading to Kn = 0.6, which is in the transition flow regime. Furthermore, in my applications, the temperature is commonly higher (up to 400°C) and the pressure varies from a few bars to below 1 mbar, which leads to significantly higher values of *Kn*. Pressure and flow profiles have therefore been predicted using a unified flow model that can be applied in a wide range of Knudsen numbers.[239]

5.2 Gas Phase Nanoreactor Platform

With the aim to enable operando characterization of individual catalyst nanoparticles, we designed and built an integrated gas-phase nanoreactor system connected to a QMS (**Figure 5.3**). In this system, the nanofluidic chip (**Figure 5.3B-C**) at its core enables controlled gas phase mass transport to and from individual and optically accessible catalytic nanoparticles, while simultaneously monitoring reaction products exiting the reactor using the QMS. To accomplish this, the Si/SiO_2 based nanofluidic chip is connected to a customized macroscopic ambient pressure gas flow control system based on off-the-shelf Swagelok components on the inlet side. On the outlet side, it is connected to an ultra-high vacuum (UHV) chamber equipped with a high-end QMS (Hiden HAL/3F PIC). For this purpose, a customized sample holder was designed (**Figure 5.3B**) and is discussed in detail below. This sample holder is then mounted on the motorized stage of an upright optical microscope (Nikon Eclipse LV150) to enable optical microscopy and spectroscopy of the catalyst nanoparticles inside the nanochannels. Image collection is done by a spectrometer (Andor 193i) equipped with an electron multiplying charge-coupled device (EMCCD) camera (Andor iXon Ultra 888). This arrangement enables the simultaneous monitoring of the catalyst (surface) state at the single nanoparticle level and to correlate it with reaction product formation to derive structure-function correlations. The following sub sections are intended to serve as a comprehensive guide to the components of the nanoreactor.

5.2.1 Nanoreactor Chip Holder and Gas Supply

To connect the nanoreactor chip to the macroscopic world, we designed and manufactured a chip holder, which enables (i) mounting of the chip on the stage of an upright optical microscope to facilitate optical spectroscopy and imaging, (ii) controlled supply of gas at up to 10 bar pressure on the inlet side and (iii) the effusion of the reaction products from the nanoreactor into an UHV chamber equipped with the QMS. 3D drawings of the chip holder with and without a mounted chip are presented in **Figure 5.3B** & **Figure 5.4A**, respectively.

The chip holder is machined from stainless steel and equipped with Swagelok VCR connections. Furthermore, electrical connection to the chip for heating and temperature readout is enabled by six gold plated electronic spring pins embedded in a machinable ceramic block (**B in Figure 5.4A**). To minimize air leaks, perfluoro elastomer (FPM) O-rings are placed at the interface between the fluidic chip and the sample holder in micromachined grooves that are surrounded by an Ar flow system

to continuously flush the O-rings with inert Ar gas from the purging inlet in **Figure 5.4A**. The gas inlet connections of the holder connect to an array of four mass flow controllers (MFCs – Bronkhorst) that are used to determine the gas mix entering the chip on one side, and a pressure controller on the opposite side to control the pressure of the gases at the inlet of the nanoreactor chip. Using this arrangement and by varying the flow rate set at the MFCs used, the time to fully exchange the microfluidic system at the inlet side from one gas composition to another can be controlled. A typical flow of 10 ml/min results in a time for gas change of < 1 minute, with the gas exchange in the macroscopic gas lines connecting the MFCs with the chip holder as the main determining factor.

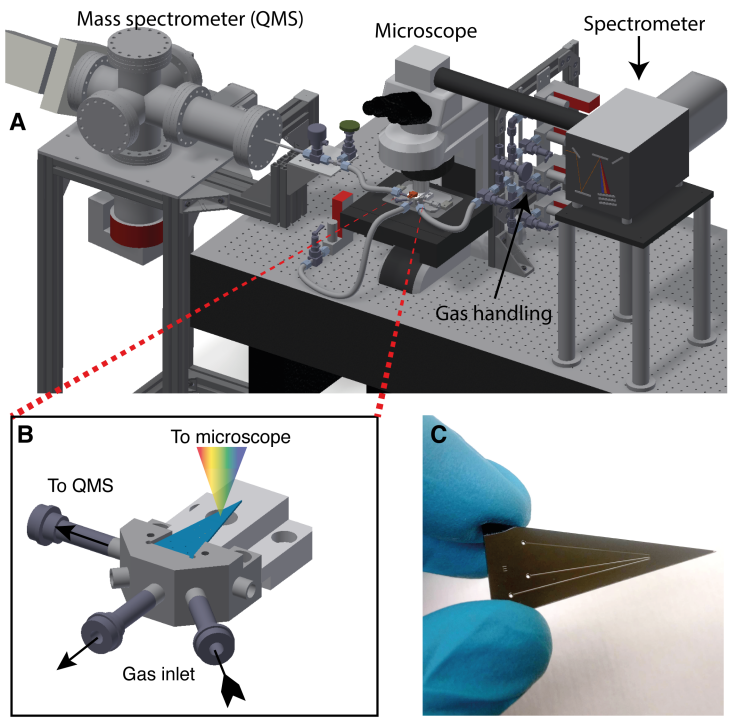

Figure 5.3 The Nanoreactor setup. A) Schematic depiction of the complete nanoreactor instrument. The nanofluidic chip is mounted in the tailor-made chip holder that connects it to the gas managing system, as well as to the QMS. The chip holder is mounted on the motorized stage of an upright microscope equipped with a dark-field objective and coupled to a spectrometer equipped with an imaging EMCCD camera shown to the right. B) Zoom-in of the nanoreactor chip holder that connects the chip (blue) to the gas supply, as well as the QMS. The chip is mounted such that the tip, where the nanofluidic structures are located, is accessible by the optical microscope for DFSS analysis of individual catalyst nanoparticles placed inside. C) Photo of a nanoreactor chip where the microfluidic channels and the inlet holes are seen.

The outlet of the chip holder is directly connected to the UHV chamber, hosting the QMS, via stainless steel tubing. To enable movement of the chip under the microscope, flexible tubing (Swagelok) is used, which also serves to minimize vibrations translated from pumps to the microscope stage. The gas lines, as well as the vacuum chamber hosting the QMS, can be heated to enable bakeout of the whole vacuum system. To minimize background signal and maximize the sensitivity, the base pressure of the QMS chamber is 10^{-10} mbar. Upon operation of the nanoreactor, it rises to approximately 5×10^{-9} mbar, depending on the chip design that determines the total flow rate into the QMS. The residual gas detection in the chamber is performed with a triple filter quadrupole mass spectrometer equipped with a pulsed ion counting detector (Hiden HAL/3F PIC) and a gold-plated ion source.

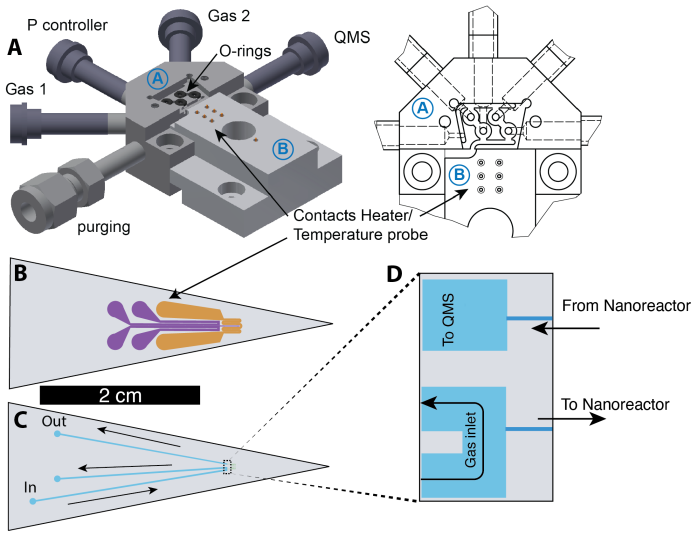

Figure 5.4 Chip holder and microfluidic channels. A) 3D (left) and 2D (right) depictions of the chip holder, illustrating the 5 gas ports available for gas handling and the 6 electric contacts used to set and measure the temperature of the nanoreactor. Circled **A** and **B** in the figures indicate parts that are fabricated in stainless steel and ceramics, respectively. B) Backside of the nanoreactor chip revealing the Pt heater (yellow) and thermometer (purple) that connects to the pins shown in (A). C) Schematic depiction of the nanofluidic chip with the microfluidic system shown in light blue. The arrows show the direction of the gas flow both on the inlet (high pressure) side and on the outlet side (low pressure towards QMS) channels where the inlets (marked In and Out) connect to the chip holder at the O-rings indicated in (A). D) Zoom in of the microfluidic channels where they connect to the nanoreactor through nanofluidic channels.

The nanoreactor chip itself is held in place on the chip holder by a stainless-steel block clamping it from above. On top of this block, a water-cooled copper heat exchanger is installed to actively cool the part of the chip that is mounted in the holder to minimize the heating of the chip holder upon operation of the on-chip heater, described in detail below. This is important since heating of the chip-holder

increases the leaking through the O-rings and thus has a negative impact on the performance of the system.

5.2.2 Microfluidic System

The microfluidic gas supply system on the inlet side of the chip is designed in a U-turn fashion (**Figure 5.4C-D**). Gases enter the chip through the bottom connector marked "In", flow in the direction indicated by the arrows and exit through the outlet hole, where an on-line pressure controller is used to set the upstream pressure. The cross-sectional dimensions of the microchannels are chosen such that they enable gas flow rates on the order of 1-10 ml/min, without significant pressure drop. This yields dimensions on the order of 200 μm width and 50 μm depth, or larger. This microfluidic inlet system connects to the nanochannels at the tip of the U-turn, which means that the pressure set in the microchannel determines the inlet pressure in the nanoreactor, which in turn determines the flowrate through the nanofluidic system. On the outlet side of the chip, the nanochannels connect to a second microfluidic system with the same dimensions (upper channel of **C**), which is directly connected to the UHV system with the QMS. Hence, *all* gases that have passed through the nanoreactor are collected here for residual gas analysis.

5.2.3 Nanofluidic System

The nanochannels are the core of the nanoreactor because they contain the catalyst bed. They are designed to enable the accurate control of the reactant flow to the nanoparticles. Specifically, the dimensions of the nanofluidic channels determine the flow rate and thus the number of reactant molecules supplied to the catalyst bed. Hence, the nanochannels can be tuned to either yield a higher flow by making them wide and short or a lower flow by making them long and/or narrow. This also makes it possible to tune the residence time of reactants over the catalyst bed. At the same time, since all gas exiting the nanochannels is directly fed into the UHV chamber with the QMS, the flow rate and thus the dimensions of the nanochannels, also determine the base pressure in the vacuum chamber which, to ensure optimal operation of the QMS, is ideally kept below 10^{-7} mbar.

Some examples of nanoreactor designs used in this work are presented in **Figure 5.5**. In all designs, the depth of the nanochannels are 100 nm, while the in-plane dimensions are varied. The first design (**Figure 5.5A**) is intended to create a long residence time in the reaction zone to ensure well mixed conditions, in analogy with a continuously stirred tank reactor (CSTR). In contrast, the second channel type (**Figure 5.5B**) results in the formation of significant concentration gradients along the catalyst bed due to reactant conversion. These two designs were used in **Paper V**. The last design (**Figure 5.5C**) consists of six parallel nanochannels, designed as symmetric funnels narrowing down to a central channel with a width of 400 nm. This design was intended to mimic a porous catalyst and was used to visualize how reactant gradients inside the pores directly affected the transient state of the individual catalyst particles placed inside (**Papers IV & VII**).

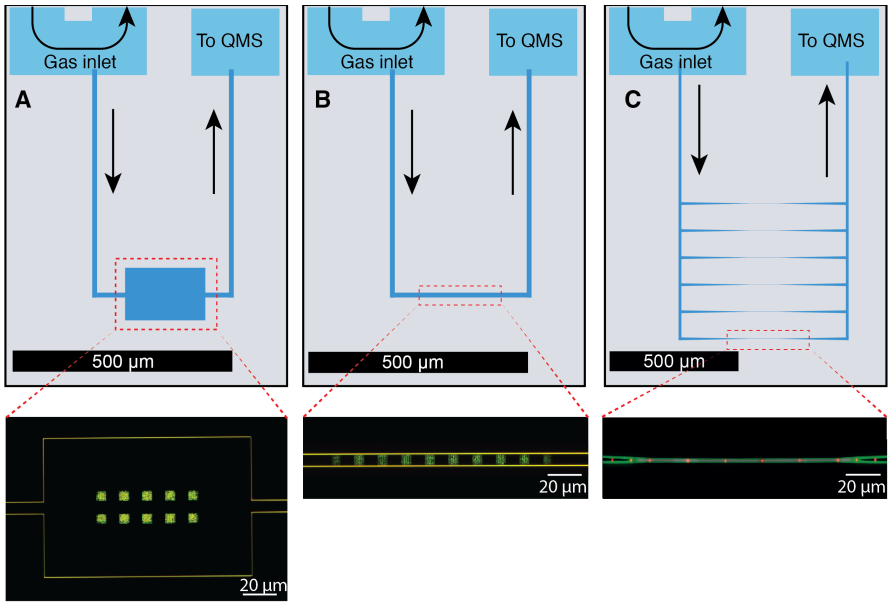

Figure 5.5 Nanofluidic channel designs. Top row shows three example nanoreactor designs and the bottom row depicts colored optical microscopy images of the reactors containing catalyst nanoparticles. In (A) and (B) the nanoparticles are arranged in square arrays, each containing 100 particles. In (C) the red dots correspond to individual Cu nanoparticles (enhanced color).

5.2.4 Monitoring Individual Nanoparticles in Nanochannels

Optical access to the chip is achieved by placing it under an upright optical microscope equipped with a 50× EPI-illumination dark-field objective. Connected to the microscope is an imaging spectrometer (Andor 193i) equipped with an EMCCD (Andor iXon Ultra 888) that enables both imaging and spectroscopy of the particles placed under the microscope. To minimize the risk of the chip drifting out of the field of view during experiments that can span over several days, a motorized stage (Märzhäuser Wetzlar SCAN) with a built-in feedback loop is used.

In the nanofluidic channels, the nanoparticles can be seen as bright spots together with light scattered from the surrounding channel walls (**Figure 5.6A**). To minimize background signal and to be able to isolate the optical response of the particles, the scattering from the walls is eliminated by installing an aperture in the illumination light path, as illustrated in the inset of **Figure 5.6B**. In this way, by blocking incident light perpendicular to the channels flow direction, scattering from the channel walls can be efficiently suppressed (**Figure 5.6B**). The individual scattering spectra of the nanoparticles can then be resolved by means of imaging or DFSS, as described in chapter 4.

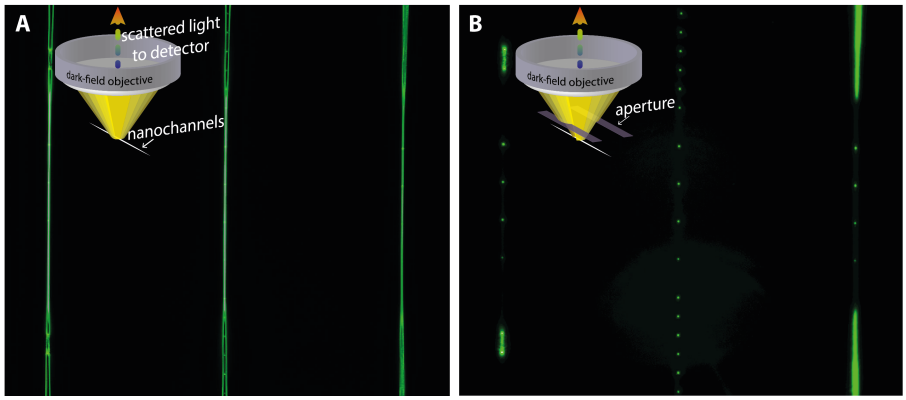

Figure 5.6 Dark field microscopy of particles in nanochannels. A) Dark field image of 3 nanochannels containing nanoparticles. B) Same as A) but with an aperture inserted to block light incident perpendicularly to the nanochannels, effectively eliminating scattering from channel walls and making the individual nanoparticles visible.

5.2.5 Nanoreactor Characterization

Flow Through the Nanochannels

The driving force for flow through the nanochannels is the pressure difference (ΔP) between the inlet and outlet. During experiments performed in the nanoreactor, the inlet side is typically held at constant pressure (at or above ambient pressure), while the outlet is pumped to a pressure below 0.001 mbar, i.e. $P_{in} \gg P_{out}$. The pressure difference between the two sides, $\Delta P = P_{in} - P_{out}$, can thus be simplified to a $\Delta P = P_{in}$.

Flow measurements were performed by establishing a known pressure of pure Ar on the inlet side of the nanochannels (P_{in}) and connecting the outlet to a closed volume that is evacuated at the start of the experiment (**Figure 5.7A**). By monitoring the pressure in the closed volume over time (**Figure 5.7B**) the ideal gas law can be utilized to translate the change in pressure to a molecular flow as:

$$\dot{N} = \frac{V}{k_B T}\frac{dP}{dt} \tag{5.1}$$

where $\dot{N}$ is the molecular flow entering the volume, $V = 4.95\times10^{-5}$ m^3 is the known volume, k_B is the Boltzmann constant, T is the temperature of the chamber and $\frac{dP}{dt}$ is the change in pressure over time which corresponds to the slope of the lines in **Figure 5.7B**. The extracted molecular flow rate through a nanoreactor (**Figure 5.5C**) is presented for three pressures in **Figure 5.7C**.

As discussed previously, some unwanted leaking of gases from the interface between the chip and the holder is unavoidable. This leak rate can be quantified from the data presented in **Figure 5.7C** as the flow rate at 0 bar inlet pressure, giving a leak rate of

approximately 10^{11} molecules/s. By flushing the interface with Ar, introduction of unwanted gases can be avoided.

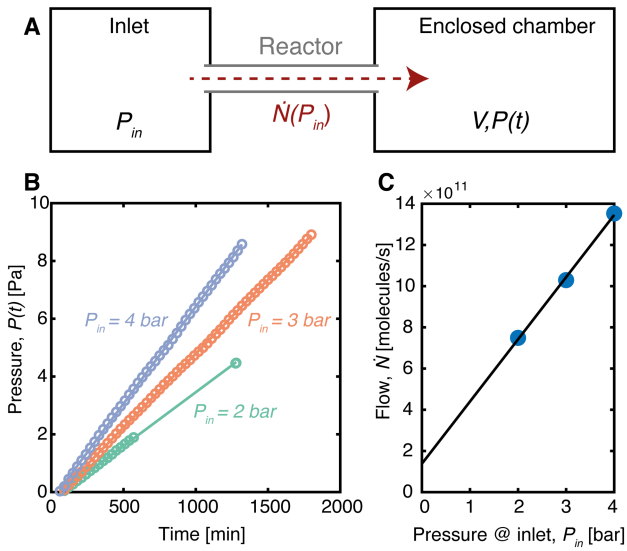

Figure 5.7 Flow measurement. A) Schematic representation of the flow measurement where the nanoreactor (center) is connected to a high-pressure side (inlet) and a low-pressure side with a closed volume that is gradually filled by the flow through the reactor ($\dot{N}$), resulting in a gradually increasing pressure *P(t)*. B) Pressure in the closed volume vs time for three different applied inlet pressures. C) The calculated molecular flow rates as a function of inlet pressure.

Pressure Profile in Nanoreactor

An important factor to consider when designing the nanoreactor system was the pressure profile inside the channels. However, due to the small scale, getting direct pressure measurements inside the channels is not possible with conventional pressure sensors. To nevertheless obtain this information, a combination of a numerical flow model and a nanoparticle-based pressure measurement was used. In **Figure 5.8** a nanoreactor design is presented (**A,B**) with its corresponding simulated pressure profile (**D**), obtained using a rarefied gas flow model valid for the whole Knudsen number regime.[239] As expected, the model predicts a continuous pressure drop along the channel with a dramatic decrease at the narrow part of the channel. Near the center of the nanochannel, where the catalyst bed is typically placed, the pressure is approximately 50% of the pressure applied in the inlet microchannel.

To experimentally address the pressure inside the nanochannel it is possible to make use of nanoparticle-based hydrogen sensors placed throughout the channel. The specific sensor is based on Pd that is known to undergo a first order phase transition when it absorbs hydrogen, and this transition is observable by monitoring the LSPR response of the particle.[26] The transition from a metallic phase (α-phase) to the hydride phase (β-phase) occurs at a relatively well defined hydrogen partial pressure

which, at the experimental conditions of 300 K, is in the range 25-35 mbar.[26] Therefore, if a particle is exposed to a partial H_2 pressure that exceeds this threshold, it will undergo a phase transition that can be observed in its optical fingerprint.

In a system with a spatially varying total gas pressure, the local H_2 partial pressure can be expressed as:

$$P_{H_2}(\boldsymbol{r}) = P(\boldsymbol{r}) \times C_{H_2} \tag{5.2}$$

where $P(\boldsymbol{r})$ is the position dependent total pressure in the channel and C_{H_2} is the concentration of H_2 gas in the stream. Thus, by finding the lowest H_2 concentration that results in a clear phase transition, the local pressure can be calculated as

$$P(\boldsymbol{r}) = \frac{P^*_{H_2}}{C^*_{H_2}} \tag{5.3}$$

where $P^*_{H_2}$ is the partial H_2 pressure required for hydride phase transition and $C^*_{H_2}$ is the measured threshold H_2 concentration below which, no hydride phase transition is observed.

Based on this, a pressure measurement was conducted by placing a row of individual Au-Pd hybrid nanoparticles (same structure as **Figure 3.7** with Pd as the top material) along the channel, as illustrated in **Figure 5.8B** by the individually colored dots. The scattering spectrum of the nanoparticles was then monitored under varying H_2 concentrations, where a significant shift in the FWHM of the spectrum can be measured as a result of the phase transition.

The results presented in **Figure 5.8C** show such an experiment, using an inlet pressure of 2 bar, where they gray bars indicate pulses of hydrogen with different concentrations. Looking at the single particle response, most particles undergo a phase transition for 3.5 % and 4 % H_2, except the bottom two. The absence of a phase transition can be explained by the partial pressure of H_2 never reaching above the required threshold pressure in the lower end of the channel. This is in good agreement with the estimated pressure drop based on the model simulations that predict a H_2 partial pressure below 25 mbar (at a H_2 concentration of 4 %) in the last 15 μm of the narrow channel, where the two particles are located. As the H_2 concentration is decreased further, most particles along the wider part of the channel respond down to a H_2 concentration of 1.5 %, with some variation due to particle-particle differences.[26] As a general trend, particles placed further downstream require a higher H_2 concentration to induce phase transition, which is especially clear when turning to the particles placed in the narrow part of the channel. By assuming a threshold pressure of 25 mbar, and putting the extracted threshold H_2 concentrations into eq. 5.3, the experimentally found total pressure inside the channel can be extracted (**Figure 5.8D**).

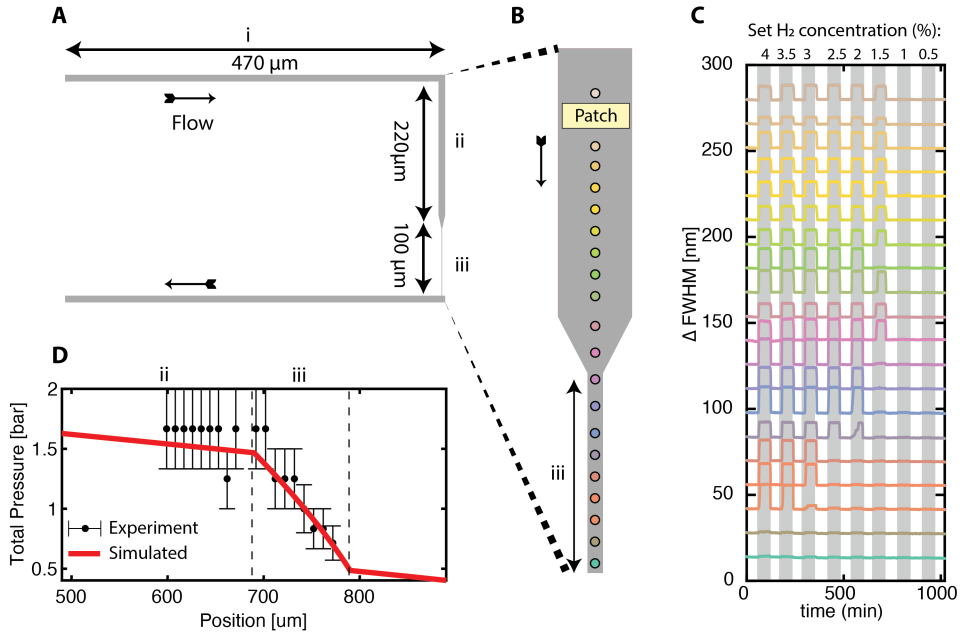

Figure 5.8 Nanoreactor pressure profile. A) Nanochannel design used for the simulation and experiment. The depth of the channels is 100 nm and the width is 10 µm at the wider parts (i,ii) down to 900 nm in the narrow region (iii). B) Schematic of the straight part of the nanochannel containing nanoparticles indicated by colored dots. The area marked as "Patch" corresponds to a region with 70 densely packed nanoparticles (not optically measured). C) Optical response presented as a change in FWHM of the dark field scattering spectra of 20 individual nanoparticles when exposed to pulses of hydrogen of different concentration indicated at the top of the figure. The individual responses have been shifted vertically for clarity and the absolute value given for the FWHM is arbitrary. D) Simulated relative pressure profile along the channel (red line) and experimentally found total pressure (black dots with error bars). Regions marked by roman letters are the same as in (A & B). The errors bars are based on an uncertainty of 5 mbar in the threshold H_2 pressure required for a phase transition in the Pd particles.

5.2.6 On-chip Heater

To enable precise temperature control of the reaction volume of the chip (i.e. the nanochannel region), an on-chip resistive heater and four-point probe thermometer is microfabricated on the backside of the nanoreactor chip. The heater design is presented in **Figure 5.4B**, where the yellow part corresponds to the heater and the purple part to the thermometer. We chose Pt as the material for the device due to its stability and reliable resistance-to-temperature relationship that is close to linear in a wide temperature range.[240]

The specific heater design, in terms of geometry, was adapted to ensure that the heating is focused to an area corresponding to the nanochannel part of the reactor

chip. To verify this, COMSOL simulations were performed to investigate the heat distribution on the chip. In the simulations, the dimensions and material composition of the chip and heater was set to match the real design and the water-cooled chip holder was simulated by fixed temperature boundary conditions at all interfaces that were in contact with the holder. **Figure 5.9** illustrates the simulated heat profiles at a reactor temperature of ca 400°C, confirming that the heating was focused on an area close to the nanoreactor region (**Figure 5.9A**) and that the temperature difference between the back of the chip (where the heater and thermometer are placed) and the nanoreactor region is < 2 °C (**Figure 5.9B-C**).

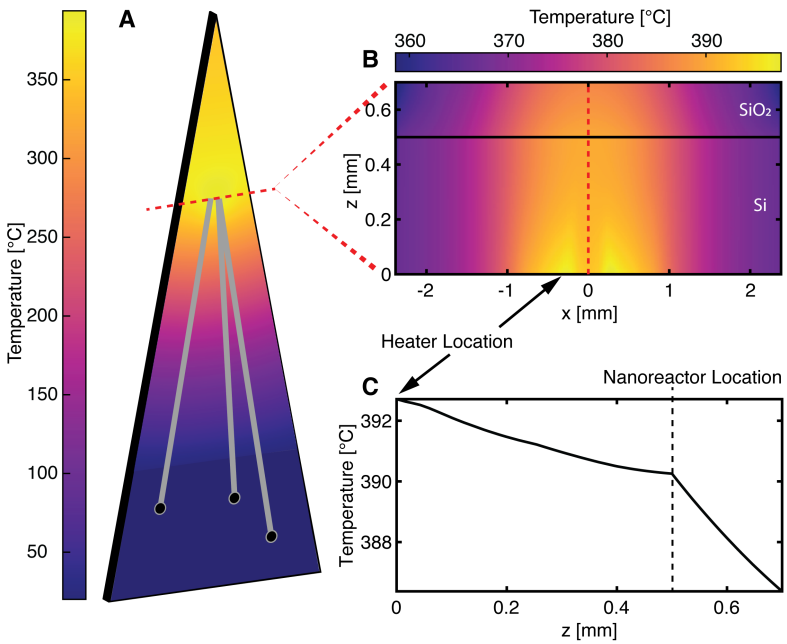

Figure 5.9 Temperature profiles of heated chip. A) 2D temperature distribution in the plane of the chip. The red dashed line corresponds to the position of the cross section presented in (B). B) 2D cross section through the chip. The black line corresponds to the Si-SiO2 interface where the nanochannels are located. The vertical red dashed line corresponds to the center of the chip and the temperature along this line is presented in (C). Note the different color scales is used in (A) and (B). C) Temperature profile through the chip. The heater is located at z = 0 mm and the nanoreactor is located at z = 0.5 mm.

Heater Calibration and Performance

The heater is controlled by driving a current through the Pt film using an external power supply. Temperature readout is achieved in a four point probe fashion[240] by monitoring the resistance of the Pt film, which changes in a well-defined way as a function of temperature.[241] To calibrate the temperature-resistance relationship for

our device it was immersed in an mineral oil bath heated to a series of temperatures, while simultaneously logging the resistance of the sensor. The data was then fitted to a Callendar-Van Dusen polynomial with the form[242]:

$$R(T) = R_0(1 + \alpha T + \beta T^2) \quad (5.4)$$

Were R_0 is the resistance at 0°C, α and β are the coefficients and T is the temperature in °C. The obtained data and corresponding fit based on equation 5.2 are presented in **Figure 5.10** and yielded $R_0 = 150\ \Omega, \alpha = 0.0021\ \mathrm{K}^{-1}$ and $\beta = -6.5 \cdot 10^{-7}\ \mathrm{K}^{-2}$.

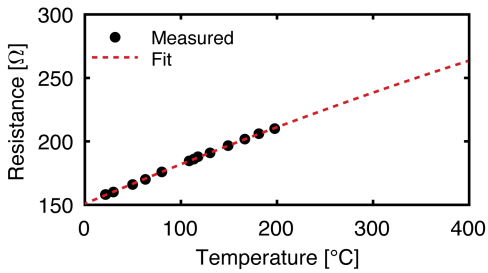

Figure 5.10 Calibration curve for the on-chip heater. Black circles correspond to the measured resistance at a given temperature and the red line to the fitted function based on eq. 5.2, used to extrapolate the response at higher temperatures.

The heater, as well as the four-point probe thermometer, are connected to a temperature control unit (Lakeshore 335) that acts as a proportional–integral–derivative (PID) regulator that can set and maintain a given temperature with an error of < 0.1 °C. With the current design, a working temperature range of 20 – 400°C can be achieved and the response time when changing temperature of the chip is typically < 1 s. Due to the small size of the chip, even a very large temperature change from room temperature to 400 °C takes less than 10 s when increasing the temperature. Cooling is done passively, and a change from 400 °C down to 30 ° takes approximately 20 s. This makes it possible to perform fast temperature ramps and measure the response of the catalyst.

However, changing the temperature affects the gas density in the channels and therefore the total flow. Therefore, gas flow corrections must be considered when experiments are performed during temperature ramps. Another difficulty when working with temperature ramps stems from thermal expansion of the nanoreactor chip, which results in particles moving out of the field of view of the microscope. This can in principle be mediated by utilizing an optical feedback loop that continuously re-centers the image. However, I have not yet explored such schemes.

6 Summary and Outlook

At this point, I hope this thesis has convinced you that a comprehensive understanding of heterogeneous catalysts requires studies on several length scales and at relevant conditions. I present an approach to catalyst characterization based on nanofluidics and plasmonic nanospectroscopy that is capable of operando characterization of individual nanoparticles. The development of the optical method and the nanoreactor platform is presented in the appended papers.

The nanoreactor concept presented in this thesis was enabled by the development of nanofabrication methods that made it possible to place well defined, optically addressable, single catalyst particles inside nanofluidic channels. In **Paper I,** which is the first work on this topic, we place individual metallic nanoparticles inside nanofluidic channels by means of electron beam lithography and show that sequential bonding of a glass lid can establish a hermetic seal. The optical readout from individual metal nanoparticles is made possible by dark field scattering spectroscopy (DFSS). In this way, by monitoring the optical response of individual plasmonic Au nanoparticles inside nanochannels immersed in a liquid, we were able to resolve the dynamics of fluid exchange inside the nanochannels, as well as the binding kinetics of thiol molecules on a single Au nanoparticle.

A method to study the oxidation of Cu nanoparticles using their plasmonic response was investigated in **Papers II** & **III**. In these papers, we showed how experiments can be paired with FDTD simulations to extract oxidation kinetics and details related to the oxidation mechanism in individual particles. Specifically, in **Paper II,** indirect plasmonic sensing using Au-Cu heterodimer structures was used to probe small (~30 nm) Cu nanoparticles. In **Paper III,** DFSS was used to study individual Cu nanoparticles. These studies revealed how the apparent oxidation kinetics of Cu nanoparticles change over the course of oxidation, most likely due to dramatic structural changes. Furthermore, based on single particle measurements, where DFSS and TEM was combined, we showed how specific structural changes in the particles could be related to characteristic optical responses. This study also dramatically illustrated how differently each particle can respond to the same external conditions. In a wider context, the ability to combine detailed FDTD simulations with the experimental observations set the stage for many of the applications of plasmonic nanospectroscopy and imaging in my subsequent works.

The knowledge gained from these two developments was utilized when designing the nanoreactor platform. This involved the construction of a new experimental platform and designing nanofluidic systems suitable for gas phase experiments, both described in **Chapter 5**. Conveniently, the same general fabrication scheme that was developed for **Paper I** could be used to make nanofluidic chips suitable for gas phase experiments. As a first application example, the nanoreactor was used to study the

oxidation state of Cu nanoparticles during CO oxidation (**Papers IV** & **V**). In these papers, the plasmonic signal from individual Cu nanoparticles inside different nanoreactors was used to probe the catalyst state under reaction conditions. Based on these studies, we were able to show that reactor geometry significantly affects the deactivation dynamics of a catalyst bed. More specifically, in **Paper IV** we investigate particles placed in a model pore and observe how reactant conversion of a single nanoparticle affect the state of particles placed downstream. In **Paper V** we constructed nanofluidic systems that resulted in both well-mixed and plug-flow like regimes (**Paper V**), where the whole catalyst bed experienced similar reaction conditions or severe reactant concentration gradients were present, respectively.

As a first conclusion, these studies confirmed the reported observation[16] that Cu nanoparticles can only be kept in a metallic state when the oxygen feed is highly mass transport limited. Furthermore, we were able to reduce the catalyst loading to 1000 particles with an estimated exposed surface area of ca. 20 μm^2. This made it possible to perform operando spectroscopy and QMS reaction product analysis of the whole catalyst bed while retaining single particle resolution. With this ability, we were able to directly compare 1000 individual particle responses to the average catalyst bed response in the same experiment. In this way, we could directly observe how nominally identical catalyst particles, placed in close vicinity, behaved differently during a catalytic reaction. From a theoretical viewpoint, it is not surprising that particles behave differently since they are expected to have slight variations in surface (and bulk) structure. However, directly visualizing this fact on a whole catalyst bed, has, to my knowledge, not been done previously with single particle resolution. This is important, since operando methods that only resolve parts of the catalyst bed risk missing relevant information when drawing conclusions about the active state. By ensuring that all parts of the catalyst are studied, we minimize the risk that erroneous structure-function relationships are constructed. Our observations also indicate that a mixed phase catalyst bed could be quite common under reaction conditions. Possibly, this type of mixed phases plays a larger role in catalyst activity than typically assumed based on the current knowledge.

Single particle plasmonic nanospectroscopy is straightforward when the catalyst material also has "good" plasmonic properties (low losses and strong scattering), such as for Au, Ag and Cu. However, the method becomes more challenging for materials which are optically more lossy, as is the case for many widely used catalyst materials, for example Pt. To overcome this limitation, we utilize indirect plasmonic sensing to study Pt particles during CO oxidation in **Papers VI** & **VII**. As a first proof of principle, we demonstrated how DFSS of $Au/SiO_2/Pt$ hybrid nanostructures could be used to detect the surface state of Pt during CO oxidation in **Paper VI**. The same method was later used to study a larger number of particles inside a nanoreactor in the temperature range 180°C – 275°C, which is presented in **Paper VII**. By studying several (18) particles in parallel, we showed that CO poisoning of Pt was observed as a change in the (surface) state of all nanoparticles. More importantly, we identified clear particle differences, which we attribute to differences in the particles' surface structure. Based on extensive FDTD modelling, we also propose that the observed

optical response stemmed from both a change in the oxidation state of the Pt surface and a change in the supporting SiO_2 layer. Interestingly, as a general trend, the formation of a Pt-oxide was more pronounced at higher temperatures, which therefore supports the notion that a Pt-oxide could be present during CO oxidation at operando conditions.

Outlook

This thesis presents the development of a new platform for catalyst research and there are several possible ways to continue this work in the future.

Up until now, I have mainly performed a number of "proof of principle" experiments based on the CO oxidation reaction and a natural next step is to make use of the nanoreactor platform to study other reactions. To best utilize the capabilities of the nanoreactor, studies of good plasmonic metals are preferred. One industrially relevant reaction that comes to mind is ethylene epoxidation that is typically performed on a Ag catalyst.[243] Ag is an excellent plasmonic material and changes to its oxidation state is known to dramatically affect its optical response, similar to Cu that has been presented here. Furthermore, it would be interesting to investigate Cu nanoparticles in other industrially relevant reactions. Cu is, for example, used industrially in the water gas shift reaction (WGSR) and the importance of particle faceting and oxidation state has been highlighted recently.[244] Cu oxides have also been proposed as an interesting epoxidation catalyst.[245] In several reactions, Cu has been shown to be active at the interface between a (sub-) oxide and a metallic surface.[244–246] As the techniques I have developed can detect a slight surface oxidation it could therefore add insight to the mechanisms governing these reactions.

Besides studies of catalyst nanoparticles, the nanofluidic platform we have built might be of interest to study fluidics on the nanoscale. For example, the nanoscale pressure sensor concept, discussed in section 5.2.5 and **Paper IV**, could be used to perform pressure measurements with high spatial resolution inside extremely confined geometries. This could potentially be used to verify and improve existing fluid dynamic models.

It would also be interesting to try to further optimize the reactor geometry in ways that make detection of reaction products from even smaller sample sizes than the presented ca. 1000 particles possible. The limitation in catalyst loading stems from the ability to efficiently use mass spectrometry to detect the reactant product formed (or the decrease in reactant concentration). Currently, we have preliminary data indicating that measurements from 100 nanoparticles is possible, and scaling this down another order of magnitude is probably within reach. In this regime, where around 10 nanoparticles can be addressed, significant contributions from each particle can hopefully be extracted and direct correlations between a single nanoparticles structure and activity could be revealed. However, this estimate assumes particles in the 100 nm size range, which is still significantly larger than commercially used catalyst nanoparticles (< 5 nm). Therefore, a significant improvement to the approach developed in this thesis would be to make it possible

to study smaller catalytic particles. This evolution will impose two major challenges. First, the smaller particles will have a smaller exposed surface area, and thus have a lower total conversion, making activity measurements by mass spectrometry even more difficult. Secondly, the type of plasmonic nanospectroscopy used in this work, that relies on scattering from individual nanoparticles, is limited to particles that are larger than 50 nm. Therefore, to be able to do access smaller nanoparticles one could, for example, make use of better sensing arrangements based on tailored nanoplasmonic structures with strong field enhancements[27] onto which the catalyst particle can be attached. For example, the heterodimer structures utilized in **Paper II** made studies of ca 30 nm disk shape Cu nanoparticles possible.

To enable investigations of more realistic catalyst beds, it would be interesting to increase the number of particles that can be monitored even further. Additionally, by varying the relative placement of particles in the catalyst bed, inter particle communications via e.g. reactant and temperature gradients could be investigated further. Therefore, studies that expand the concept presented in **Paper V** could be used to explore how catalyst beds can be optimized on the micrometer scale. Currently, the maximum number of particles that can be studied with the method presented in this thesis is limited by the field of view of the microscope. Scaling this to 10 000 particles should therefore be possible without modification. This method could be further improved by adding ability to collect spectroscopic information from all particles in the image. This could be achieved by utilizing a tunable band-pass filter between the microscope and the camera to achieve multi/hyper spectral imaging.

Although my studies have almost exclusively[†] been performed in the gas phase, a colleague has simultaneously developed the methodology to study liquid phase catalytic reactions inside nanochannels.[91] In these studies, fluorescent reactants are used to measure catalyst activity over individual Au nanoparticles of different size. However, the state of the catalyst during the reaction is not monitored. An interesting development would be to combine the fluorescence approach with plasmonic nanospectroscopy to simultaneously probe activity and the state of individual particles. Succeeding with such a study would make single particle structure-function relationships possible and would thus be a significant milestone in the field of single particle catalysis.

Furthermore, one major limitation of the current nanoreactor is that it is not possible to access the catalyst particles placed inside the chips with high-resolution imaging techniques, such as TEM. This problem stems from the (relatively) thick SiO_2 and Si layers used in the chip. In this context, it would be a huge improvement to design the nanoreactor chip in a way that made it accessible to e.g. an electron beam. This would open the possibility to do in- or ex-situ SEM/TEM analysis of the particles to get

[†] **Paper I** involved liquid phase experiments.

information about particle morphology at the different stages of the reaction. One way of achieving this could be to include an etched, electron transparent window on the chip, similar to the in situ TEM chips that exist already.[56] With this added ability it would be possible to identify unique structural properties of the individual particles which could be related to differences in catalytic performance.

So far, we have only addressed nanoparticles made by evaporation-based techniques. These particles are well defined when it comes to size and shape in 2D but evaporation techniques lack control over crystallinity and 3D structure of the particles. It would therefore be interesting to incorporate chemically synthesized colloidal nanoparticles into the nanoreactors for catalyst testing. Placement of individual nanoparticles from colloidal solutions could be achieved by e.g. surface modification inside the channels or by using novel patterning[247] or printing techniques.[248]

I envision the optical method presented in this thesis as a tool for screening large arrays of particles and identifying interesting individuals or sub-groups. These subgroups could be investigated further by a high-resolution technique and hopefully enable more efficient identification of specific traits (active sites) that have a large impact on the catalyst's performance.

In this way, I hope that the method presented in this thesis can help us better understand the remaining secrets of real catalysts.

7 Acknowledgements

I acknowledge financial support from the ERC StG SINCAT and the Knut and Alice Wallenberg Foundation project 2015.0055, and thank the Knut and Alice Wallenberg Foundation for their support of the infrastructure in the MC2 nanofabrication laboratory at Chalmers.

There are also a lot of people that have met over these past years and although I cannot mention everyone, here are some people I want to acknowledge.

First of all, a big thanks to Christoph, my main supervisor who gave me the opportunity to join this jorney. Your never ending optimism and commitment that things will work out has helped me a lot!

My examiner, Henrik Grönbeck, thanks for good scientific discussions, feedback on my thesis, and for keeping Chemical Physics a good workplace.

Thanks also to my co-supervisor Hanna Härelind.

Thanks to Stephan Bartling who was a big part of starting this project and building the nanoreactor infrastructure.

Thanks to Joachim for teaching me almost everything I know about nanofabrication. I look forward to hearing more of your fascinating ideas in the future!

Thanks to all past and present members of the Langhammer group.

A special thanks to Ferry, my office mate for most of my time at Chalmers. Your commitment and ability to get things done is truly impressive and I'm happy we got to co-author a paper before you left.

Thanks to Sara and Christopher for successful collaborations and nice conference trips including both biking in big cities and skiing on big mountains.

Thanks to all co-authors. In particular Henrik, Astrid, Su, Svetlana, Vladimir, Joachim, Sara, Christopher, Tomasz and Anders. You were all part of making this work possible.

I'm also grateful to everyone at Chemical Physics, it's really nice to always have friends around for lunches and fika.

A big thanks to my friends and family who makes my life outside of work great!

Finally, thanks to Matilda for all your support these years and for making each day the best!

Bibliography

1. Barber, D. J. & Frestone, I. C. An Investigation of the origin of the colour of the Lycurgus cup by analytical transmission electron microscopy. *Archaeometry* **32**, 33–45 (1990) doi:10.1111/j.1475-4754.1990.tb01079.x.
2. Eigler, D. M. & Schweizer, E. K. Positioning single atoms with a scanning tunnelling microscope. *Nature* **344**, 524–526 (1990) doi:10.1038/344524a0.
3. Dyck, O., Kim, S., Kalinin, S. V. & Jesse, S. Placing single atoms in graphene with a scanning transmission electron microscope. *Appl. Phys. Lett.* **111**, 113104 (2017) doi:10.1063/1.4998599.
4. Lu, W. & Lieber, C. M. Nanoelectronics from the bottom up. *Nat. Mater.* **6**, 841–850 (2007) doi:10.1038/nmat2028.
5. Bell, A. T. The impact of nanoscience on heterogeneous catalysis. *Science* **299**, 1688–91 (2003) doi:10.1126/science.1083671.
6. Agasti, S. S. *et al.* Nanoparticles for detection and diagnosis. *Adv. Drug Deliv. Rev.* **62**, 316–328 (2010) doi:10.1016/J.ADDR.2009.11.004.
7. Chorkendorff, I. & Niemantsverdriet, J. W. *Concepts of modern catalysis and kinetics*. (Wiley-VCH, 2017).
8. Ertl, G. Reactions at Surfaces: From Atoms to Complexity (Nobel Lecture). *Angew. Chemie Int. Ed.* **47**, 3524–3535 (2008) doi:10.1002/anie.200800480.
9. Unger, K. K. *Characterization of porous solids : proceedings of the IUPAC symposium (COPS I), Bad Soden a. Ts., F.R.G., April 26-29, 1987*. (Elsevier, 1988).
10. Frenken, J. & Groot, I. *Operando Research in Heterogeneous Catalysis*. vol. 114 (Springer International Publishing, 2017). doi:10.1007/978-3-319-44439-0.
11. Duke, C. B. The birth and evolution of surface science: Child of the union of science and technology. *Proc. Natl. Acad. Sci.* **100**, 3858 LP – 3864 (2003) doi:10.1073/pnas.0730358100.
12. Rodríguez, J. A. *et al. In-situ Characterization of Heterogeneous Catalysts*. (John Wiley & Sons, Inc., 2013). doi:10.1002/9781118355923.
13. Kim, B. H. *et al.* Critical differences in 3D atomic structure of individual ligand-protected nanocrystals in solution. *Science* **368**, 60–67 (2020) doi:10.1126/science.aax3233.
14. Sambur, J. B. & Chen, P. Approaches to Single-Nanoparticle Catalysis. *Annu. Rev. Phys. Chem.* **65**, 395–422 (2014) doi:10.1146/annurev-physchem-040513-103729.
15. Ackermann, M. D. *et al.* Structure and Reactivity of Surface Oxides on Pt(110) during Catalytic CO Oxidation. *Phys. Rev. Lett.* **95**, 255505 (2005) doi:10.1103/PhysRevLett.95.255505.
16. Bu, Y., Niemantsverdriet, J. W. H. & Fredriksson, H. O. A. Cu Model Catalyst Dynamics and CO Oxidation Kinetics Studied by Simultaneous in Situ UV-Vis and Mass Spectroscopy. *ACS Catal.* **6**, 2867–2876 (2016) doi:10.1021/acscatal.5b02861.
17. Gänzler, A. M. *et al.* Operando spatially and time-resolved X-ray absorption spectroscopy and infrared thermography during oscillatory CO oxidation. *J. Catal.* **328**, 216–224 (2015) doi:10.1016/J.JCAT.2015.01.002.
18. Hejral, U., Müller, P., Balmes, O., Pontoni, D. & Stierle, A. Tracking the shape-

dependent sintering of platinum–rhodium model catalysts under operando conditions. *Nat. Commun.* **7**, 10964 (2016) doi:10.1038/ncomms10964.

19. Zafeiratos, S., Piccinin, S. & Teschner, D. Alloys in catalysis: phase separation and surface segregation phenomena in response to the reactive environment. *Catal. Sci. Technol.* **2**, 1787–1801 (2012) doi:10.1039/C2CY00487A.
20. Larsson, E. M., Langhammer, C., Zoric, I. & Kasemo, B. Nanoplasmonic Probes of Catalytic Reactions. *Science* **326**, 1091–1094 (2009) doi:10.1126/science.1176593.
21. Alekseeva, S., Nedrygailov, I. I. & Langhammer, C. Single Particle Plasmonics for Materials Science and Single Particle Catalysis. *ACS Photonics* **6**, 1319–1330 (2019) doi:10.1021/acsphotonics.9b00339.
22. Larsson, E. M., Syrenova, S., Langhammer, C. & Giessen, H. Nanoplasmonic sensing for nanomaterials science. *Nanophotonics* vol. 1 249–266 (2012) doi:10.1515/nanoph-2012-0029.
23. Taylor, A. B. & Zijlstra, P. Single-Molecule Plasmon Sensing: Current Status and Future Prospects. *ACS Sensors* **2**, 1103–1122 (2017) doi:10.1021/acssensors.7b00382.
24. Anker, J. N. *et al.* Biosensing with plasmonic nanosensors. *Nat. Mater.* **7**, 442–453 (2008) doi:10.1038/nmat2162.
25. Syrenova, S. *et al.* Hydride formation thermodynamics and hysteresis in individual Pd nanocrystals with different size and shape. *Nat. Mater.* **14**, 1236–1244 (2015) doi:10.1038/nmat4409\rhttp://www.nature.com/nmat/journal/v14/n12/abs/nmat4409.html#supplementary-information.
26. Alekseeva, S. *et al.* Grain boundary mediated hydriding phase transformations in individual polycrystalline metal nanoparticles. *Nat. Commun.* **8**, 1084 (2017) doi:10.1038/s41467-017-00879-9.
27. Liu, N., Tang, M. L., Hentschel, M., Giessen, H. & Alivisatos, A. P. Nanoantenna-enhanced gas sensing in a single tailored nanofocus. *Nat. Mater.* **10**, 631–636 (2011) doi:10.1038/nmat3029.
28. Bocquet, L. & Charlaix, E. Nanofluidics, from bulk to interfaces. *Chem. Soc. Rev.* **39**, 1073–1095 (2010) doi:10.1039/B909366B.
29. Eijkel, J. C. T. & Berg, A. van den. Nanofluidics: what is it and what can we expect from it? *Microfluid. Nanofluidics* **1**, 249–267 (2005) doi:10.1007/s10404-004-0012-9.
30. Berzelius, J. J. Årsberättelsen om framsteg i fysik och kemi. (1835).
31. Ostwald, W. Catalysis. *Phys. Zeitschrift* **3**, 313–322 (1901).
32. Appl, M. & Wiley InterScience (Online service). *Ammonia : principles and industrial practice*. (Wiley-VCH, 1999).
33. Haber, F. & Koenig, A. Wissenschaftliche Übersichten: Oxydation des Luftstickstoffes. *Zeitschrift für Elektrotechnik und Elektrochemie* **16**, 11–25 (1910) doi:10.1002/bbpc.19100160105.
34. Haber, F. & Rossignol, R. Le. Über die technische Darstellung von Ammoniak aus den Elementen. *Zeitschrift für Elektrochemie und Angew. Phys. Chemie* **19**, 53–72 (1913) doi:10.1002/BBPC.19130190201.
35. Schlögl, R. Heterogeneous catalysis. *Angew. Chemie - Int. Ed.* **54**, 3465–3520 (2015) doi:10.1002/anie.201410738.
36. Papp, C. From Flat Surfaces to Nanoparticles: In Situ Studies of the Reactivity of Model Catalysts. *Catal. Letters* **147**, 2–19 (2017) doi:10.1007/s10562-016-1925-0.

37. Taylor, H. S. & Armstrong, E. F. A theory of the catalytic surface. *Proc. R. Soc. London. Ser. A, Contain. Pap. a Math. Phys. Character* **108**, 105–111 (1925) doi:10.1098/rspa.1925.0061.

38. Taylor, H. S. Fourth Report of the Committee on Contact Catalysis. *J. Phys. Chem.* **30**, 145–171 (1926) doi:10.1021/j150260a001.

39. Kohn, W. & Sham, L. J. Self-Consistent Equations Including Exchange and Correlation Effects. *Phys. Rev.* **140**, A1133–A1138 (1965) doi:10.1103/PhysRev.140.A1133.

40. Jones, R. O. Density functional theory: Its origins, rise to prominence, and future. *Rev. Mod. Phys.* **87**, 897–923 (2015) doi:10.1103/RevModPhys.87.897.

41. Jørgensen, M. & Grönbeck, H. Scaling Relations and Kinetic Monte Carlo Simulations To Bridge the Materials Gap in Heterogeneous Catalysis. *ACS Catal.* **7**, 5054–5061 (2017) doi:10.1021/acscatal.7b01194.

42. Jinnouchi, R. & Asahi, R. Predicting Catalytic Activity of Nanoparticles by a DFT-Aided Machine-Learning Algorithm. *J. Phys. Chem. Lett.* **8**, 4279–4283 (2017) doi:10.1021/acs.jpclett.7b02010.

43. Squires, G. Francis Aston and the mass spectrograph. *J. Chem. Soc.{,} Dalt. Trans.* 3893–3900 (1998) doi:10.1039/A804629H.

44. Somorjai, G. . The surface science of heterogeneous catalysis. *Surf. Sci.* **299–300**, 849–866 (1994) doi:10.1016/0039-6028(94)90702-1.

45. Ertl, G. Oscillatory Kinetics and Spatio-Temporal Self-Organization in Reactions at Solid Surfaces. *Science* **254**, 1750–1755 (1991) doi:10.1126/science.254.5039.1750.

46. Binnig, G. & Rohrer, H. Scanning Tunneling Microscopy—from Birth to Adolescence (Nobel Lecture). *Angew. Chemie Int. Ed. English* **26**, 606–614 (1987) doi:10.1002/anie.198706061.

47. Wintterlin, J., Völkening, S., Janssens, T. V. W., Zambelli, T. & Ertl, G. Atomic and Macroscopic Reaction Rates of a Surface-Catalyzed Reaction. *Science* **278**, 1931 LP – 1934 (1997) doi:10.1126/science.278.5345.1931.

48. Quate, C. F. The AFM as a tool for surface imaging. *Surf. Sci.* **299–300**, 980–995 (1994) doi:https://doi.org/10.1016/0039-6028(94)90711-0.

49. Stoltze, P. & Nørskov, J. K. Bridging the "pressure gap" between ultrahigh-vacuum surface physics and high-pressure catalysis. *Phys. Rev. Lett.* **55**, 2502–2505 (1985) doi:10.1103/PhysRevLett.55.2502.

50. Gustafson, J. *et al.* The Role of Oxides in Catalytic CO Oxidation over Rhodium and Palladium. *ACS Catal.* **8**, 4438–4445 (2018) doi:10.1021/acscatal.8b00498.

51. Somorjai, G. A. & McCrea, K. R. B. T.-A. in C. Sum frequency generation: Surface vibrational spectroscopy studies of catalytic reactions on metal single-crystal surfaces. in *Impact of Surface Science on Catalysis* vol. 45 385–438 (Academic Press, 2000). doi:https://doi.org/10.1016/S0360-0564(02)45018-3.

52. van Spronsen, M. A., van Baarle, G. J. C., Herbschleb, C. T., Frenken, J. W. M. & Groot, I. M. N. High-pressure operando STM studies giving insight in CO oxidation and NO reduction over Pt(1 1 0). *Catal. Today* **244**, 85–95 (2015) doi:10.1016/J.CATTOD.2014.07.008.

53. Herbschleb, C. T. *et al.* The ReactorSTM: Atomically resolved scanning tunneling microscopy under high-pressure, high-temperature catalytic reaction conditions. *Rev. Sci. Instrum.* **85**, 083703 (2014) doi:10.1063/1.4891811.

54. Roobol, S. B. *et al.* The ReactorAFM : Non-contact atomic force microscope operating under high-pressure and high-temperature catalytic conditions. *Rev. Sci. Instrum.* **86**, 033706 (2015) doi:10.1063/1.4916194.

55. Knudsen, J., Andersen, J. N. & Schnadt, J. A versatile instrument for ambient pressure x-ray photoelectron spectroscopy: The Lund cell approach. *Surf. Sci.* **646**, 160–169 (2016) doi:10.1016/J.SUSC.2015.10.038.

56. Vendelbo, S. B. *et al.* Visualization of oscillatory behaviour of Pt nanoparticles catalysing CO oxidation. *Nat. Mater.* **13**, 884–890 (2014) doi:10.1038/nmat4033.

57. Kooyman, P. J. Development of Operando transmission electron microscopy. in *Springer Series in Chemical Physics* vol. 114 111–129 (2017). doi:10.1007/978-3-319-44439-0_5.

58. Conner, W. C. & Falconer, J. L. Spillover in Heterogeneous Catalysis. *Chem. Rev.* **95**, 759–788 (1995) doi:10.1021/cr00035a014.

59. Karim, W. *et al.* Catalyst support effects on hydrogen spillover. *Nature* **541**, 68–71 (2017) doi:10.1038/nature20782.

60. Collins, S. S. E., Cittadini, M., Pecharromán, C., Martucci, A. & Mulvaney, P. Hydrogen Spillover between Single Gold Nanorods and Metal Oxide Supports: A Surface Plasmon Spectroscopy Study. *ACS Nano* **9**, 7846–7856 (2015) doi:10.1021/acsnano.5b02970.

61. Eriksson, M. & Petersson, L.-G. Spillover of hydrogen, oxygen and carbon monoxide in oxidation reactions on SiO2 supported Pd. *Surf. Sci.* **311**, 139–152 (1994) doi:10.1016/0039-6028(94)90485-5.

62. Olsson, L., Persson, H., Fridell, E., Skoglundh, M. & Andersson, B. A Kinetic Study of NO Oxidation and NOx Storage on Pt/Al2O3 and Pt/BaO/Al2O3. *J. Phys. Chem. B* **105**, 6895–6906 (2001) doi:10.1021/jp010324p.

63. van Schrojenstein Lantman, E. M., Deckert-Gaudig, T., Mank, A. J. G., Deckert, V. & Weckhuysen, B. M. Catalytic processes monitored at the nanoscale with tip-enhanced Raman spectroscopy. *Nat. Nanotechnol.* **7**, 583–586 (2012) doi:10.1038/nnano.2012.131.

64. de Smit, E. *et al.* Nanoscale chemical imaging of a working catalyst by scanning transmission X-ray microscopy. *Nature* **456**, 222–225 (2008) doi:10.1038/nature07516.

65. Chakrabarti, A. *et al.* A decade+ of operando spectroscopy studies. *Catal. Today* **283**, 27–53 (2017) doi:10.1016/j.cattod.2016.12.012.

66. Weckhuysen, B. M. Snapshots of a working catalyst: possibilities and limitations of in situ spectroscopy in the field of heterogeneous catalysis. *Chem. Commun.* 97–110 (2002) doi:10.1039/B107686H.

67. van Spronsen, M. A., Frenken, J. W. M. & Groot, I. M. N. Surface science under reaction conditions: CO oxidation on Pt and Pd model catalysts. *Chem. Soc. Rev.* **46**, 4347–4374 (2017) doi:10.1039/C7CS00045F.

68. Portela, R., Perez-Ferreras, S., Serrano-Lotina, A. & Bañares, M. A. Engineering operando methodology: Understanding catalysis in time and space. *Front. Chem. Sci. Eng.* **12**, 509–536 (2018) doi:10.1007/s11705-018-1740-9.

69. Roy, K., Artiglia, L. & van Bokhoven, J. A. Ambient Pressure Photoelectron Spectroscopy: Opportunities in Catalysis from Solids to Liquids and Introducing Time Resolution. *ChemCatChem* **10**, 666–682 (2018) doi:10.1002/cctc.201701522.

70. Roiaz, M., Pramhaas, V., Li, X., Rameshan, C. & Rupprechter, G. Atmospheric pressure reaction cell for operando sum frequency generation spectroscopy of ultrahigh vacuum

grown model catalysts. *Rev. Sci. Instrum.* **89**, 45104 (2018) doi:10.1063/1.5021641.

71. Plodinec, M., Nerl, H. C., Girgsdies, F., Schlögl, R. & Lunkenbein, T. Insights into Chemical Dynamics and Their Impact on the Reactivity of Pt Nanoparticles during CO Oxidation by Operando TEM. *ACS Catal.* **10**, 3183–3193 (2020) doi:10.1021/acscatal.9b03692.

72. Chee, S. W., Arce-Ramos, J. M., Li, W., Genest, A. & Mirsaidov, U. Structural changes in noble metal nanoparticles during CO oxidation and their impact on catalyst activity. *Nat. Commun.* **11**, 2133 (2020) doi:10.1038/s41467-020-16027-9.

73. Singh, J., Nachtegaal, M., Alayon, E. M. C., Stötzel, J. & van Bokhoven, J. A. Dynamic Structure Changes of a Heterogeneous Catalyst within a Reactor: Oscillations in CO Oxidation over a Supported Platinum Catalyst. *ChemCatChem* **2**, 653–657 (2010) doi:10.1002/cctc.201000061.

74. Newton, M., Newton & A., M. Time Resolved Operando X-ray Techniques in Catalysis, a Case Study: CO Oxidation by O2 over Pt Surfaces and Alumina Supported Pt Catalysts. *Catalysts* **7**, 58 (2017) doi:10.3390/catal7020058.

75. Grunwaldt, J.-D., Hannemann, S., Schroer, C. G. & Baiker, A. 2D-Mapping of the Catalyst Structure Inside a Catalytic Microreactor at Work: Partial Oxidation of Methane over Rh/Al2O3. *J. Phys. Chem. B* **110**, 8674–8680 (2006) doi:10.1021/jp060371n.

76. Thomas, S. *et al.* Modelling a reactor cell for operando IR studies: From qualitative to fully quantitative kinetic investigations. *Catal. Today* **283**, 176–184 (2017) doi:https://doi.org/10.1016/j.cattod.2016.07.008.

77. Meunier, F. C. The design and testing of kinetically-appropriate operando spectroscopic cells for investigating heterogeneous catalytic reactions. *Chem. Soc. Rev.* **39**, 4602–4614 (2010) doi:10.1039/B919705M.

78. Mesu, J. G., Beale, A. M., de Groot, F. M. F. & Weckhuysen, B. M. Probing the Influence of X-rays on Aqueous Copper Solutions Using Time-Resolved in Situ Combined Video/X-ray Absorption Near-Edge/Ultraviolet–Visible Spectroscopy. *J. Phys. Chem. B* **110**, 17671–17677 (2006) doi:10.1021/jp062618m.

79. Martis, V. *et al.* Effects of X-rays on Crystal Nucleation in Lithium Disilicate. *Cryst. Growth Des.* **11**, 2858–2865 (2011) doi:10.1021/cg200004y.

80. Jiang, P. *et al.* Room-Temperature Reaction of Oxygen with Gold: An In situ Ambient-Pressure X-ray Photoelectron Spectroscopy Investigation. *J. Am. Chem. Soc.* **132**, 2858–2859 (2010) doi:10.1021/ja909987j.

81. Morgan, K. *et al.* Evolution and Enabling Capabilities of Spatially Resolved Techniques for the Characterization of Heterogeneously Catalyzed Reactions. *ACS Catal.* **6**, 1356–1381 (2016) doi:10.1021/acscatal.5b02602.

82. Grunwaldt, J.-D., Wagner, J. B. & Dunin-Borkowski, R. E. Imaging Catalysts at Work: A Hierarchical Approach from the Macro- to the Meso- and Nano-scale. *ChemCatChem* **5**, 62–80 (2013) doi:10.1002/cctc.201200356.

83. Buurmans, I. L. C. & Weckhuysen, B. M. Heterogeneities of individual catalyst particles in space and time as monitored by spectroscopy. *Nat. Chem.* **4**, 873–886 (2012) doi:10.1038/nchem.1478.

84. Grunwaldt, J.-D. *et al.* Catalysts at work: From integral to spatially resolved X-ray absorption spectroscopy. *Catal. Today* **145**, 267–278 (2009) doi:10.1016/J.CATTOD.2008.11.002.

85. Roy, K. *et al.* Design and performance of a new setup for spatially resolved transmission X-ray photoelectron spectroscopy at the Swiss Light Source. *J. Synchrotron Radiat.* **26**, 785–792 (2019) doi:10.1107/S1600577519002984.

86. Hartman, T., Geitenbeek, R. G., Wondergem, C. S., van der Stam, W. & Weckhuysen, B. M. Operando Nanoscale Sensors in Catalysis: All Eyes on Catalyst Particles. *ACS Nano* **14**, 3725–3735 (2020) doi:10.1021/acsnano.9b09834.

87. Kimmerle, B. *et al.* Visualizing a Catalyst at Work during the Ignition of the Catalytic Partial Oxidation of Methane. *J. Phys. Chem. C* **113**, 3037–3040 (2009) doi:10.1021/jp810319v.

88. Koptyug, I. V, Khomichev, A. V, Lysova, A. A. & Sagdeev, R. Z. Spatially Resolved NMR Thermometry of an Operating Fixed-Bed Catalytic Reactor. *J. Am. Chem. Soc.* **130**, 10452–10453 (2008) doi:10.1021/ja802075m.

89. van Ravenhorst, I. K. *et al.* In Situ Local Temperature Mapping in Microscopy Nano-Reactors with Luminescence Thermometry. *ChemCatChem* **11**, 5505–5512 (2019) doi:10.1002/cctc.201900985.

90. Zetterberg, J. *et al.* An in situ set up for the detection of CO2 from catalytic CO oxidation by using planar laser-induced fluorescence. *Rev. Sci. Instrum.* **83**, 53104 (2012) doi:10.1063/1.4711130.

91. Levin, S. *et al.* A nanofluidic device for parallel single nanoparticle catalysis in solution. *Nat. Commun.* **10**, 4426 (2019) doi:10.1038/s41467-019-12458-1.

92. Xu, W., Zhang, Y. & Chen, T. X-ray-Based Microscopy of Single Particle Nanocatalysis. in *Single Particle Nanocatalysis* 181–206 (Wiley-VCH Verlag GmbH & Co. KGaA, 2019). doi:10.1002/9783527809721.ch7.

93. Kumar, N., Stephanidis, B., Zenobi, R., Wain, A. J. & Roy, D. Nanoscale mapping of catalytic activity using tip-enhanced Raman spectroscopy. *Nanoscale* **7**, 7133–7137 (2015) doi:10.1039/C4NR07441F.

94. Kumar, N., Weckhuysen, B. M., Wain, A. J. & Pollard, A. J. Nanoscale chemical imaging using tip-enhanced Raman spectroscopy. *Nat. Protoc.* **14**, 1169–1193 (2019) doi:10.1038/s41596-019-0132-z.

95. Neubrech, F., Huck, C., Weber, K., Pucci, A. & Giessen, H. Surface-enhanced infrared spectroscopy using resonant nanoantennas. *Chem. Rev.* **117**, 5110–5145 (2017) doi:10.1021/acs.chemrev.6b00743.

96. Wu, C.-Y. *et al.* High-spatial-resolution mapping of catalytic reactions on single particles. *Nature* **541**, 511–515 (2017) doi:10.1038/nature20795.

97. Meier, J., Friedrich, K. A. & Stimming, U. Novel method for the investigation of single nanoparticle reactivity. *Faraday Discuss.* **121**, 365–372 (2002) doi:10.1039/B200014H.

98. Novo, C., Funston, A. M. & Mulvaney, P. Direct observation of chemical reactions on single gold nanocrystals using surface plasmon spectroscopy. *Nat. Nanotechnol.* **3**, 598–602 (2008) doi:10.1038/nnano.2008.246.

99. Langhammer, C. & Larsson, E. M. Nanoplasmonic In Situ Spectroscopy for Catalysis Applications. *ACS Catal.* **2**, 2036–2045 (2012) doi:10.1021/cs300423a.

100. Renken, A. & Kiwi-Minsker, L. Microstructured Catalytic Reactors. *Adv. Catal.* **53**, 47–122 (2010) doi:10.1016/S0360-0564(10)53002-5.

101. Tanimu, A., Jaenicke, S. & Alhooshani, K. Heterogeneous catalysis in continuous flow microreactors: A review of methods and applications. *Chem. Eng. J.* **327**, 792–821 (2017)

doi:10.1016/J.CEJ.2017.06.161.

102. Yue, J., Schouten, J. C. & Nijhuis, T. A. Integration of Microreactors with Spectroscopic Detection for Online Reaction Monitoring and Catalyst Characterization. *Ind. Eng. Chem. Res.* **51**, 14583–14609 (2012) doi:10.1021/ie301258j.

103. Rizkin, B. A., Popovic, F. G. & Hartman, R. L. Review Article: Spectroscopic microreactors for heterogeneous catalysis. *J. Vac. Sci. Technol. A* **37**, 50801 (2019) doi:10.1116/1.5108901.

104. Kiwi-Minsker, L. & Renken, A. Microstructured reactors for catalytic reactions. *Catal. Today* **110**, 2–14 (2005) doi:10.1016/J.CATTOD.2005.09.011.

105. Rebrov, E. V. Heterogeneous Catalysis in Microreactors. in *Microreactors in Preparative Chemistry* 243–271 (Wiley-VCH Verlag GmbH & Co. KGaA, 2013). doi:10.1002/9783527652891.ch10.

106. Wiles, C. & Watts, P. Continuous process technology: a tool for sustainable production. *Green Chem.* **16**, 55–62 (2014) doi:10.1039/C3GC41797B.

107. Jähnisch, K., Hessel, V., Löwe, H. & Baerns, M. Chemistry in Microstructured Reactors. *Angew. Chemie Int. Ed.* **43**, 406–446 (2004) doi:10.1002/anie.200300577.

108. Henriksen, T. R., Olsen, J. L., Vesborg, P., Chorkendorff, I. & Hansen, O. Highly sensitive silicon microreactor for catalyst testing. *Rev. Sci. Instrum.* **80**, 124101 (2009) doi:10.1063/1.3270191.

109. Dionigi, F. *et al.* A transparent Pyrex μ-reactor for combined *in situ* optical characterization and photocatalytic reactivity measurements. *Rev. Sci. Instrum.* **84**, 103910 (2013) doi:10.1063/1.4826495.

110. Kehres, J. *et al.* Novel micro-reactor flow cell for investigation of model catalysts using *in situ* grazing-incidence X-ray scattering. *J. Synchrotron Radiat.* **23**, 455–463 (2016) doi:10.1107/S1600577516001387.

111. Baier, S., Rochet, A., Hofmann, G., Kraut, M. & Grunwaldt, J.-D. Lithographically fabricated silicon microreactor for in situ characterization of heterogeneous catalysts—Enabling correlative characterization techniques. *Rev. Sci. Instrum.* **86**, 065101 (2015) doi:10.1063/1.4921775.

112. Cao, E., Firth, S., McMillan, P. F. & Gavriilidis, A. Application of microfabricated reactors for operando Raman studies of catalytic oxidation of methanol to formaldehyde on silver. *Catal. Today* **126**, 119–126 (2007) doi:10.1016/J.CATTOD.2006.11.002.

113. Zhao, S. *et al.* Operando Characterization of Catalysts through use of a Portable Microreactor. *ChemCatChem* **7**, 3683–3691 (2015) doi:10.1002/cctc.201500688.

114. Beale, A. M., van der Eerden, A. M. J., Kervinen, K., Newton, M. A. & Weckhuysen, B. M. Adding a third dimension to operando spectroscopy: a combined UV-Vis, Raman and XAFS setup to study heterogeneous catalysts under working conditions. *Chem. Commun.* **0**, 3015 (2005) doi:10.1039/b504027b.

115. Tan, C. K. C., Delgass, W. N. & Baertsch, C. D. Spatially resolved in situ FTIR analysis of CO adsorption and reaction on Pt/SiO2 in a silicon microreactor. *Appl. Catal. B Environ.* **93**, 66–74 (2009) doi:10.1016/J.APCATB.2009.09.013.

116. Creemer, J. F. *et al.* Atomic-scale electron microscopy at ambient pressure. *Ultramicroscopy* **108**, 993–998 (2008) doi:10.1016/J.ULTRAMIC.2008.04.014.

117. Xin, H. L., Niu, K., Alsem, D. H. & Zheng, H. In Situ TEM Study of Catalytic

Nanoparticle Reactions in Atmospheric Pressure Gas Environment. *Microsc. Microanal.* **19**, 1558–1568 (2013) doi:10.1017/S1431927613013433.

118. Fam, Y. *et al.* A versatile nanoreactor for complementary in situ X-ray and electron microscopy studies in catalysis and materials science. *J. Synchrotron Radiat.* **26**, 1769–1781 (2019) doi:10.1107/S160057751900660X.

119. Ertl, G. Reactions at well-defined surfaces. *Surf. Sci.* **299–300**, 742–754 (1994) doi:10.1016/0039-6028(94)90694-7.

120. Allian, A. D. *et al.* Chemisorption of CO and Mechanism of CO Oxidation on Supported Platinum Nanoclusters. *J. Am. Chem. Soc.* **133**, 4498–4517 (2011) doi:10.1021/ja110073u.

121. Zhdanov, V. P. & Kasemo, B. Kinetic phase transitions in simple reactions on solid surfaces. *Surf. Sci. Rep.* **20**, 113–189 (1994) doi:10.1016/0167-5729(94)90009-4.

122. Zambelli, T., Barth, J. V., Wintterlin, J. & Ertl, G. Complex pathways in dissociative adsorption of oxygen on platinum. *Nature* **390**, 495–497 (1997) doi:10.1038/37329.

123. Burnett, D. J. *et al.* In-situ soft X-ray studies of CO oxidation on the Pt(1 1 1) surface. *Surf. Sci.* **564**, 29–37 (2004) doi:10.1016/J.SUSC.2004.07.001.

124. Imbihl, R. & Ertl, G. Oscillatory Kinetics in Heterogeneous Catalysis. *Chem. Rev.* **95**, 697–733 (1995) doi:10.1021/cr00035a012.

125. Vogel, D. *et al.* Local Catalytic Ignition during CO Oxidation on Low-Index Pt and Pd Surfaces: A Combined PEEM, MS, and DFT Study. *Angew. Chemie Int. Ed.* **51**, 10041–10044 (2012) doi:10.1002/anie.201204031.

126. Suchorski, Y. & Rupprechter, G. Local reaction kinetics by imaging. *Surf. Sci.* **643**, 52–58 (2016) doi:10.1016/j.susc.2015.05.021.

127. Jørgensen, M. & Grönbeck, H. The Site-Assembly Determines Catalytic Activity of Nanoparticles. *Angew. Chemie Int. Ed.* **57**, 5086–5089 (2018) doi:10.1002/anie.201802113.

128. Hendriksen, B. L. M. & Frenken, J. W. M. CO Oxidation on Pt(110): Scanning Tunneling Microscopy Inside a High-Pressure Flow Reactor. *Phys. Rev. Lett.* **89**, 046101 (2002) doi:10.1103/PhysRevLett.89.046101.

129. Beck, A. *et al.* The dynamics of overlayer formation on catalyst nanoparticles and strong metal-support interaction. *Nat. Commun.* **11**, 3220 (2020) doi:10.1038/s41467-020-17070-2.

130. Royer, S. & Duprez, D. Catalytic Oxidation of Carbon Monoxide over Transition Metal Oxides. *ChemCatChem* **3**, 24–65 (2011) doi:10.1002/cctc.201000378.

131. Eren, B., Heine, C., Bluhm, H., Somorjai, G. A. & Salmeron, M. Catalyst Chemical State during CO Oxidation Reaction on Cu(111) Studied with Ambient-Pressure X-ray Photoelectron Spectroscopy and Near Edge X-ray Adsorption Fine Structure Spectroscopy. *J. Am. Chem. Soc.* **137**, 11186–11190 (2015) doi:10.1021/jacs.5b07451.

132. Huang, T.-J. J. & Tsai, D.-H. H. CO Oxidation Behavior of Copper and Copper Oxides. *Catal. Letters* **87**, 173–178 (2003) doi:10.1023/A:1023495223738.

133. Xu, F. *et al.* Redox-Mediated Reconstruction of Copper during Carbon Monoxide Oxidation. *J. Phys. Chem. C* **118**, 15902–15909 (2014) doi:10.1021/jp5050496.

134. Jernigan, G. G. G. & Somorjai, G. A. a. Carbon Monoxide Oxidation over Three Different Oxidation States of Copper: Metallic Copper, Copper (I) Oxide, and Copper (II) Oxide - A Surface Science and Kinetic Study. *J. Catal.* **147**, 567–577 (1994) doi:10.1006/jcat.1994.1173.

135. Le, D., Stolbov, S. & Rahman, T. S. Reactivity of the Cu2O(100) surface: Insights from first principles calculations. *Surf. Sci.* **603**, 1637–1645 (2009) doi:https://doi.org/10.1016/j.susc.2008.12.039.

136. Luo, L. *et al.* Real-Time Atomic-Scale Visualization of Reversible Copper Surface Activation during the CO Oxidation Reaction. *Angew. Chemie Int. Ed.* **59**, 2505–2509 (2020) doi:10.1002/anie.201915024.

137. Zhdanov, V. P. & Kasemo, B. Simulation of kinetic oscillations in the CO+O2/Pt reaction on the nm scale. *J. Catal.* **214**, 121–129 (2003) doi:https://doi.org/10.1016/S0021-9517(02)00028-3.

138. Wu, L.-N., Tian, Z.-Y. & Qin, W. Mechanism of CO Oxidation on Cu2O (111) Surface: A DFT and Microkinetic Study. *Int. J. Chem. Kinet.* **50**, 507–514 (2018) doi:10.1002/kin.21176.

139. Museum, T. B. Lycurgus Cup. http://www.britishmuseum.org/research/collection_online/collection_object_details/collection_image_gallery.aspx?assetId=36154001&objectId=61219&partId=1#more-views.

140. Kelly, K. L., Coronado, E., Zhao, L. L. & Schatz, G. C. The optical properties of metal nanoparticles: The influence of size, shape, and dielectric environment. *J. Phys. Chem. B* **107**, 668–677 (2003) doi:10.1021/jp026731y.

141. Tittl, A., Giessen, H. & Liu, N. Plasmonic Gas and Chemical Sensing. in *Nanomaterials and Nanoarchitectures: A Complex Review of Current Hot Topics and their Applications* 239–272 (2015). doi:10.1007/978-94-017-9921-8_8.

142. Langhammer, C., Zorić, I., Kasemo, B. & Clemens, B. M. Hydrogen storage in Pd nanodisks characterized with a novel nanoplasmonic sensing scheme. *Nano Lett.* **7**, 3122–3127 (2007) doi:10.1021/nl071664a.

143. Mie, G. Beiträge zur Optik trüber Medien, speziell kolloidaler Metallösungen. *Ann. Phys.* **330**, 377–445 (1908) doi:10.1002/andp.19083300302.

144. Maier, S. A. *Plasmonics: Fundamentals and applications*. (Springer US, 2007). doi:10.1007/0-387-37825-1.

145. Schwind, M. *et al.* Nanoplasmonic Sensing for Monitoring the Initial Stages of Atmospheric Corrosion of Cu Nanodisks and Thin Films. *J. Electrochem. Soc.* **160**, C487–C492 (2013) doi:10.1149/2.051310jes.

146. Pirzadeh, Z., Pakizeh, T., Miljkovic, V., Langhammer, C. & Dmitriev, A. Plasmon–Interband Coupling in Nickel Nanoantennas. *ACS Photonics* **1**, 158–162 (2014) doi:10.1021/ph4000339.

147. Langhammer, C., Schwind, M., Kasemo, B. & Zorić, I. Localized Surface Plasmon Resonances in Aluminum Nanodisks. *Nano Lett.* **8**, 1461–1471 (2008) doi:10.1021/nl080453i.

148. Langhammer, C., Yuan, Z., Zorić, I. & Kasemo, B. Plasmonic Properties of Supported Pt and Pd Nanostructures. *Nano Lett.* **6**, 833–838 (2006) doi:10.1021/nl060219x.

149. Bansal, A. & Verma, S. S. Optical response of noble metal alloy nanostructures. *Phys. Lett. A* **379**, 163–169 (2015) doi:10.1016/j.physleta.2014.11.018.

150. Nugroho, F. A. A., Iandolo, B., Wagner, J. B. & Langhammer, C. Bottom-Up Nanofabrication of Supported Noble Metal Alloy Nanoparticle Arrays for Plasmonics. *ACS Nano* **10**, 2871–2879 (2016) doi:10.1021/acsnano.5b08057.

151. Lalisse, A., Tessier, G., Plain, J. & Baffou, G. Plasmonic efficiencies of nanoparticles made of metal nitrides (TiN, ZrN) compared with gold. *Sci. Rep.* **6**, 38647 (2016) doi:10.1038/srep38647.

152. Wokaun, A., Gordon, J. P. & Liao, P. F. Radiation Damping in Surface-Enhanced Raman Scattering. *Phys. Rev. Lett.* **48**, 957–960 (1982) doi:10.1103/PhysRevLett.48.957.

153. Zhao, J. *et al.* Methods for Describing the Electromagnetic Properties of Silver and Gold Nanoparticles. *Acc. Chem. Res.* **41**, 1710–1720 (2008) doi:10.1021/ar800028j.

154. Taflove, A., Hagness, S. C. & Piket-May, M. Computational Electromagnetics: The Finite-Difference Time-Domain Method. in *The Electrical Engineering Handbook* 629–670 (Elsevier, 2005). doi:10.1016/B978-012170960-0/50046-3.

155. García de Abajo, F. J. & Howie, A. Retarded field calculation of electron energy loss in inhomogeneous dielectrics. *Phys. Rev. B* **65**, 115418 (2002) doi:10.1103/PhysRevB.65.115418.

156. Rechberger, W. *et al.* Optical properties of two interacting gold nanoparticles. *Opt. Commun.* **220**, 137–141 (2003) doi:10.1016/S0030-4018(03)01357-9.

157. Sheikholeslami, S., Jun, Y. W., Jain, P. K. & Alivisatos, A. P. Coupling of optical resonances in a compositionally asymmetric plasmonic nanoparticle dimer. *Nano Lett.* **10**, 2655–2660 (2010) doi:10.1021/nl101380f.

158. Nordlander, P., Oubre, C., Prodan, E., Li, K. & Stockman, M. I. Plasmon hybridization in nanoparticle dimers. *Nano Lett.* **4**, 899–903 (2004) doi:10.1021/nl049681c.

159. Prodan, E., Radloff, C., Halas, N. J. & Nordlander, P. A hybridization model for the plasmon response of complex nanostructures. *Science* **302**, 419–22 (2003) doi:10.1126/science.1089171.

160. Flauraud, V. *et al.* Mode Coupling in Plasmonic Heterodimers Probed with Electron Energy Loss Spectroscopy. *ACS Nano* **11**, 3485–3495 (2017) doi:10.1021/acsnano.6b08589.

161. Zorić, I., Zäch, M., Kasemo, B. & Langhammer, C. Gold, Platinum, and Aluminum Nanodisk Plasmons: Material Independence, Subradiance, and Damping Mechanisms. *ACS Nano* **5**, 2535–2546 (2011) doi:10.1021/nn102166t.

162. Jensen, T. R., Malinsky, M. D., Haynes, C. L. & Van Duyne, R. P. Nanosphere Lithography: Tunable Localized Surface Plasmon Resonance Spectra of Silver Nanoparticles. *J. Phys. Chem. B* **104**, 10549–10556 (2000) doi:10.1021/jp002435e.

163. Traci R. Jensen *et al.* Nanosphere Lithography: Effect of the External Dielectric Medium on the Surface Plasmon Resonance Spectrum of a Periodic Array of Silver Nanoparticles. (1999) doi:10.1021/JP9926802.

164. Englebienne, P. Use of colloidal gold surface plasmon resonance peak shift to infer affinity constants from the interactions between protein antigens and antibodies specific for single or multiple epitopes. *Analyst* **123**, 1599–1603 (1998) doi:10.1039/a804010i.

165. Foerster, B., Rutten, J., Pham, H., Link, S. & Sönnichsen, C. Particle Plasmons as Dipole Antennas: State Representation of Relative Observables. *J. Phys. Chem. C* acs.jpcc.8b06350 (2018) doi:10.1021/acs.jpcc.8b06350.

166. Dahlin, A. B., Tegenfeldt, J. O. & Höök, F. Improving the instrumental resolution of sensors based on localized surface plasmon resonance. *Anal. Chem.* **78**, 4416–4423 (2006) doi:10.1021/ac0601967.

167. Jackman, J. A., Rahim Ferhan, A. & Cho, N. J. Nanoplasmonic sensors for biointerfacial science. *Chemical Society Reviews* vol. 46 3615–3660 (2017) doi:10.1039/c6cs00494f.

168. Haes, A. J., Zou, S., Schatz, G. C. & Van Duyne, R. P. Nanoscale optical biosensor: Short range distance dependence of the localized surface plasmon resonance of noble metal nanoparticles. *J. Phys. Chem. B* **108**, 6961–6968 (2004) doi:10.1021/jp036261n.

169. Wadell, C. & Langhammer, C. Drift-corrected nanoplasmonic hydrogen sensing by polarization. *Nanoscale* **7**, 10963–10969 (2015) doi:10.1039/C5NR01818H.

170. Wadell, C., Syrenova, S. & Langhammer, C. Plasmonic hydrogen sensing with nanostructured metal hydrides. *ACS Nano* **8**, 11925–11940 (2014) doi:10.1021/nn505804f.

171. Syrenova, S. *Nanoplasmonic Spectroscopy of Single Nanoparticles Tracking Size and Shape Effects in Pd Hydride Formation*. (Institutionen för teknisk fysik, Kemisk fysik, Chalmers tekniska högskola, 2014).

172. Langhammer, C., Zhdanov, V. P., Zorić, I. & Kasemo, B. Size-dependent kinetics of hydriding and dehydriding of Pd nanoparticles. *Phys. Rev. Lett.* **104**, (2010) doi:10.1103/PhysRevLett.104.135502.

173. Shegai, T. & Langhammer, C. Hydride formation in single palladium and magnesium nanoparticles studied by nanoplasmonic dark-field scattering spectroscopy. *Adv. Mater.* **23**, 4409–4414 (2011) doi:10.1002/adma.201101976.

174. Duan, X., Kamin, S., Sterl, F., Giessen, H. & Liu, N. Hydrogen-Regulated Chiral Nanoplasmonics. *Nano Lett.* **16**, 1462–1466 (2016) doi:10.1021/acs.nanolett.5b05105.

175. Sterl, F. *et al.* Nanoscale Hydrogenography on Single Magnesium Nanoparticles. *Nano Lett.* acs.nanolett.8b01277 (2018) doi:10.1021/acs.nanolett.8b01277.

176. Rice, K. P., Walker, E. J., Stoykovich, M. P. & Saunders, A. E. Solvent-dependent surface plasmon response and oxidation of copper nanocrystals. *J. Phys. Chem. C* **115**, 1793–1799 (2011) doi:10.1021/jp110483z.

177. Susman, M. D., Feldman, Y., Bendikov, T. A., Vaskevich, A. & Rubinstein, I. Real-time plasmon spectroscopy study of the solid-state oxidation and Kirkendall void formation in copper nanoparticles. *Nanoscale* **9**, 12573–12589 (2017) doi:10.1039/C7NR04256F.

178. Mayer, K. M. & Hafner, J. H. Localized surface plasmon resonance sensors. *Chem. Rev.* **111**, 3828–3857 (2011) doi:Doi 10.1021/Cr100313v.

179. Langhammer, C., Larsson, E. M., Kasemo, B. & Zorić, I. Indirect Nanoplasmonic Sensing: Ultrasensitive Experimental Platform for Nanomaterials Science and Optical Nanocalorimetry. *Nano Lett.* **10**, 3529–3538 (2010) doi:10.1021/nl101727b.

180. Larsson, E. M. *et al.* Real Time Indirect Nanoplasmonic in Situ Spectroscopy of Catalyst Nanoparticle Sintering. *ACS Catal.* **2**, 238–245 (2012) doi:10.1021/cs200583u.

181. Ringe, E., Sharma, B., Henry, A.-I., Marks, L. D. & Van Duyne, R. P. Single nanoparticle plasmonics. *Phys. Chem. Chem. Phys. Phys. Chem. Chem. Phys. Phys. Chem. Chem. Phys* **1515121**, 4075–4460 (2013) doi:10.1039/c3cp44574g.

182. Ohtsu, M. *Progress in Nanophotonics 1*. (Springer Berlin Heidelberg, 2011). doi:10.1007/978-3-642-17481-0.

183. Tanaka, Y. *et al.* Direct imaging of nanogap-mode plasmon-resonant fields. *Opt. Express* **19**, 7726–7733 (2011) doi:10.1364/OE.19.007726.

184. Imura, K., Nagahara, T. & Okamoto, H. Near-field optical imaging of plasmon modes in gold nanorods. *J. Chem. Phys.* **122**, 154701 (2005) doi:10.1063/1.1873692.

185. Cinchetti, M. *et al.* Photoemission Electron Microscopy as a Tool for the Investigation of Optical Near Fields. *Phys. Rev. Lett.* **95**, 047601 (2005) doi:10.1103/PhysRevLett.95.047601.

186. Sun, Q. *et al.* Direct imaging of the near field and dynamics of surface plasmon resonance on gold nanostructures using photoemission electron microscopy. *Light Sci. Appl.* **2**, e118–e118 (2013) doi:10.1038/lsa.2013.74.

187. Chaturvedi, P. *et al.* Imaging of Plasmonic Modes of Silver Nanoparticles Using High-Resolution Cathodoluminescence Spectroscopy. *ACS Nano* **3**, 2965–2974 (2009) doi:10.1021/nn900571z.

188. García de Abajo, F. J. & Kociak, M. Probing the Photonic Local Density of States with Electron Energy Loss Spectroscopy. *Phys. Rev. Lett.* **100**, 106804 (2008) doi:10.1103/PhysRevLett.100.106804.

189. Boyer, D., Tamarat, P., Maali, A., Lounis, B. & Orrit, M. Photothermal imaging of nanometer-sized metal particles among scatterers. *Science* **297**, 1160–3 (2002) doi:10.1126/science.1073765.

190. Pini, V. *et al.* Spatially multiplexed dark-field microspectrophotometry for nanoplasmonics. *Sci. Rep.* **6**, 22836 (2016) doi:10.1038/srep22836.

191. Zopf, D. *et al.* Hyperspectral imaging of plasmon resonances in metallic nanoparticles. *Biosens. Bioelectron.* **81**, 287–293 (2016) doi:10.1016/J.BIOS.2016.03.001.

192. Kane Yee. Numerical solution of initial boundary value problems involving maxwell's equations in isotropic media. *IEEE Trans. Antennas Propag.* **14**, 302–307 (1966) doi:10.1109/TAP.1966.1138693.

193. Inc., L. No Title.

194. FitzGerald, K. P., Nairn, J., Skennerton, G. & Atrens, A. Atmospheric corrosion of copper and the colour, structure and composition of natural patinas on copper. *Corros. Sci.* **48**, 2480–2509 (2006) doi:https://doi.org/10.1016/j.corsci.2005.09.011.

195. Hauffe, K. *Oxidation of Metals*. (Springer US, 1995). doi:10.1007/978-1-4684-8920-0.

196. Carter, R. E. Kinetic Model for Solid-State Reactions. *J. Chem. Phys.* **34**, 2010–2015 (1961) doi:10.1063/1.1731812.

197. Yin, Y. *et al.* Formation of hollow nanocrystals through the nanoscale Kirkendall effect. *Science* **304**, 711–4 (2004) doi:10.1126/science.1096566.

198. Chen, Y. Nanofabrication by electron beam lithography and its applications: A review. *Microelectron. Eng.* **135**, 57–72 (2015) doi:10.1016/J.MEE.2015.02.042.

199. Tseng, A. A. (Ampere A. . *Nanofabrication : fundamentals and applications*. (World Scientific, 2008).

200. Stepanova, M. & Dew, S. *Nanofabrication. Techniques and Principles* vol. 9783709104 (Springer Vienna, 2012). doi:10.1007/978-3-7091-0424-8.

201. Williams, K. R., Gupta, K. & Wasilik, M. Etch rates for micromachining processing-part II. *J. Microelectromechanical Syst.* **12**, 761–778 (2003) doi:10.1109/JMEMS.2003.820936.

202. Laermer, F. & Schilp, A. Method of anisotropically etching silicon. (1996).

203. Deal, B. E. & Grove, A. S. General Relationship for the Thermal Oxidation of Silicon. *J. Appl. Phys.* **36**, 3770–3778 (1965) doi:10.1063/1.1713945.

204. BYU Electrical and computer engineering. Oxide Thickness Calculator | BYU Cleanroom. http://cleanroom.byu.edu/OxideThickCalc.

205. Ohring, M. *Materials Science of Thin Films*. *Materials Science* vol. 29 (Elsevier, 2002). doi:10.1016/B978-0-12-524975-1.50018-5.

206. Yang, S.-M., Jang, S. G., Choi, D.-G., Kim, S. & Yu, H. K. Nanomachining by Colloidal Lithography. *Small* **2**, 458–475 (2006) doi:10.1002/smll.200500390.

207. Fredriksson, H. *et al.* Hole-mask colloidal lithography. *Adv. Mater.* **19**, 4297–4302 (2007) doi:10.1002/adma.200700680.

208. Hanarp, P., Sutherland, D. S., Gold, J. & Kasemo, B. Control of nanoparticle film structure for colloidal lithography. *Colloids Surfaces A Physicochem. Eng. Asp.* **214**, 23–36 (2003) doi:10.1016/S0927-7757(02)00367-9.

209. Syrenova, S., Wadell, C. & Langhammer, C. Shrinking-hole colloidal lithography: Self-aligned nanofabrication of complex plasmonic nanoantennas. *Nano Lett.* **14**, 2655–2663 (2014) doi:10.1021/nl500514y.

210. Mao, P. & Han, J. Fabrication and characterization of 20 nm planar nanofluidic channels by glass–glass and glass–silicon bonding. *Lab Chip* **5**, 837 (2005) doi:10.1039/b502809d.

211. Goldstein, J. I. *et al. Scanning Electron Microscopy and X-ray Microanalysis*. (Springer US, 2003). doi:10.1007/978-1-4615-0215-9.

212. Williams, D. B. & Carter, C. B. *Transmission electron microscopy: A textbook for materials science*. (Springer US, 2009). doi:10.1007/978-0-387-76501-3.

213. El Mel, A.-A. *et al.* Electron Beam Nanosculpting of Kirkendall Oxide Nanochannels. *ACS Nano* **8**, 1854–1861 (2014) doi:10.1021/nn406328f.

214. Amati, M. *et al.* Photoelectron microscopy at Elettra: Recent advances and perspectives. *J. Electron Spectros. Relat. Phenomena* **224**, 59–67 (2018) doi:https://doi.org/10.1016/j.elspec.2017.06.006.

215. Kirchner, S. R. *et al.* Snapshot Hyperspectral Imaging (SHI) for Revealing Irreversible and Heterogeneous Plasmonic Processes. *J. Phys. Chem. C* **122**, 6865–6875 (2018) doi:10.1021/acs.jpcc.8b01398.

216. Wang, H., Zhang, T. & Zhou, X. Dark-field spectroscopy: development, applications and perspectives in single nanoparticle catalysis. *J. Phys. Condens. Matter* **31**, 473001 (2019) doi:10.1088/1361-648X/ab330a.

217. Armstrong, R. E., van Liempt, J. C. & Zijlstra, P. Effect of Film Thickness on the Far- and Near-Field Optical Response of Nanoparticle-on-Film Systems. *J. Phys. Chem. C* **123**, 25801–25808 (2019) doi:10.1021/acs.jpcc.9b06592.

218. Gross, J. H. *Mass Spectrometry*. (Springer Berlin Heidelberg, 2011). doi:10.1007/978-3-642-10711-5.

219. Xu, Y. Nanofluidics: A New Arena for Materials Science. *Adv. Mater.* **30**, 1702419 (2018) doi:10.1002/adma.201702419.

220. Mawatari, K., Kazoe, Y., Shimizu, H., Pihosh, Y. & Kitamori, T. Extended-Nanofluidics: Fundamental Technologies, Unique Liquid Properties, and Application in Chemical and Bio Analysis Methods and Devices. *Anal. Chem.* **86**, 4068–4077 (2014) doi:10.1021/ac4026303.

221. Kim, S. J., Wang, Y.-C., Lee, J. H., Jang, H. & Han, J. Concentration Polarization and Nonlinear Electrokinetic Flow near a Nanofluidic Channel. *Phys. Rev. Lett.* **99**, 044501 (2007) doi:10.1103/PhysRevLett.99.044501.

222. Louër, A.-C. *et al.* Pressure-Assisted Selective Preconcentration in a Straight

Nanochannel. *Anal. Chem.* **85**, 7948–7956 (2013) doi:10.1021/ac4016159.

223. Gamble, T. *et al.* Rectification of Ion Current in Nanopores Depends on the Type of Monovalent Cations: Experiments and Modeling. *J. Phys. Chem. C* **118**, 9809–9819 (2014) doi:10.1021/jp501492g.

224. Zhang, M. *et al.* Light and pH Cooperative Nanofluidic Diode Using a Spiropyran-Functionalized Single Nanochannel. *Adv. Mater.* **24**, 2424–2428 (2012) doi:10.1002/adma.201104536.

225. Xu, Y. & Xu, B. An Integrated Glass Nanofluidic Device Enabling In-situ Electrokinetic Probing of Water Confined in a Single Nanochannel under Pressure-Driven Flow Conditions. *Small* **11**, 6165–6171 (2015) doi:10.1002/smll.201502125.

226. Hibara, A. *et al.* Nanochannels on a Fused-Silica Microchip and Liquid Properties Investigation by Time-Resolved Fluorescence Measurements. *Anal. Chem.* **74**, 6170–6176 (2002) doi:10.1021/ac025808b.

227. Tas, N. R., Haneveld, J., Jansen, H. V., Elwenspoek, M. & van den Berg, A. Capillary filling speed of water in nanochannels. *Appl. Phys. Lett.* **85**, 3274–3276 (2004) doi:10.1063/1.1804602.

228. Bocquet, L. & Tabeling, P. Physics and technological aspects of nanofluidics. *Lab Chip* **14**, 3143–3158 (2014) doi:10.1039/C4LC00325J.

229. Haywood, D. G., Saha-Shah, A., Baker, L. A. & Jacobson, S. C. Fundamental Studies of Nanofluidics: Nanopores, Nanochannels, and Nanopipets. *Anal. Chem.* **87**, 172–187 (2015) doi:10.1021/ac504180h.

230. Sparreboom, W., van den Berg, A. & Eijkel, J. C. T. Principles and applications of nanofluidic transport. *Nat. Nanotechnol.* **4**, 713–720 (2009) doi:10.1038/nnano.2009.332.

231. Viefhues, M., Regtmeier, J. & Anselmetti, D. Fast and continuous-flow separation of DNA-complexes and topological DNA variants in microfluidic chip format. *Analyst* **138**, 186–196 (2013) doi:10.1039/C2AN36056J.

232. Regtmeier, J., Käsewieter, J., Everwand, M. & Anselmetti, D. Continuous-flow separation of nanoparticles by electrostatic sieving at a micro-nanofluidic interface. *J. Sep. Sci.* **34**, 1180–1183 (2011) doi:10.1002/jssc.201100007.

233. Tegenfeldt, J. O. *et al.* The dynamics of genomic-length DNA molecules in 100-nm channels. *Proc. Natl. Acad. Sci.* **101**, 10979–10983 (2004) doi:10.1073/pnas.0403849101.

234. Müller, V. & Westerlund, F. Optical DNA mapping in nanofluidic devices: principles and applications. *Lab Chip* **17**, 579–590 (2017) doi:10.1039/C6LC01439A.

235. Prakash, S. & Yeom, J. *Nanofluidics and Microfluidics*. (Elsevier, 2014). doi:10.1016/C2010-0-66159-1.

236. Xu, Y., Matsumoto, N., Wu, Q., Shimatani, Y. & Kawata, H. Site-specific nanopatterning of functional metallic and molecular arbitrary features in nanofluidic channels. *Lab Chip* **15**, 1989–1993 (2015) doi:10.1039/C5LC00190K.

237. Haber, J. Manual on catalyst characterization (Recommendations 1991). *Pure Appl. Chem.* **63**, 1227–1246 (1991) doi:https://doi.org/10.1351/pac199163091227.

238. Karniadakis, G., Beskok, A. & Aluru, N. Basic Concepts and Technologies. in *Microflows and Nanoflows* (eds. Karniadakis, G. et al.) 1–48 (Springer-Verlag, 2005). doi:10.1007/0-387-28676-4_1.

239. Beskok, A. & Karniadakis, G. E. Report: A model for flows in channels, pipes, and ducts

at micro and nano scales. *Microscale Thermophys. Eng.* **3**, 43–77 (1999) doi:10.1080/108939599199864.

240. Ida, N. *Sensors, Actuators, and their Interfaces: A Multidisciplinary Introduction*. *Sensors, Actuators, and their interfaces - a multidisciplinary introduction* (Institution of Engineering and Technology, 2013). doi:10.1049/SBCS502E.

241. Siemens, C. W. The Bakerian Lecture: On the Increase of Electrical Resistance in Conductors with Rise of Temperature, and Its Application to the Measure of Ordinary and Furnace Temperatures; Also on a Simple Method of Measuring Electrical Resistances. *Proc. R. Soc. London* **19**, 443–445 (1870) doi:10.1098/rspl.1870.0066.

242. Van Dusen, M. V. Platinum-resistance thermometry at low temperatures. *J. Am. Chem. Soc.* **47**, 326–332 (1925) doi:10.1021/ja01679a007.

243. Pu, T., Tian, H., Ford, M. E., Rangarajan, S. & Wachs, I. E. Overview of Selective Oxidation of Ethylene to Ethylene Oxide by Ag Catalysts. *ACS Catal.* **9**, 10727–10750 (2019) doi:10.1021/acscatal.9b03443.

244. Zhang, Z. *et al.* The most active Cu facet for low-temperature water gas shift reaction. *Nat. Commun.* **8**, 488 (2017) doi:10.1038/s41467-017-00620-6.

245. Greiner, M. T., Jones, T. E., Klyushin, A., Knop-Gericke, A. & Schlögl, R. Ethylene Epoxidation at the Phase Transition of Copper Oxides. *J. Am. Chem. Soc.* **139**, 11825–11832 (2017) doi:10.1021/jacs.7b05004.

246. Cao, J. *et al.* In situ observation of oscillatory redox dynamics of copper. *Nat. Commun.* **11**, 3554 (2020) doi:10.1038/s41467-020-17346-7.

247. Zhang, H. *et al.* Direct Assembly of Large Area Nanoparticle Arrays. *ACS Nano* **12**, 7529–7537 (2018) doi:10.1021/acsnano.8b02932.

248. Gargiulo, J., Cerrota, S., Cortés, E., Violi, I. L. & Stefani, F. D. Connecting Metallic Nanoparticles by Optical Printing. *Nano Lett.* **16**, 1224–1229 (2016) doi:10.1021/acs.nanolett.5b04542.